

**From Low to High Fidelity Geophysics:  
3-D Multi-Component  
Shallow Seismic Surveying  
in the Lions' Harbour of Miletus (Turkey)**

Dissertation  
zur Erlangung des Doktorgrades  
der Mathematisch-Naturwissenschaftlichen Fakultät  
der Christian-Albrechts-Universität zu Kiel

vorgelegt von  
**Susanne Wölz**

Kiel 2003

Referent:	Prof. Dr. Wolfgang Rabbel
Korreferent:	Prof. Dr. Rolf Meissner
Tag der mündlichen Prüfung:	12. Dezember 2003
Zum Druck genehmigt:	17. Dezember 2003

Der Dekan

”Stets findet Überraschung statt,  
da wo man’s nicht erwartet hat.”

WILHELM BUSCH

## Abstract

Geophysical work in the alluvial sedimentary environment of the archaeological site of Miletus' Lions' Harbour (Turkey) raised the question whether suspicious anomalies observed in magnetic data could be related to historic building structures. 2-D shear wave seismic refraction surveys did not provide sufficient lateral resolution to answer this question precisely. Thus, two 3-D multi-component refraction surveys were carried out covering the anomalies. The experiment also aimed to evaluate the potential of this new high resolution seismic technique for shallow acquisition developed in the thesis.

The 2-C and 3-C geophone grids, resp., with 1 *m* spacing provided sufficient lateral sampling to record the coherent wavefield. Lines were shot successively, rather than acquiring data in one large 2-D spread. Interpretation of S-wave data in 3-D is improved if orthogonal horizontal point sources are applied. The vector source was realized with a man-driven sledgehammer. In part problems occurred with geophone planting and coupling due to significant mud cracks and tamarisk cover.

If acquired in 3-D seismic vector data have the potential to resolve lateral velocity heterogeneity with high resolution. The complexity of the direct, refracted and reflected wavefield is impressive in unprocessed data. Wavefront bending due to refractor geometry or velocity heterogeneity is significant. Structural detail even below the wavelength limit is vast. Surface waves are able to map sharp lateral material contrast with lower than wavelength accuracy. Even the influence of mud cracks could be imaged in the coda of ground coupled airwaves and radiation patterns.

Due to acquisition geometry and wavefield characteristics different phases of the wavefield intermix. Three different approaches to wavefield separation were defined and investigated, comprising a simple wavefield component rotation to geometric ray direction, calculation of curl and divergence at the surface and rotation into the ray coordinate system ("slowness projection"). The latter turned out providing the best results for refracted arrivals.

The refractor imaging technique applied in this thesis uses data separated by slowness projection as input and is capable to map coherent basement structures on the meter-scale. The resulting model describes the depth function of the refracting horizon relative to a constant reference depth level which has to be determined, for instance, by intercept-time analysis or, even preciser, by drilling. The minimum rms-error  $\epsilon$  between cored bedrock depth and refractor model is  $\epsilon = 0.44m$  (4.2 %) at an average refractor depth of  $z_0 = 10.5m$ . The velocity model obtained from tomographic inversion using the refractor topography model as input exhibits surface velocity anomalies and a prominent high velocity zone in the refractor.

Spectral analysis of the surface wavefield, gave some indication for a seismic anomaly in about 3 – 6 *m* depth, which is not "seen" by the refracted wave. Coinciding magnetic anomalies and Rayleigh velocity contrasts, possibly representing antique moles, correlate well with the basin topography. The shape of the Milesian Lions' Harbour basin at this location is shallow enough and provides appropriate ground to found moles on solid rock.

## Zusammenfassung

Die bisherigen geophysikalischen Arbeiten im verlandeten Löwenhafen der archäologischen Stätte Milet (Türkei) warfen die Frage auf, ob beobachtete magnetische Anomalien in Verbindung mit historischen Gebäudestrukturen stehen. Diese Frage konnte mit 2D-Scherwellen-Refraktionsseismik aufgrund ungenügender lateraler Auflösung nicht widerspruchsfrei geklärt werden. Infolgedessen wurden zwei ausgewählte Lokationen mit 3D-Mehrkomponenten-Refraktionsseismik vermessen. Dieses Experiment war außerdem darauf ausgerichtet, das Potential dieser hier entwickelten, neuen und einfachen, hochauflösenden seismischen Methode für Flachgrunduntersuchungen einzuschätzen.

Zwei- oder Dreikomponentenauslagen im 1 m Abstand lieferten ausreichende laterale Abtastung und eigneten sich zur Erfassung des kohärenten Wellenfeldes. Profile wurden nacheinander und nicht mit einer Gesamtauslage aufgezeichnet. Die Interpretation von Scherwellen in 3D wird verbessert, wenn horizontal polarisierte Punktquellen verwendet werden. Die Vektorquellen wurden durch Schürfschläge verwirklicht. Verursacht durch tiefe Trockenrisse und Tamariskenbewuchs traten teilweise Probleme beim Stecken und bei der Ankoppelung der Geophone auf.

Vektordaten haben das Potential, laterale Geschwindigkeitsunterschiede mit einer hohen Genauigkeit aufzulösen, wenn in 3D aufgezeichnet wird. Schon in den unbearbeiteten Daten ist die Komplexität des direkten, refraktierten und reflektierten Wellenfeldes beeindruckend. Wellenfronten starker Krümmung, verursacht durch Refraktortopographie oder Geschwindigkeitsunterschiede, sind signifikant. Die Menge struktureller Details auch unterhalb der Auflösungsgrenze ist beachtlich. Oberflächenwellen können scharfe laterale Materialkontraste abbilden, die kleiner als eine Wellenlänge sind. Sogar in der Coda der eingekoppelten Luftwelle und im Abstrahlmuster bildet sich der Einfluß der Trockenrisse ab.

Aufgrund der Akquisitionsgeometrie und des Wellenfeldcharakters mischen sich verschiedene Phasen des Wellenfeldes. Deswegen wurden drei verschiedene Methoden der Wellenfeldtrennung untersucht: eine einfache Drehung der Wellenfeldkomponenten in die geometrische Strahlrichtung, die Berechnung von Rotation und Divergenz des Wellenfeldes an der Oberfläche und die Drehung der Wellenfeldkomponenten ins Strahlkoordinatensystem ("slowness projection"), wobei letztere Methode das beste Ergebnis für refraktierte Wellen lieferte.

Das in dieser Arbeit entwickelte Abbildungsverfahren ist geeignet, kohärente Refraktorstrukturen im  $m$ -Bereich wiederzugeben. Das resultierende Modell beschreibt die Tiefenfunktion des refraktierenden Horizonts bis auf eine konstante Referenztiefe, die aus der Interceptzeitmethode oder noch genauer aus Bohrinformationen bestimmt werden muss. Der minimale RMS-Fehler  $\epsilon$  zwischen erbohrter und errechneter Refraktortiefe beträgt  $\epsilon = 0,44 \text{ m}$  (4,2 %), bei einer durchschnittlichen Refraktortiefe von  $z_0 = 10,5 \text{ m}$ . Ein durch tomographische Inversion erhaltenes Geschwindigkeitsmodell zeigt Oberflächenanomalien und eine markante Hochgeschwindigkeitszone im Refraktor.

Die Spektralanalyse der Oberflächenwellen ergab einige Hinweise auf eine seismische Anomalie in ca. 3–6 m Tiefe, die von der refraktierten Welle nicht „gesehen“ wird. Das gemeinsame Auftreten von magnetischen Anomalien und von Kontrasten in der Rayleighgeschwindigkeit, das möglicherweise antike Molen repräsentiert, korreliert gut mit der Beckentopographie. Die Form des Milesischen Löwenhafens an dieser Stelle ist flach genug und bietet geeigneten Untergrund, Molen direkt auf Kalkstein zu gründen.

# Contents

<b>1</b>	<b>Introduction</b>	<b>3</b>
<b>2</b>	<b>Miletus</b>	<b>9</b>
2.1	Geological and Morphological Settings . . . . .	9
2.2	History and Archaeology . . . . .	13
2.3	Geophysical Investigations in Miletus . . . . .	15
2.3.1	The greater city area . . . . .	16
2.3.2	Lions' Harbour . . . . .	18
<b>3</b>	<b>Seismic Data Acquisition and Simulation</b>	<b>22</b>
3.1	3-D 4-C . . . . .	22
3.2	3-D 9-C . . . . .	23
3.3	Synthetic Data . . . . .	25
<b>4</b>	<b>Processing and Imaging Methodology</b>	<b>28</b>
4.1	Generic preprocessing and data display . . . . .	28
4.2	Wavefield separation . . . . .	30
4.2.1	Basic vector rotations . . . . .	31
4.2.2	Vector field operations <i>curl</i> and <i>divergence</i> . . . . .	34
4.2.3	Slowness projection (ray coordinate system) . . . . .	36

---

4.3	Wavefield Optimization . . . . .	37
4.4	Refractor Imaging . . . . .	40
<b>5</b>	<b>Application to Field Data</b>	<b>46</b>
5.1	Wavefield Phenomena . . . . .	46
5.1.1	Radiation Patterns . . . . .	48
5.1.2	Refracted waves . . . . .	51
5.1.3	Surface waves . . . . .	54
5.2	Separation of wavefield constituents . . . . .	57
5.2.1	Source characteristics . . . . .	57
5.2.2	3-D effect . . . . .	59
5.2.3	Discussion . . . . .	65
5.3	Refractor Imaging . . . . .	65
5.3.1	Topography of Lions' Harbour (east) . . . . .	65
5.3.2	Interpretation and Discussion . . . . .	72
<b>6</b>	<b>Discussion and Conclusions</b>	<b>76</b>
	<b>References</b>	<b>79</b>
<b>A</b>	<b>Technical Miscellanea</b>	<b>85</b>
<b>B</b>	<b>Additional Data Examples</b>	<b>89</b>
<b>C</b>	<b>Tomographical Inversion</b>	<b>102</b>

# Chapter 1

## Introduction

### **Geophysics and Archaeology**

The liaison between Geophysics and Archaeology began after the second world war, when in 1946 Richard Atkinson carried out a Wenner resistivity survey to investigate a henge site in Dorchester, England (Atkinson, 1952). In the more recent past the use of geophysical methods for archaeology gained popularity, with a preference on electrical resistivity, magnetics and ground probing radar. Seismic and other techniques such as infrared imagery, self potential or micro-gravity are less commonly used (Wynn, 1986a; Wynn, 1986b). The generally low data acquisition rate compared to other geophysical methods and the relative lack of resolution might be the most obvious explanation for this. However seismic as a method in its own right, always becomes indispensable if the structure of lithological contacts in the subsurface is the target of the investigation and when, e.g. electrical pseudo sections do not provide sufficient resolution or are not acquirable due to malformed soil conditions. Therefore, over the last two decades the number of seismic investigations at archaeological sites increased. Seismic refraction surveys are now usually preferred to investigate shallow sedimentary targets (Stümpel *et al.*, 1988; Weinstein-Evron *et al.*, 1991; Tsokas *et al.*, 1995; Karastathis & Pappas, 1997; Benjumea *et al.*, 2000; Cardarelli & Nardis, 2001), whereas the seismic reflection acquisition technique is aimed at deeper horizons (20-30m) because reflections are mostly covered by direct arrivals and ground roll in the shallow (Stright, 1986; Dobecki & Schoch, 1992) or deployed in marine environments (Stümpel & Meissner, 1982).

### **Standard 2-D refraction seismic acquisition**

Refraction seismic is a well established method to determine the shallow structure of lithological contacts for engineering as well as oil and mineral exploration. While the primary goal of the former is to directly determine the structure of subsurface layers (Palmer, 1981; Palmer, 1986; Palmer, 2001b; Palmer, 2001c; Palmer, 2001a; Clayton & A., 1981; Hill, 1987; Piip, 2001; Belfer *et al.*, 1998), the latter mostly applies the gained velocity information for static corrections or to get an overview of an unknown area.

The use of compressional waves for exploration is very common in today's industrial and,



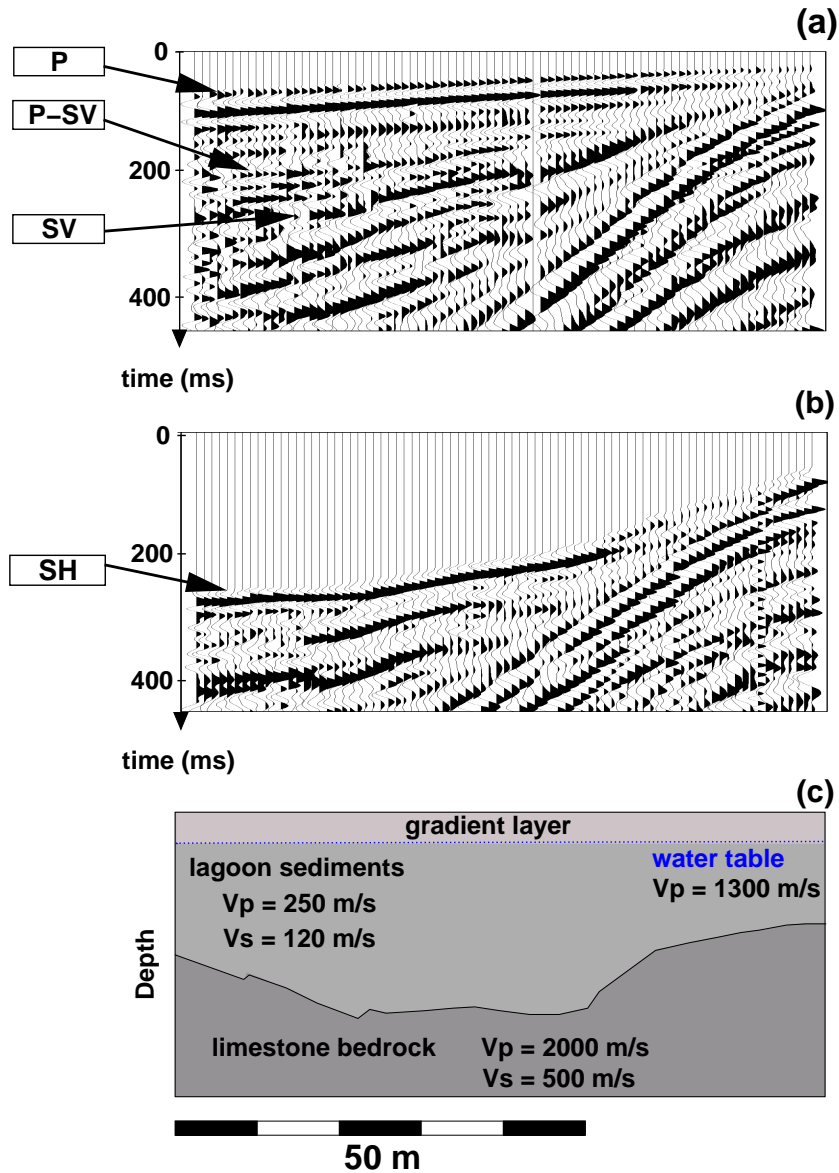


**Figure 1.1:** The comparison illustrates the advantages of using shear waves for refraction surveys. Panel (a): seismogram of a vertical component. The refracted P wave propagates through the water table. Panel (b): seismogram of a horizontal cross-line component. The refracted SH event prominently outlines the refractor topography. Panel (c): Subsurface interpretation.

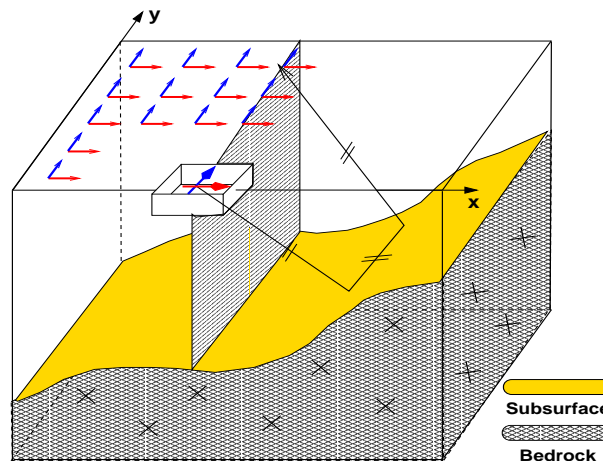


**Figure 1.2:** *Strong refractor topography causes refracted seismic energy to travel on ray paths not falling into the vertical plane below the spread. The sketch also illustrates the acquisition geometry concept.*

if seismic is used at all, also in archaeological applications. This is in part motivated by the convenient way to excite and record the compressional wavefields. Also the smaller logistical and processing efforts evolved compared to shear wave surveys are sometimes preferable.

Nevertheless, shear wave exploration surveys became more and more popular in the last decade, as is demonstrated by the increasing number of journal publications and conference presentations since the 1990s (e.g. Leading Edge Special Sections in April 1998, October 1998 and September 2001).

Shear wave exploration, although logistically and financially more expensive, provide a number of advantages over P wave exploration. If P- and S-wave signals are generated in the same frequency interval, shear waves will show about two-to ten-times higher resolution than P-waves because of their lower propagation velocity. Even  $V_p/V_s$ -ratios of higher than 10 are not unusual in shallow environments. In addition and in contrast to compressional waves S-wave velocity is nearly independent of pore fluids so it is linked more closely to lithology (Stümpel *et al.*, 1984). In particular, S-wave propagation is not influenced by the groundwater table which may cover shallow refracting horizons.

It is common practice to use one-dimensional geophone spreads to record the particle motion also motivated by the limited logistical efforts evolved. Acquisition and processing procedures for such 2-D refraction seismic surveys are simple and well understood. In shallow shear wave surveys S-waves are typically excited by realizing a horizontally oriented vector source with a horizontally led sledgehammer blow. The seismic spread will be oriented perpendicular to the strike of geological structure and shear wave sensors parallel to it. Thus preferably, SH- and Love-waves are recorded along the profile, and P-energy is minimized.

In order to illustrate the advantages of using shear waves for refraction surveys we take

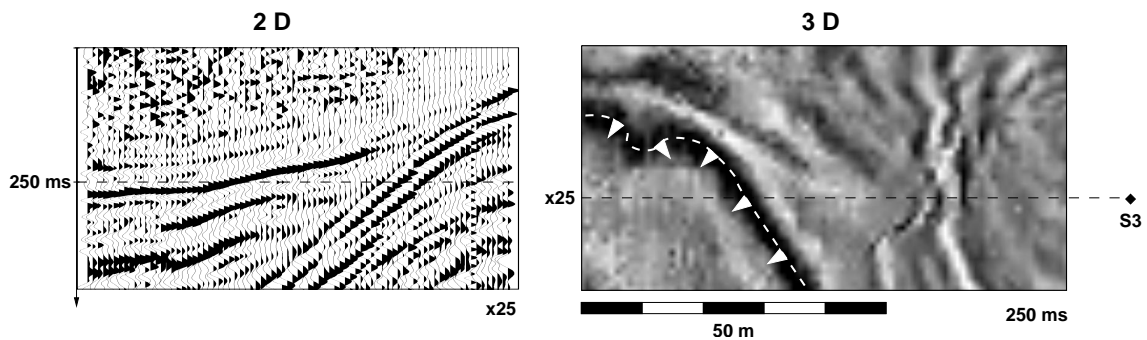


**Figure 1.3:** 2-D (left) versus 3-D (right) refraction seismic acquisition: A time slice from a 3-D refraction seismic SH wave survey illustrates that the refracted event (direction of propagation marked by arrows) due to refractor topography exhibits significant offline contribution. The seismogram on the left results from acquisition along the dashed line on the right.

a look at the following example. Figure 1.1 shows a typical 2-D refraction survey seismogram (panel a) excited by a vertical sledge hammer blow and recorded with vertical receivers. We clearly see the refracted P wave propagating through the water table (see panel (c) for subsurface interpretation). The structure of the targeted limestone basin can only be retrieved from a weak and noisy P to SV converted event (panel a). For comparison panel (b) shows a seismogram corresponding to a recording with a horizontally led crossline hammer blow and horizontally arranged receivers. The refracted event consists of an SH polarized wavefield and prominently outlines the refractor topography.

### 3-D multicomponent refraction seismic acquisition: advantages and difficulties

A typical 2-D refraction survey assumes a one-dimensional vertical velocity structure for the subsurface ignoring 2-D refractor topography (see figure 1.2). However, seismic wave propagation is a 3-D phenomenon especially when geological interfaces show complicated topography. In certain environments, such as basins, regions with tectonic imprint or salt uplift, prominent refractor topography causes refracted seismic energy to travel on ray paths not falling into the vertical plane spanned by the spread and the surface normal (cf. fig. 1.2). Figure 1.3 shows a time slice from a 3-D refraction seismic SH wave survey in the right panel, illustrating this effect. It becomes obvious that the refracted event (direction of propagation marked by arrows) due to refractor topography would exhibit significant offline contribution and thus the interpretation can be ambiguous, wrong or simply impossible, if recording is done with a traditional 2-D spread (i.e. along the dashed line in the right panel of the figure, resulting in the seismogram on the left). It would be difficult to detect the ray direction of the refracted wave and impossible to reconstruct the real 3-D structure of the subsurface. In order to circumvent such interpretation pitfalls, the wavefield has to be recorded with a 2-D spread, i.e. using 3-D

refraction seismic techniques (Bennett, 1999; Gaiser, 1999; Blott *et al.*, 1999).

Other difficulties arise because the subsurface is an elastic medium. Due to conversion a mixture of different wavetypes is recorded by the spread, which can best be accounted for with a multi-component survey. The use of multicomponent surveys in industrial applications is already established as state-of-the-art (Ebrom *et al.*, 1998; Margrave *et al.*, 1998; Winterstein *et al.*, 1998; Hardage *et al.*, 2003). However, in shallow acquisition this technique is not common, moreover multicomponent refraction surveys have not been reported in the literature.

Interpretation is challenging, because it comprises converted and primary wavefields as well as surface waves of different polarizations, aside from the enormous amount of data involved in acquiring and processing the seismic response from complex refractor topography with a 3-D multicomponent refraction survey.

Depending on the spatial arrangement of source- and receiver-points, layer geometry and source type, geophones will record a mixture of P-, S-, Rayleigh- and Love-waves. The resulting interference pattern may have a confusing appearance especially at small offsets as they are common in shallow prospecting. Thus wavefield separation has to be carried out as a preparatory step prior to interpretation. Also source radiation and sensor reception pattern have to be accounted for.

A number of wavefield separation methods were developed during the last years and several reviews are given in the literature (e.g. Richwalski *et al.*, 2000 or Robertsson & Curtis, 2002). Most of them were developed to separate up and down going wavefields in VSPs (Kommedal & Tjostheim, 1989) or at ocean bottoms and for separating  $S1$  and  $S2$  waves in anisotropic media (Dellinger *et al.*, 2002; Maultzsch *et al.*, 2003; Liu *et al.*, 2003).

### **Outline of this thesis**

This thesis is intended to demonstrate the potential of a newly developed, high resolution, 3-D, multicomponent shear wave refraction seismic technique for shallow acquisition.

The data presented in this thesis were acquired at the archaeological site of Miletus (Western Turkey) as part of a project to derive geological boundary conditions for the antique cultivation and insights into other human activities there, like trade and transport. However, the focus of this thesis, is not exclusively on the archaeological outcome of the geophysical measurements but mainly on the experience gained with multicomponent acquisition, processing, and interpretation of 3-D wavefields in the shallow subsurface. Another main goal is to show that multi-component 3-D refraction seismic acquisition is a feasible technique for shallow seismic exploration.

Following this introduction an overview of the area of interest, including geological and archaeological information as well as previous geophysical surveys will be given in **chapter two**.

Two 3-D multicomponent refraction seismic surveys were carried out in the alluvial sedimentary environment of the Lions' Harbour of Miletus. Both surveys are covering areas exhibiting suspicious magnetic anomalies observed in earlier geophysical work, in the

western and eastern part of the harbour, respectively, which are of general archaeological interest.

Also a synthetic seismic survey was simulated by 3-D viscoelastic Finite Difference modeling (Bohlen, 2002) and is used to verify newly developed processing techniques. An overview of the acquisition geometry and physical parameters of field and virtual surveys is given in **chapter three**.

After documenting generic preprocessing the methodology and theoretical performance of three different wavefield separation approaches is presented in **chapter four**. The investigation is supported by synthetic data examples.

For 3-D surveys refractor topography can not be deduced with standard 2-D refraction interpretation techniques. The layout of a 3-D seismic refraction survey is not designed in strict analogy to a 2-D survey, e.g. in a regular Cartesian grid there is not always a pair of reverse shots for each possible line. Thus, the determination of refractor topography and velocity can not be obtained by simply extending traditional refraction interpretation techniques into 3-D. Seismic inversion by tomography is a possible remedy for this problem but suffers from heterogenous resolution if only a limited number of shot points is used.

A new simple approach to 3-D refractor topography inversion is introduced in this thesis. The methodology of this technique is also covered in **chapter four**.

**Chapter five** starts with a general discussion of kinematic as well as dynamic phenomena observed in both of the field data examples. Subsequently the different wave field separation methods are applied to the data.

In a first example the focus is put on separating direct and surface waves and the effects of source and receiver radiation and reception patterns, respectively. The second example is more complex and lends itself to demonstrate the performance of separating refracted wavefields in 3-D. The advantages and disadvantages of the methods described here will be discussed.

In the last section of this chapter the proposed 3-D refractor topography inversion method is applied to field data. The plain topographic results presented here are supported by tomographic refractor inversion which is also discussed.

# Chapter 2

## Miletus

Since Miletus is an investigation site of great archaeological interest history motivates all activities in the area. Thus, in the following chapter we will outline the greater and younger past of Miletus in chronological order (geological, historic, archaeological, and geophysical). We will start with the geological and morphological situation in the area because it has influenced rise and fall of ancient Miletus. Subsequently the historic past, archaeological and other scientific work will be described. The major part of this chapter, however, will document geophysical work and results in Miletus (geoelectrical, geomagnetical, radar, and seismic) with a focus on seismic investigations.

### 2.1 Geological and Morphological Settings

Associated with the collision between the African and the Eurasian plates and the resulting extension and westward migration of the Anatolian microplate, western Turkey is characterized by numerous east-west trending grabens, since the late Tertiary. The Mediterranean Sea transgressed into these grabens due to the postglacial sea level rise and formed the Latmian Gulf. Marine embayments partly extending far inland evolved such as Miletus, Priene, Myous, Magnesia, Tralleis (see figure 2.1).

When sea level reached close to its present position about 5,500 years ago the opposite process started. Fluvial sedimentation has led to the gradual infill of the embayments. Deltas, floodplains and lakes were created which now serve as geo-archives, storing most of the clastic sediments produced by erosion and denudation in the hinterland.

The Latmian Gulf silted up by the progradation of the Büyük Menderes (Meander, ancient name: Maiandros) delta (Fig. 2.4). Ancient seaports such as Miletus, Myous and Priene became landlocked and harbours unserviceable. This led to the decline and final desertion of the settlements. Thus their history was closely connected with the landscape evolution of the region. To date the scenarios for the historic delta growth of the Büyük Menderes have been mostly based on literary evidence and leave room for different interpretations (Fig. 2.4).

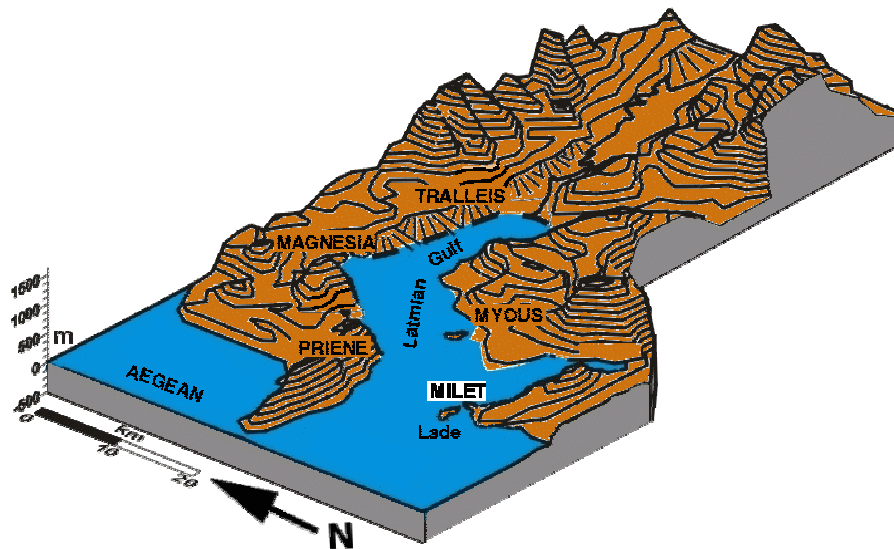


**Figure 2.1:** *The Latmian Gulf incised deep into the landscape more than two millenia ago. Miletus is located on its southern edge. This maximum extend was probably already reached 4000 BP (after Bay, 1999).*

Miletus is situated in western Turkey near the Aegean coast about 140 km south of Izmir and 90 km north of Bodrum (see figure 2.2, embedded map in the upper left hand corner). Morphologically noticeable is the some 500 km<sup>2</sup> expanded Büyük Menderes alluvial plain, the former Latmian Gulf, which has silted up during the last 2000 years. A remaining witness of the former bay is the Bafa Gölü (Bafa: Turkish for lake) which still holds brackish water. The plane is surrounded by a mountain landscape, such as Samsun Dağları, a crystalline region with metamorphic rocks up to 1400 m height and the Menderes massif to the East, also crystalline. In the South the plane is limited by more flat formations of Neogene limestone. Miletus itself was situated on a former peninsula in this Latmian Gulf (Kleiner, 1968) and its now stranded 10 km inland. Geological mapping in the surroundings of the city was done by Schröder & Yalcin, 1992. Sediments of a non-marine basin of the younger Tertiary were found. Lade island, west of Miletus and Kalabaktepe, south-west of the city, as well as the peninsula itself consists of freshwater limestone of different formations.

The Lions' Harbour in the north-western part of the city is a former bay of 150 m \* 300 m extent. The harbour is named after two huge lion statues which are still found on the former harbour area (see fig. 2.8, marked by "L") and is considered to be one of the key areas near the city center. It cuts deeply into the peninsula, separating two Neogene limestone hills, the Homeytepe and the Kaletepe, in the NE and SW, respectively. These hills are part of the Nergiztepe formation reaching up to 110 m thickness, so the previous harbour basin is embedded in limestone (Bay, 1996). The axis of the Lions' bay strikes nearly N to S. In the north a recent artificial dam is located to prevent the bay from flooding by the Menderes river. Morphologically, the boundary between limestone and

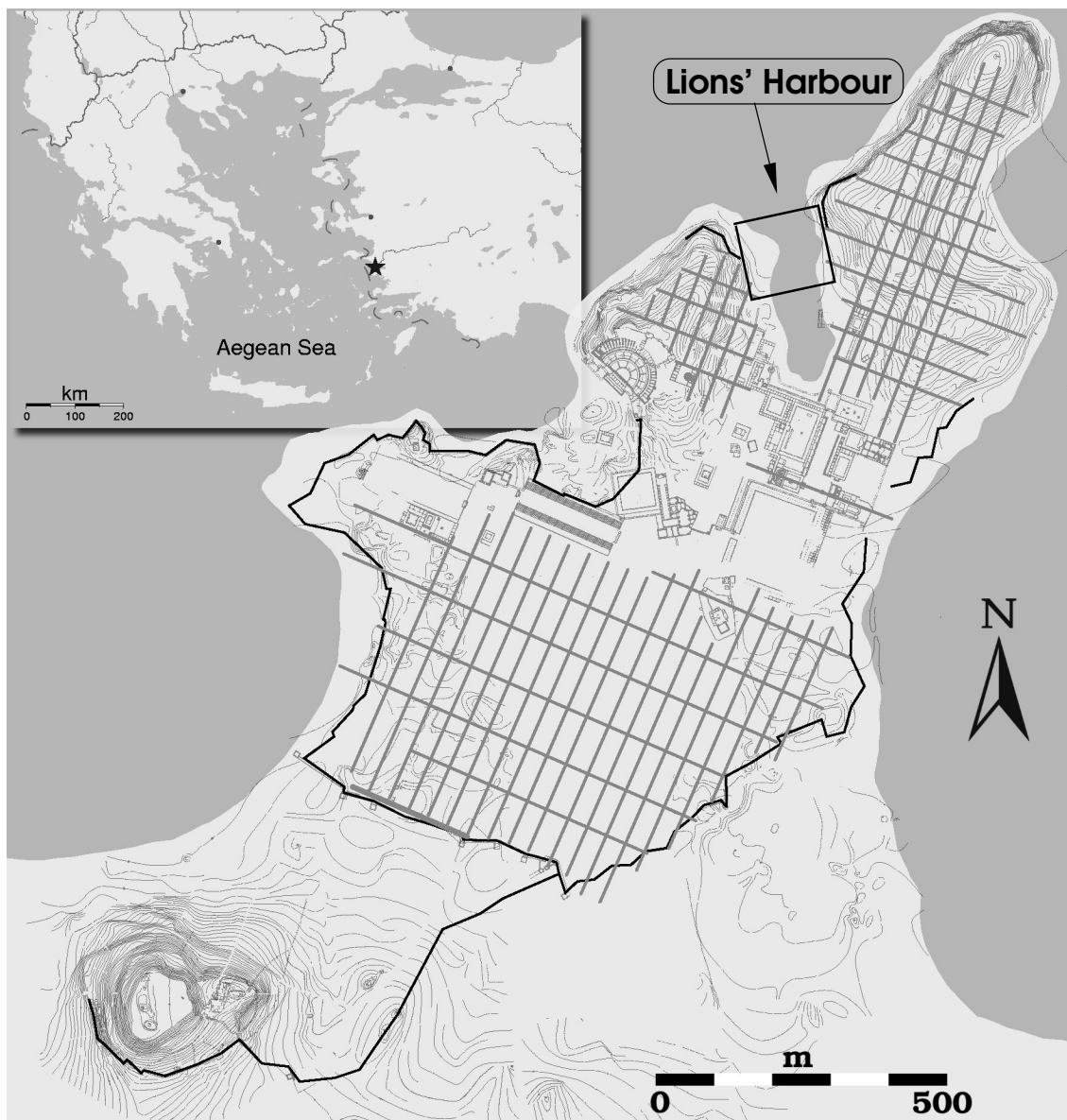


**Figure 2.2:** Map of the Aegean region embedded on the upper left hand corner with location of Miletus near the western coast of Turkey indicated. The enlargement shows a former reconstruction (after Kleiner, 1968) of the ancient town at hellenistic time with a few buildings (theatre, market square), parts of the known city wall and the street system. The Lions' Harbour (follow arrow) located on the city's north-western side and incised deeply into the peninsula. This naturally limestone formed bay is especially suited to serve as a harbour. The area of interest is outlined by a rectangle.



sedimentary infill forms an edge, which outlines the bay. Approximately half of the bay is covered by an up to 1.5 thick layer of debris from former excavations (Tuttahs, 1995). The basin fill was investigated by drilling at two sites (see triangles in Fig. 2.8) where the limestone bedrock was found at 12 m and 21 m, respectively. Both sites showed

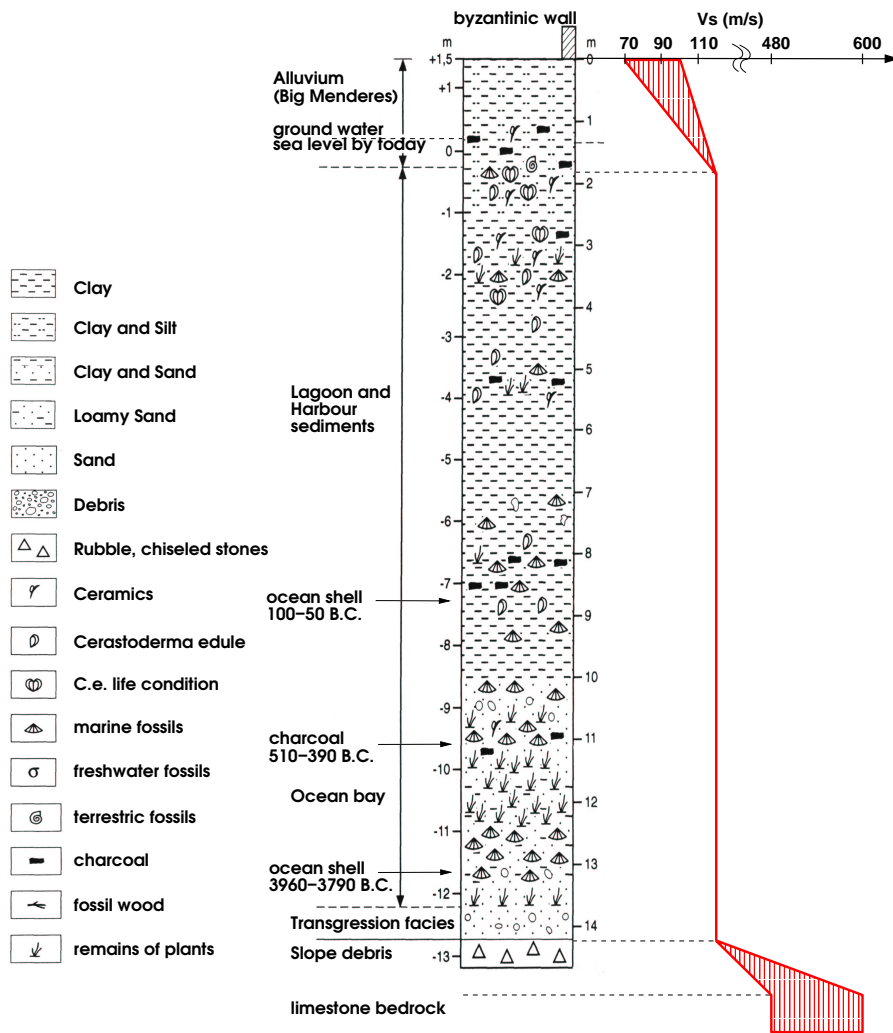


**Figure 2.3:** Coring log holds information about sedimentation of the Lions' Harbour and thus information about progradation of the Menderes River Delta after (Brückner, 1996). Right hand site: velocity profile of Lions' Harbour.

similar stratigraphy (see figure 2.3). The Neogene limestone is truncated by an erosional unconformity. Erosional slope debris of limestone (up to 1 m) was found close to the bottom of the bay. The upward following column comprises marine, lagoon and harbour sediments with shells, charcoal, rest of plants and human artifacts, i.e. ceramics, respectively. From top to bottom the basin fill is rich in clay. Brackish groundwater is found approximately at 1 m depth. The drill cores proved that sedimentation was slow

until 450 B.C. and became more rapid in Hellenistic and especially in Roman times (cf. fig. 2.4). Not later than in Byzantine times the harbour had got a swampy-terrestrial environment and became useless. The geological profiles are representative for the geological situation all over the harbour area (Brückner, 1996; Brückner, 1998; Brückner *et al.*, 2002; Brückner, 2003).

## 2.2 History and Archaeology

Traces of Miletus' settlements go back to the late Chalkolithikum. Oldest architecture testifies a Minoan settlement in the 18th century B.C. up to its destruction in the center of 15th century B.C., a first Mycenaean settlement in the 15/14th century B.C. and after their destruction, a probably fortified settlement in the 13/12th century B.C. under the influence of the Hetitic empire (Niemeier & Niemeier, 1997). On Hetitic clay boards the territory of Büyük and Küçük Menderes is probably named as *Arzawa* with *Pariana* (Priene), *Millawanda* (Miletus) and *Apasa* (Ephesos) (Bay, 1999). In the 12th century B.C. the Hetitic and Mycenic empire was destroyed.

The Greeks colonized the coastal area of Western Anatolia since the 11th century B.C. In the 7/6th century B.C. Miletus developed to a cultural and intellectual center of Asia Minor (*archaic Miletus*) (Brückner, 1996). In respect to protection and trading the outstanding peninsula is a naturally advantageous settlement location. With view of over 80 colonies at the Black Sea and Marmara and connections to Egypt and South Italy, Miletus was called "Ioniae caput" - head of Ionia (Bayhan, 1997). Miletus was the most important center of Ionia philosophy and produced personalities like Thales (Thales Lemma), Anaximandros (invented the sundial), Anaximenes, Hippodamos, Isidoros, and Hekatatios.

At the beginning of the 5th century B.C. Miletus was dominated by the Persians. The Ionian rebellion ended with the destruction of Miletus 494 B.C. after the crucial battle near the former island Lade.

Alexander the Great released the region of the Persians and the *Greek Miletus* was rebuilt fast. 133 B.C. Miletus was assimilated by the Roman Empire and recovered once again. In the *Roman Miletus* the theater, Faustina and other great buildings were extended. Miletus was a rich city but did not represent a leading position anymore.

In Byzanthinic times in the 7/8th century A.D. a castell was built and Miletus had some importance as cathedral town (Bay, 1999). Since 1352 Venice maintained an overseas trading station there. 1412, most harbours long had silted up but still a channel lead to the harbour at the antique theater of Palatia (Miletus' name since the 12th century). The enormous theater and many other outstanding remnants are still visible despite the high age of Miletus. Miletus' longstanding history of settlement makes it to a valuable archaeological site which results on its part in a history of excavation.

Investigations in Miletus began 1446 with the traveler Cyriacus. The chronist Çelebi visited the city 1670 and described Miletus as a city of ruins. The first archaeological

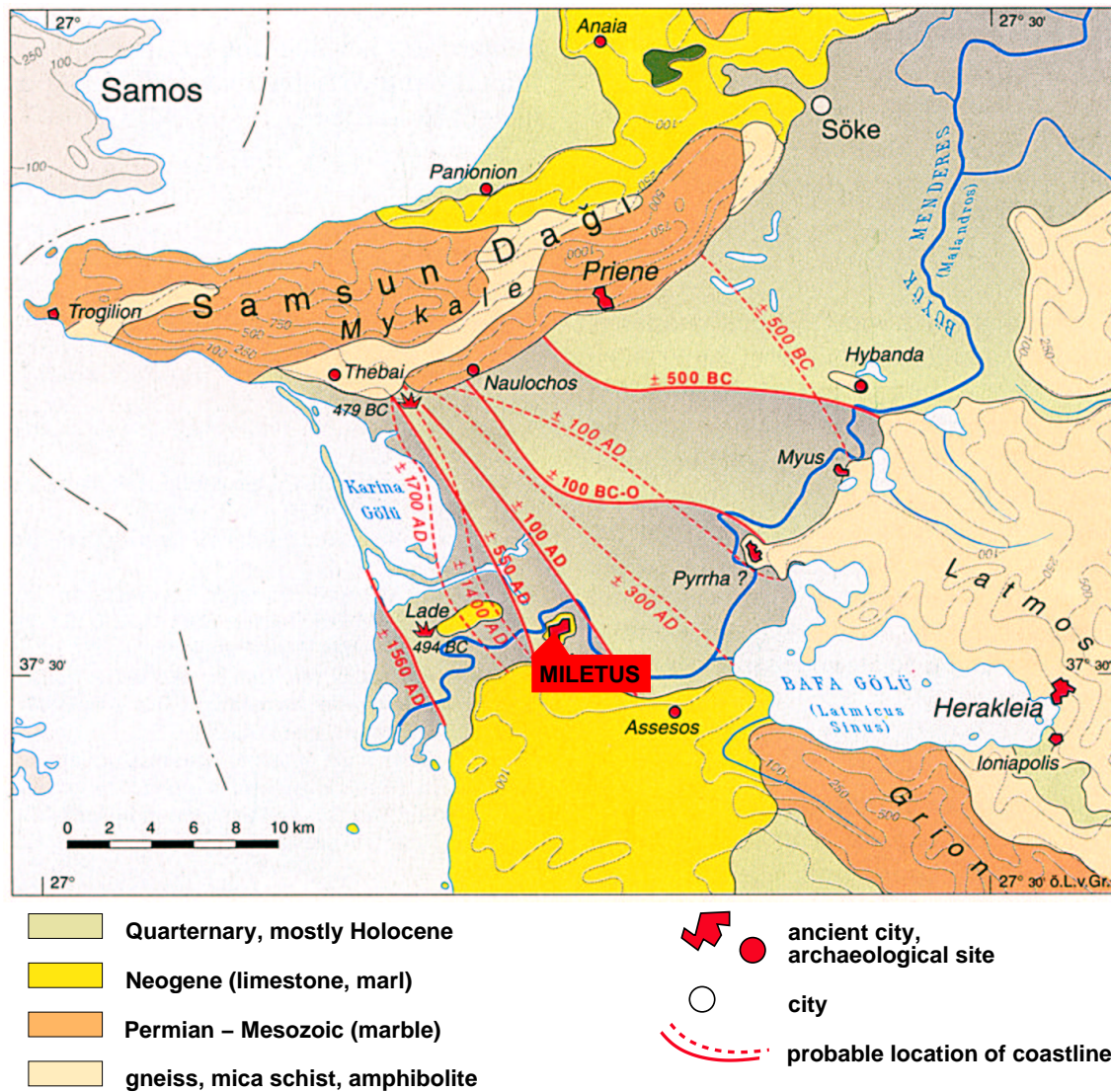


**Figure 2.4:** Scenario for the progradation of the Büyük Menderes delta in historical times. The so-called Latmian Gulf once occupied the alluvial planes and lakes (after Brückner, 1998).



**Figure 2.5:** *Photograph of one of the lion statues uncovered during an excavation campaign 1993 on the eastern side of Lions' Harbour. It's counterpart on the western side was cut in two pieces and shows the destructive traces of history (Graeve, 1996).*

investigations in Miletus were accomplished 1873 by the French archaeologist O. Rayet. However, the systematic study of the ancient city began 1899 under Theodor Wiegand on behalf of the Berlin museums. City fundamentals and a large part of public buildings in the city center were uncovered, e.g. statues, like the two huge lion sculptures of the Lions' Harbour. During World War I the excavations were abandoned and later resumed again under management of C. Weickert and G. Kleiner. Excavation pieces are exhibited in the Pergamon Museum of Berlin.

Since many years excavation and restauration are now directed by Prof. Dr. V. v. Graeve of Ruhr University Bochum on the behalf of the German Research Society (DFG).

The Milet archive at the Ruhr University Bochum contains all attainable text and photo documents from the more than one hundred year old excavation history of Miletus. Miletus today also is a famous tourist attraction.

## 2.3 Geophysical Investigations in Miletus

Since early applications in 1946 (Atkinson, 1952) geophysical investigations became more and more popular as a supporting tool in archaeology. Geophysics not only helps clarifying geological boundary conditions but directly allows for non-destructive mapping of settlement structures.

Today they are an integral part of modern archaeological surveying; moreover preliminary evaluation of unknown terrain usually starts with geophysical work. Geophysical

methods in archaeology range from georadar, geoelectrics and geomagnetics to two and three dimensional seismic surveys. The latter are however still subject to technological development as is demonstrated in this thesis.

In the following we will give an overview of the geophysical work done in the greater area of the city of Miletus and later focus on the specific investigations done in Miletus' Lions' Harbour. There we will put an additional focus on two dimensional seismic work since it must be regarded as the precursor to the work presented in this thesis.

### 2.3.1 The greater city area

The process of determining the extent and structure of the city of Miletus as it is known to day was supported by area wide magnetic measurements acquired over the last decade (Stümpel *et al.*, 1995; Stümpel *et al.*, 1997; Stümpel *et al.*, 1999; Stümpel, 2001). The surveys were conducted using a fluxgate gradiometer array which was carried by two operators and now can be attached to a small tractor to speed up acquisition. Initially, positioning had to rely on traditional geodetic measurements but today it is fully GPS driven. Figure 2.6 documents the status quo of magnetic surveys in Miletus. The most important supporting achievements of these surveys comprise locating and mapping of the inner and outer city walls (CW in the figure), the revelation of the historic street grid's (SG) location and extent, locating the position of city harbours (H1-H4) as well as the "sacred street" (S) and a number of ancient water pipes (WP) and reservoirs (Stümpel *et al.*, 1995; Stümpel *et al.*, 1997).

Other geophysical methods, such as georadar, geoelectrics, and electromagnetics were also applied in Miletus but with less extent. One of the main goals was to evaluate the usefulness of different methods when deployed for archaeological prospecting, regarding penetration, resolution and acquisition speed. In addition, first surveys aimed towards the development of multisensor acquisition techniques were conducted, and the results compared at one of the water pipe locations and the large water reservoir in 1993 (Stümpel *et al.*, 1997). Recently an innovative multisensor acquisition system is developed at Kiel University standardizing and finalizing these studies (Erkul, 2003).

Because the methods just mentioned do not allow for structural depth information at various locations also seismic surveys were deployed. At Kalabaktepe <sup>1</sup>, a 50 m high hill located south of the city center, in total 12 2-D shear wave refraction surveys were acquired for example. The aim of this seismic investigation was to determine the volume of an anthropogenic infill, consisting of settlement debris ("Persian Debris"), which was deposited after the destruction of the city 494 B.C. by the Persians. At the same time the original anticlinal topography of the mountain top was revealed (Stümpel *et al.*, 1999). However, the structure of the subsurface of this location is highly complex, thus recently a follow-up 3-D 9-C seismic survey, cloning the acquisition technique described in this thesis, was conducted. Summary and a more elaborate description is found in (Musmann, 2003).

---

<sup>1</sup>"Tepe" Turkish for "Hill" or "Mountain"



**Figure 2.6:** Status quo of the magnetic surveys performed in Miletus over the last decade. The most important supporting achievements of these surveys are indicated as: (K) Kalabaktepe, (CW) city walls, (SG) street grid, (H1-H4) "Lions' Harbour", "Theater Harbour" and unknown harbours, respectively; (S) "Sacret Street", (WP) water pipe. Further description in text. The enlargement shows the result of magnetic surveys in the Lions' Harbour area.

Historic documents indicate the existence of four harbours in Miletus. The "Lions' Harbour" and the "Theater Harbour" locations are well known, but the two remaining locations are still subject of investigation and discussion (H1 and H2 in figure 2.6). However, magnetic surveying in 1998 and 1999 (Stümpel, 2001) and coring in 2000 (Wullstein, 2001) suggest that one of these harbours was located between the southern inner city wall and Kalabaktepe (H3 in figure 2.6). At this location a number of 2-D refraction seismic surveys were also acquired which in part support this thesis, but could not provide a definite clue.

### 2.3.2 Lions' Harbour

From a geophysical point of view the most thoroughly investigated area in Miletus is the northern part of the Lions' Harbour (in the southern part surveying is hampered by excavation debris). This is motivated by the fact that the ground plans of the harbour buildings and basins are of special importance for the architectonic reconstruction of the city.

The first of a significant number of investigations were two GPR surveys near the lion statues as well as the acquisition of six electric profiles near the dam in 1993 (Stümpel *et al.*, 1995; Stümpel *et al.*, 1997).

GPR could not be extended because the penetration depth of electro-magnetic waves is less than 1 *m* in the area. This is caused by highly conductive clayish sediments and a highly brackish groundwater table. Target statements about the extension of the expected sandy layer above the lion sculptures or a quay wall could not be issued.

Although the differences between the apparent resistance were very small the pseudo-section of electric measurements in the same year gave better results than GPR. In the north-western part (upper left hand corner in fig. 2.8) a zone of increased resistivity appeared at the surface. In the north elongation of this anomaly one of the lion statues is situated. Accompanying drilling showed sandy sediments with shells near the surface which is interpreted as a historic beach building a barrier between harbour area and shoreline.

During the same campaign and in the following years the harbour and adjacent areas were mapped magnetically. The most important result of these surveys are two diffuse elongated anomalies inside the morphologically defined basin zone. The anomalies are 50 *m* long, 100 *m* spaced, parallel to each other and are situated close to the eastern and western harbour boundaries. Since they lead straight away from the ancient city center towards the lion monuments (marked "L" in figure 2.8, cf. photograph 2.5) and because they are parallel to the ancient Milesian street system (cf. Fig. 2.2) the anomalies have been attributed to the remnants of former mole foundations or quay walls (Stümpel *et al.*, 1997).

In order to determine the ancient coastal morphology and topography of the harbour basin a seismic shear wave survey was acquired with refraction profiles arranged perpendicular to the bay axis. The choice of shear wave refraction profiling was motivated on the one hand, by the strong contrast in S-wave velocity between basin fill and basement,

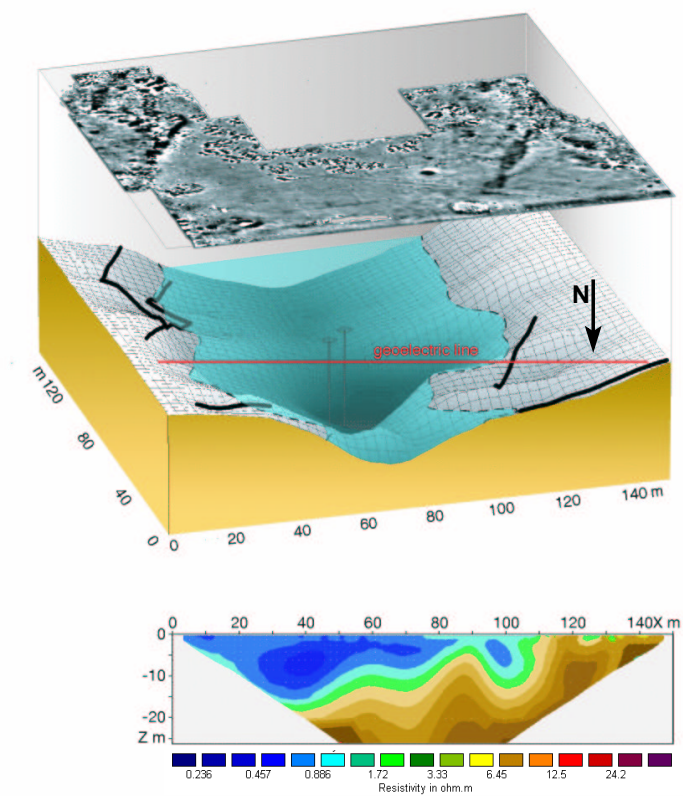


**Figure 2.7:** Model of the harbour basin as resulting from 2-D refraction seismic interpretation, superimposed by a gray-scaled plot of magnetic anomalies. The upper part shows results from an electric survey (pseudosection) acquired parallel to the harbour dam.



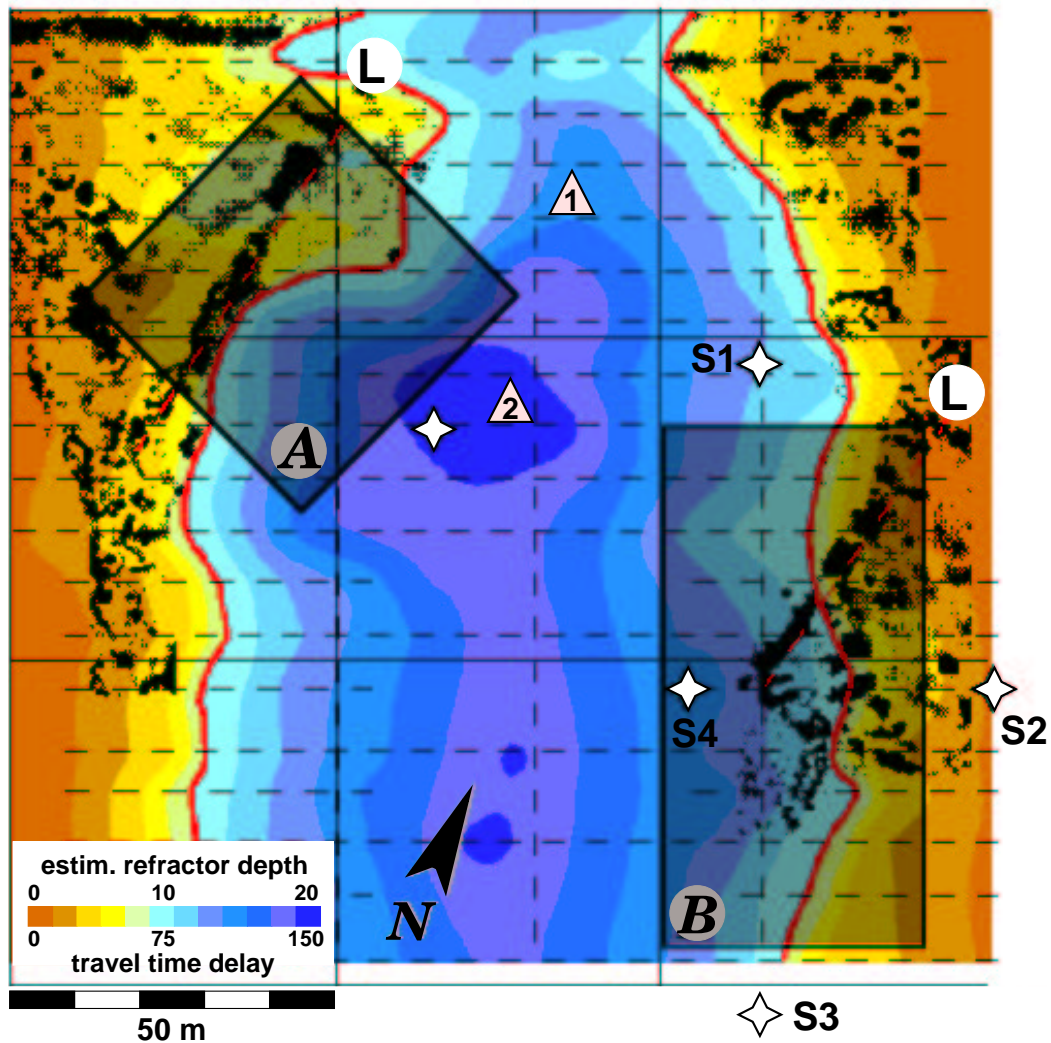


**Figure 2.8:** Contour map of the basin topography of the Lions' Harbour based on single profile seismic measurements with shearwaves (dashed lines). The positions of the lion sculptures are indicated by the letter "L". Partly underlain is a gray scaled magnetic map with strong linear anomalies, which run from the sculptures directly south. These anomalies are supposed to be quay walls or mole foundations of the former harbour. Marked by triangles are two core site locations of accompanying drillings. The square on the upper left hand corner shows the position of the first acquired dense geophone array discussed in this paper as area *A* with the shotpoint (marked with a white star) on its south-eastern edge. Located on the lower right hand side is area *B* with its shotpoints on each side of the area. Both areas cover locations of high interest.

guaranteeing short critical distances, and, on the other hand, by the high  $V_p/V_s$ -ratio providing higher spatial resolution in S than in P. The survey also aimed to elicit the possible existence of mole foundations or walls causing the linear magnetic anomalies described above.

After extensive magnetic surveying work and shearwave refraction seismic a first model of the harbour basin was found (figure 2.8). The derived subsurface model is shown in the middle part of figure 2.7. The basin has asymmetric depth contours with a depth maximum of about 22 m located between the magnetic anomalies. The solid line in Fig. 2.8 is an assumed antique coastal line in about 6 m depth, following an isoline from the seismic results. The linear magnetic anomalies also indicated in the subsurface model (black lines) do not seem to be directly correlated with the basin structure (Stümpel *et al.*, 1995; Stümpel *et al.*, 1997; Stümpel *et al.*, 1999; Stümpel, 2001).

The model was built by interpolating between the 8 m spaced seismic lines, which can cause great inaccuracy. Often energy is not emitted right beneath the seismic line ("3-D side swipe effect" see figure 1.3). As a consequence conventional refraction profiling is not able to deal with complex topography (e.g. strong slopes, corners and edges). Therefore, this first model has to be considered too rough and possibly wrong.

The morphology and topography of the Lions' Harbour as well as the magnetic anomalies in question play an important role for archaeological interpretation. This fact and the principal interest in small scale resolution potential of shear waves motivated the 3-D multi-component refraction seismic surveys presented in this thesis.

## Chapter 3

# Seismic Data Acquisition and Simulation

This section describes the acquisition of three-dimensional multi-component data on the two areas covering magnetic anomalies as indicated in Figure 2.8 ( $\mathcal{A}$  and  $\mathcal{B}$ ) and the simulation of a 3-D 9-C synthetic dataset. While 3-D in this case stands for the combination of two spatial ( $x$  and  $y$ ) with one temporal ( $t$ ) dimension, multi-component specifies the number of components used or generated in the survey, e.g. two source components and two receiver components form a four-component (4-C) dataset.

### 3.1 3-D 4-C

Measurements in 1997 on area  $\mathcal{A}$  cover part of the western linear magnetic anomaly (cf. figure 2.8) which is pointing directly towards one of the lion statues and is aligned to the Milesian street system (cf. figure 2.6). It is situated above an area with strong curvatures and steep slopes known from previous surveys (see section 2.3.2). A principle sketch of the acquisition layout is shown in Figure 1.2.

Geophones were arranged with 1  $m$  grid spacing along linear profiles also separated by 1  $m$  comprising 48 sensors each and pointing WSW to ENE. We used single 10  $Hz$  horizontal shearwave geophones oriented parallel to the grid coordinate axes (Fig. 1.2). The seismic waves, preferably S-waves, were generated by hitting a vertical metal plate with a horizontally led sledge-hammer in two orthogonal directions to excite all possible shear wave components. We thus speak of a vectorial source (2C) and vectorial receivers (2C) for this experiment. The survey area was shot from one shot location situated in the middle of the southeastern survey edge (cf. fig. 2.8). Figure 3.2 shows a photograph of the shotpoint after finishing the survey, where A denotes the metal plate which is hit by the hammer B. N is the propagation direction of horizontal polarized shearwaves. Please note that the hole is extended because of intensive use.

In the following geophone lines, geophone components and hammershot orientations are designated with  $X$  and  $Y$  following the grid coordinate system as illustrated in Figure

Parameters	numerical simulation	survey $A$	survey $B$
size of survey area	$40 \times 27 \text{ m}$	$48 \times 48 \text{ m}$	$40 \times 80 \text{ m}$
number of components	9	4	9
number of shot comp.	3	2	3
number of rec. comp.	3	2	3
number of shot loc.	1	1	4
Sampling rate	$1 \text{ ms}$	$1 \text{ ms}$	$1 \text{ ms}$
recording length	$1000 \text{ ms}$	$1000 \text{ ms}$	$2048 \text{ ms}$
grid spacing	$0.2 \text{ m}$	$1 \text{ m}$	$1 \text{ m}$
excitation	Ricker wavelet $25 \text{ Hz}$	hammer blow $\sim 25 \text{ Hz}$	hammer blow $\sim 25 \text{ Hz}$
$v_p$ surface	$300 - 600 \text{ m/s}$	$\sim 240 \text{ m/s}$	$110 - 250 \text{ m/s}$
$v_p$ bedrock	$950 \text{ m/s}$	no value	$\sim 2000 \text{ m/s}$ (estim.)
$v_s$ surface	$90 - 150 \text{ m/s}$	$\sim 120 \text{ m/s}$	$70 - 120 \text{ m/s}$
$v_s$ bedrock	$590 \text{ m/s}$	$\sim 600 \text{ m/s}$	$\sim 600 \text{ m/s}$

**Table 3.1:** Summarized parameter of synthetic data and field data examples.

1.2.

Each component either receiver or shot was acquired in sequence and line by line. For example, geophones were planted on an inline, oriented in x-direction, and then the shot was fired first in x- and then in y-direction. Subsequently the geophones were arranged to point in y-direction on the same line, to record the second x and y shot sequence. The line was then shifted  $1 \text{ m}$  in crossline direction to acquire the next profile. This procedure was repeated to fill up the  $48 \times 48 \text{ m}$  acquisition area. A 48-channel BISON seismograph was used for recording. Recording time was 1 second with a sampling rate of  $1 \text{ ms}$ , and a dominant signal frequency of  $25 \text{ Hz}$ . Due to a good signal-to-noise ratio two-fold vertical stacking was sufficient on average. Table 3.1 summarizes the main acquisition parameters. In total  $\approx 400$  sledge hammer hits were done and 192 profiles with  $48 \text{ m}$  length were recorded resulting in  $9.2 \text{ km}$  total spread length.

## 3.2 3-D 9-C

Motivated by the success and gained experience of the first measurement a second 3-D multicomponent survey  $B$  was carried out in a two week campaign in 2000. This survey was positioned to cover the second area exhibiting suspicious magnetic anomalies as discussed in section 2.3.2 and seen in figure 2.8, lower right hand side. This anomaly is characterized by a prominent edge suggesting possible man-made structures in the subsurface, such as quay walls or harbour foundations. The acquisition setup for survey  $B$  was comparably complex. The survey covered an area of  $40 \times 81 \text{ m}$  and was surrounded

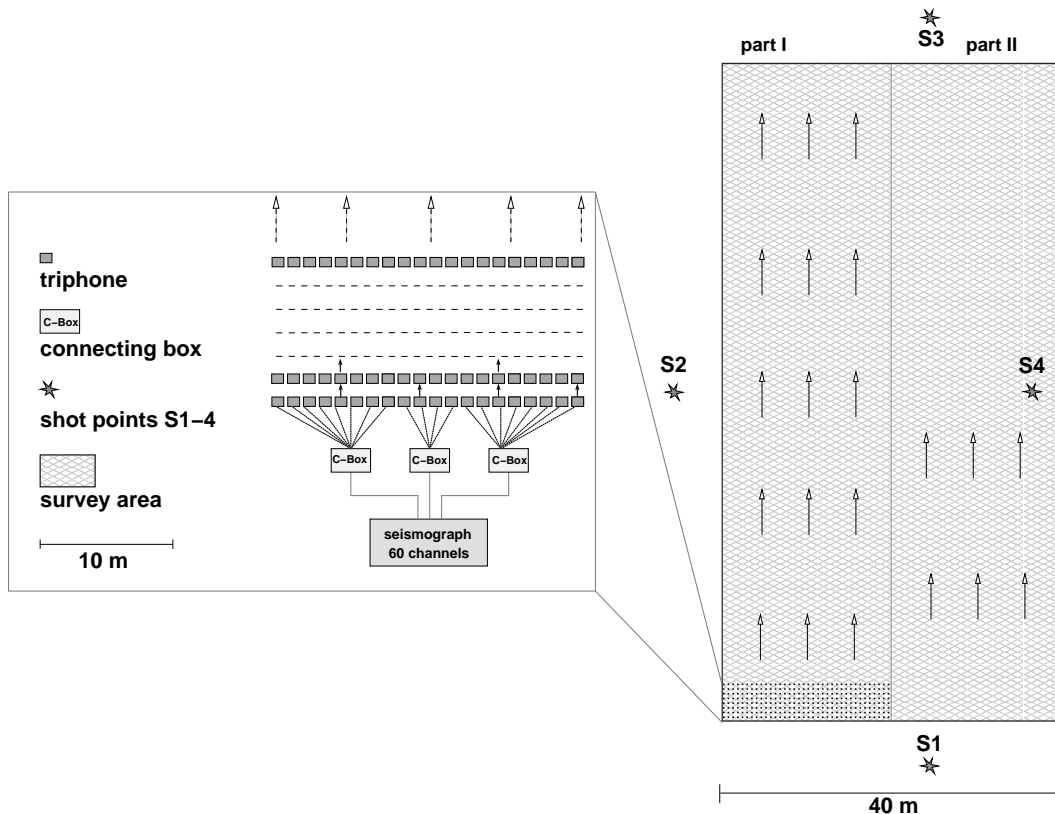


**Figure 3.1:** Acquisition setup for survey B, covering an area of  $40 \times 81$  m. 20 three-component Gal'perin geophones were deployed with 1 m spacing to simultaneously record data for each shot with a 60 – channel Geometrics seismograph. Each profile only covered half the width of the acquisition area. To complete one full-width line, the geophones had to be moved once by 20 m. Four three-component shotpoints were fired in sequence before the line was moved. This procedure was repeated 81 times to complete the survey.

by four shotpoints. A principle sketch of the acquisition layout and concept is shown in Figure 3.1.

This time not only two, but three components were used on the source and on the receiver side, respectively. Four three-component shotpoints were fired in sequence before the line was moved. The horizontal shot components were realized as in survey A. The vertical shot component was realized by vertically hitting a plate lying on the ground. 20 three-component Gal'perin geophones (see figure 3.2) were deployed with 1 m spacing to simultaneously record data for each shot with a 60 – channel Geometrics seismograph. Each profile only covered half the width of the acquisition area. Thus, to complete one full-width line, the geophones had to be moved once by 20 m. This procedure was repeated 81 times to complete the survey. For the location of the shotpoints please refer to figure 2.8. Table 3.1 also summarizes all acquisition parameter for this survey.

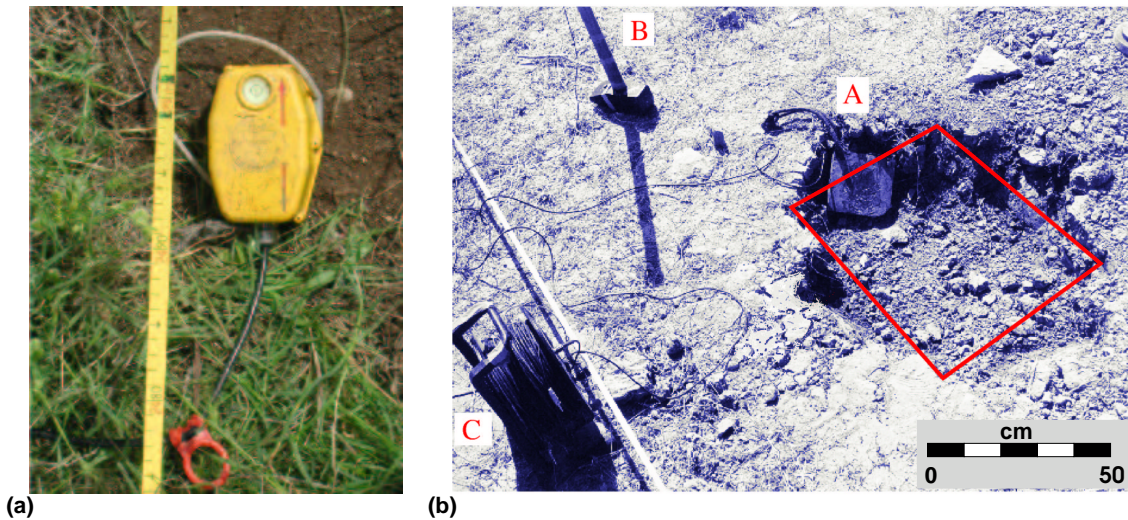


**Figure 3.2:** Panel a: Photograph of a planted Gal'perin triphone used in survey B. Planting was aggravated by extremely hard soil and coupling was difficult due to significant mudcracks and tamarisk roots (cf. figure 3.3). Panel b: Deformation of the source hole from its original shape (frame) is evident. Also shown are a metal source plate (A), a sledgehammer (B), trigger wiring (C).

Problems in geophone coupling were caused by deep mud cracks originating from the flooding during the winter and a lack of rain during spring and the hot summer in this region. Figure 3.3 shows a photograph of the location of the survey area and enlarged a photograph of these mud cracks. The cracks made planting the geophones with their two or three spikes a real challenge and only with the aid of drill machines resp. chisels we succeeded in firmly attaching the geophones to the ground.

Because of the difficult acquisition conditions the area was mapped visually during the survey (see figure A.1) to be able to later correlate possible seismic artefacts with direct surface influence.

In total nearly 8000 hammer blows were done and 5832 profiles with 20 m length resulting in 16.6 km total spread length were acquired. This makes this survey over ten times more laborious than survey A, not only noticeable in campaign duration but also in blisters on Turkish shooters' hands.

### 3.3 Synthetic Data

In order to support and accompany interpretation of the field data and subsequent processing, a synthetic seismic survey was conducted simulating acquisition geometry resembling survey A. On the one hand, this is aimed to better understand wavefield behavior with respect to the acquisition geometry. On the other hand, this synthetic data



**Figure 3.3:** *Photograph of the Lions' Harbour area seen from the North-East with the approximate location of the survey area. Enlarged in the lower right hand corner the very dry soil of this area as found during the acquisition campaign on area  $\mathcal{B}$  is displayed. The up to 20cm deep mud cracks cause badly coupled receivers as well as bad quality of source points. They also cause difficulties with planting the geophones and are responsible for non-radial symmetric wave propagation. The photography in the lower left hand corner shows Turkish worker standing on a pile of tamarisks that had to be stubbed.*

set serves to evaluate and verify the different wavefield separation methods developed in this thesis. To provide comparability and to account for the special setup of the survey a parallel 3-D viscoelastic finite-difference (FD) software (Bohlen, 2002) was used. The FD algorithm uses conventional 2nd order FD operators in time and 4th order operators in space on a staggered grid (Levander, 1988; Robertsson *et al.*, 1994). The algorithm simulates propagation, reflection, refraction and scattering of seismic waves in isotropic, variable heterogeneous 2-D and 3-D media. FD simulation is regarded as an exact method because the wave equation is solved numerically without any approximations. The subsurface model is projected onto a regular grid and for each time step the entire wavefield is calculated everywhere in the 3-D model. In order to include viscoelastic effects in the simulations a GSLS (generalized standard linear solid) is used allowing to calculate arbitrary absorption  $Q(\omega)$ . The program can simulate different types of sources including a single vector force. An absorbing layer around the model suppresses boundary reflections.

---

In our case a homogeneous halfspace has been chosen and is sufficient to illustrate the performance of wavefield separation techniques discussed in this thesis. For modeling parameter please refer to table 3.1. These parameters are chosen to resemble the real situation as closely as possible in order to also allow for direct comparison of field data and synthetic results.



# Chapter 4

## Processing and Imaging Methodology

This chapter describes the generic preprocessing, data display concepts and wavefield separation techniques necessary to understand complex 3-D datasets. After adequate geophone orientations for each wave type are simulated computationally and thus, wavefield separation is achieved, refractor imaging is possible. In theory an optimization of separated wavefield amplitudes can be performed by taking into account the vector shot components. In practice, however, this proves to be difficult as will be discussed in the section thereafter. Finalizing this chapter, a new refractor imaging concept for 3-D refraction seismic data sets will be introduced.

### 4.1 Generic preprocessing and data display

The data acquired as described in the previous chapter (3) are of very good quality (see figure 1.3, left hand side). This is caused by a more or less homogeneous basin filling, a good velocity contrast between sediment and bedrock and the relative lack of anthropogenic noise. However, due to the acquisition concept, setup and sequence prior to any other high-level processing, first of all the data have to be prepared by a basic processing sequence comprising the following steps (for a more detailed overview please refer to appendix A):

- rotation from Gal'perin into Cartesian coordinate system (for Gal'perin rotation please refer to appendix A, figure A.2)
- sorting into common shot gathers
- splitting into common shot component gathers and common receiver component gathers

This process e.g. for survey  $B$  led to 36 data sets of about 27Mb each ( $\approx 1Gb$  in total). For different processing steps it is necessary to amplify the data by applying a multi-component AGC (i.e. two- or three-component AGC ) in order to emphasize late arrivals while preserving amplitude ratios. After preprocessing the acquisition configura-

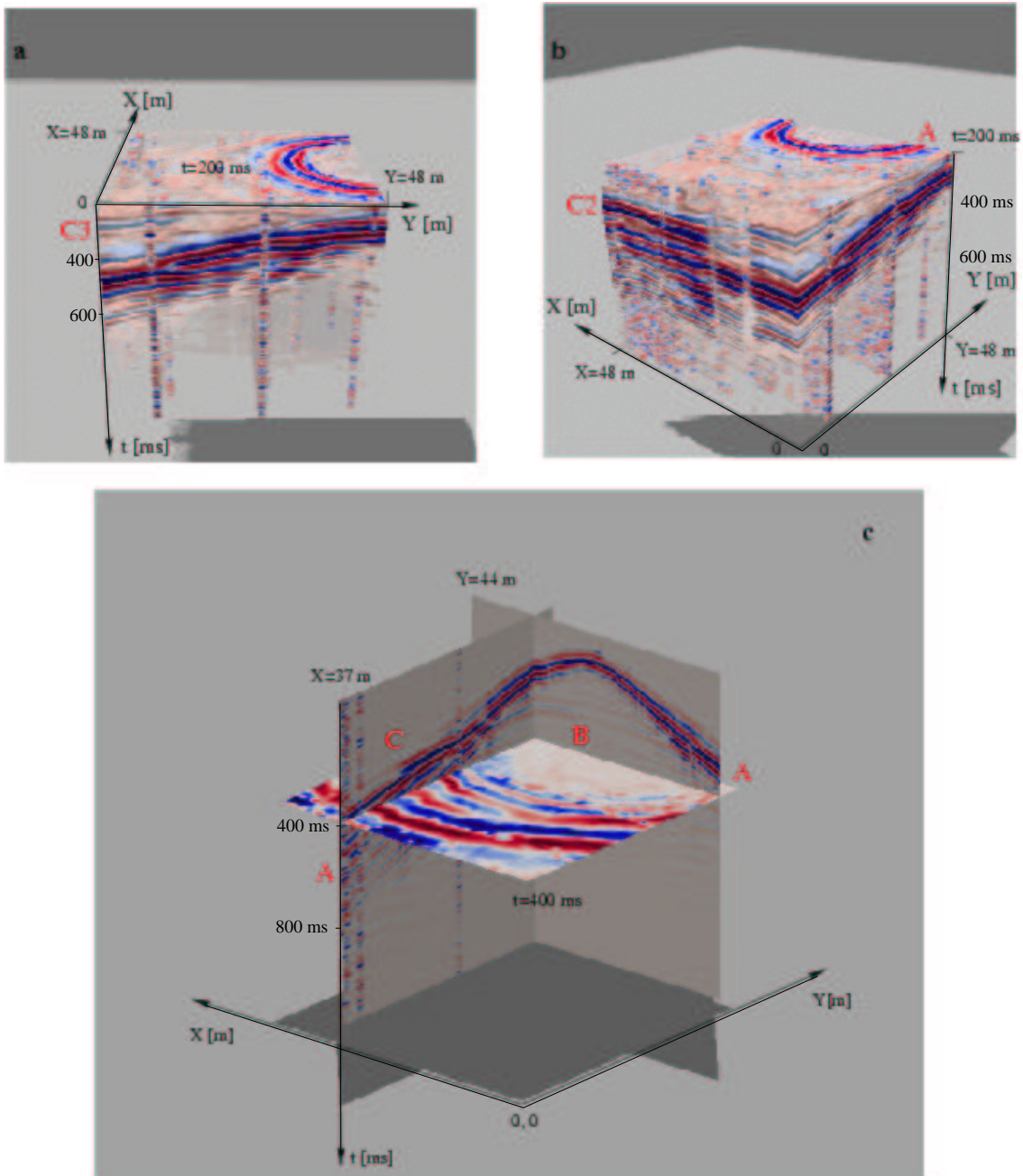


**Figure 4.1:** Volumetric display of data set  $\mathcal{A}$ , panel (a) and (b). Amplitude values close to zero were rendered transparently. Seen from above is a timeslice at 200 ms. To the side the refraction (C2 and C3) is clearly identified. Panel (c) shows the direct wave with Love wavefield (A), the refraction C and a weak reflection B in a composition of crossline, inline, and timeslice, respectively.

tion results in four single component datasets for area  $\mathcal{A}$  (see fig. 5.2) and nine single component datasets per shotpoint for area  $\mathcal{B}$ . For two-dimensional geophone spreads the recorded wavefields are not presented as usual by seismogram sections, but in data blocks. Such data blocks or data cubes combine two spatial ( $x$  and  $y$ ) with one temporal ( $t$ ) coordinate and thus represent the extension of a "usual" seismogram ( $\mathbf{u}(x, t)$ ) into a two-dimensional seismogram ( $\mathbf{u}(x, y, t)$ ). Since geophones are based on the principle of induction, seismograms  $\mathbf{u}$  represent particle velocity, that is  $\mathbf{u} = \dot{\mathbf{U}}(x, y, t)$  where  $\mathbf{U}$  is displacement. In our case  $\mathbf{u} = (u_x, u_y)'$  for experiment  $\mathcal{A}$  and  $\mathbf{u} = (u_x, u_y, u_z)'$  for experiment  $\mathcal{B}$  where "' denotes "transpose". Although data may be represented in 3-D views by opacity amplitude coding (volume rendering/volumetric display) we found it necessary to combine various 2-D sections for a reliable interpretation, for example, inline ( $\mathbf{u}(x_0, y, t)$ ), crossline ( $\mathbf{u}(x, y_0, t)$ ) or radial seismogram section ( $\mathbf{u}(x, y(x), t)$ ) and time slices ( $\mathbf{u}(x, y, t_0)$ ), which form two-dimensional subspaces of these blocks. The volumetric view of one of the data cubes of area  $\mathcal{A}$  gives an impression of the spatial interference of body and surface waves (figure 4.1). Panels (a) and (b) of figure 4.1 show the whole data set where the upper 200 ms were removed to provide a better "insight" into the data. Amplitude values close to zero are rendered transparently. Seen from above is a timeslice at 200 ms and the refraction  $C2$  and  $C3$  is clearly identified at the side (panel a and b). Panel (c) shows the direct wave with Love wavefield ( $A$ ), the refraction  $C$  and a weak reflection  $B$  in a composition of crossline, inline, and timeslice, respectively. These views allow for excellent illustration of the wavefield propagation in three dimensions and correlation of events. The volumetric display is a consequent extension of the seismogram concept to the 3-D case.

Since timeslice sequences are better suited to understand the spatial and temporal connection of propagating wavefields than volume displays, we display data mainly as time slice sequences in the following.

The vertical shot component as well as the vertical receiver component of survey  $\mathcal{B}$  is not used in this discussion, because these components are not essential for the shearwave processing and/or wavefield separation approaches used here. Moreover compressional wave energy quickly escapes by refracting in the water table (as is illustrated in figure 1.1) and thus is of little use in the Lions' Harbour. Besides some rather cosmetic bandpass filtering and AGC application for plotting, the further processing consists of applying different wavefield separation methods in order to find adequate source and receiver orientation for the considered wave types.

## 4.2 Wavefield separation

The multicomponent acquisition approach discussed in chapter 3 allows for reconstruction of any geophone or source orientation possible. For wavefield separation it is only necessary to look at the receiver side. We will now describe three different ways to decompose the recorded wavefield into its transversely and radially polarized constituents:

- A pure geometrical approach for wavefield separation.

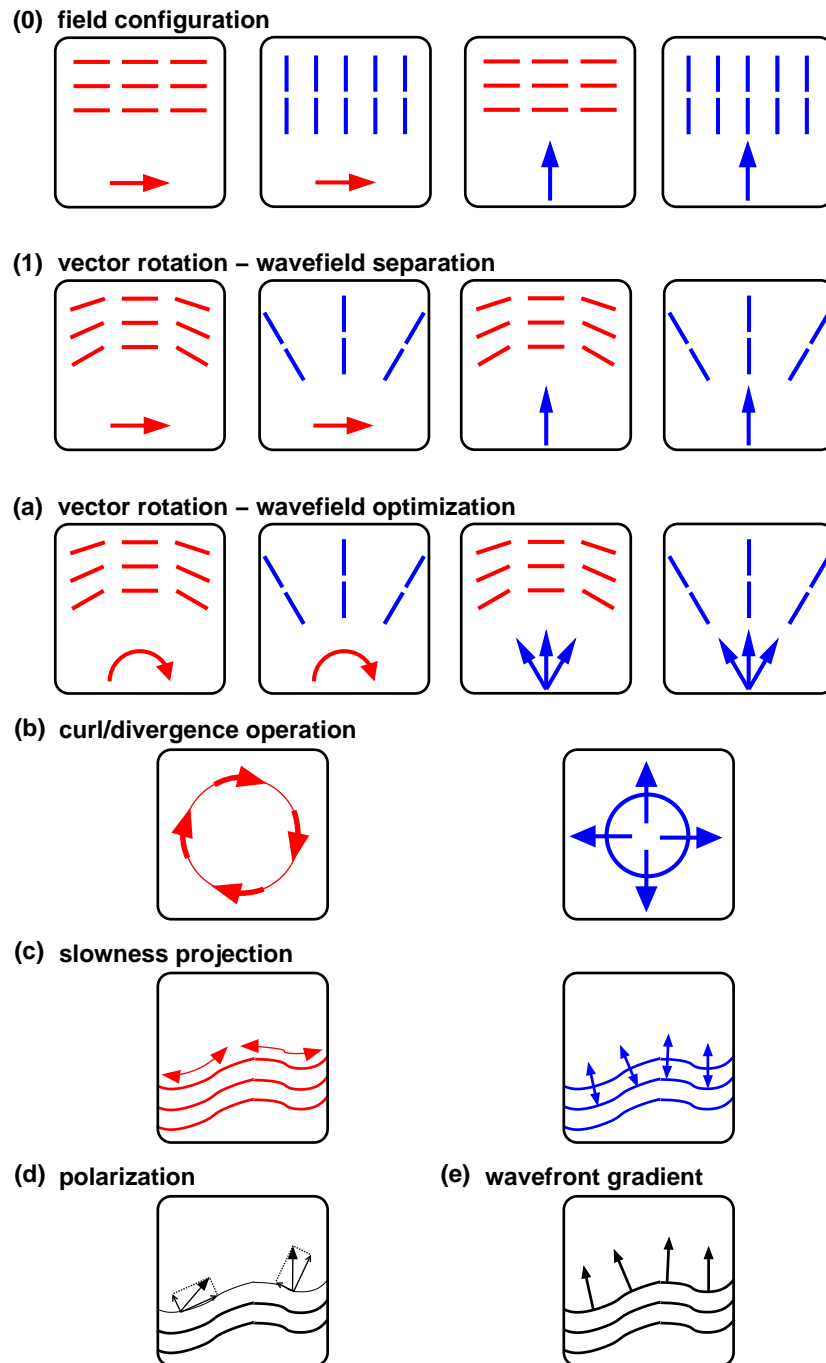
- Applying the curl and divergence operations to separate radial and transverse movements in the horizontal plane of elastic wavefields (Dellinger & J., 1990; Robertsson & Muzyert, 1999).
- Calculating the horizontal slowness and projecting  $\mathbf{u}$  into the azimuth of ray propagation.

Figure 4.2 shows an icon set illustrating the original field acquisition source and receiver component combinations (panel 0). The arrow in the lower part of the icons indicate the shot direction, whereas the set of lines in the upper part of the icons indicates the receiver orientation. The corresponding Cartesian coordinate system x-axis is pointing to the right and the y-axis is pointing up. For example, icon three in panel (0) refers to a shot in y-direction recorded with receivers in x-direction. The other icons in fig. 4.2 will be explained alongside with the corresponding wavefield separation and optimization methods. The icons will be used later in the thesis to label field data, as well as synthetic data examples.

All the methods described in the following were evaluated with a synthetic seismic dataset resembling survey  $\mathcal{A}$  (section 3.3). Figure 4.3 displays timeslices of the synthetic wavefield  $u_i^j(x, y, t_0)$  for  $t_0 = 180 \text{ ms}$ , where  $i = x, y$  indicates the receiver and  $j = X, Y$  indicates the shot component. We thus have a  $2 \times 2$  matrix for each location within a timeslice. They are labeled by acquisition geometry icons described above. Simulated was a single force source emitting elastic P and S wave energy with a typical radiation pattern as described in e.g. Kähler & Meissner (1983). It becomes obvious that due to the acquisition geometry and source-receiver orientations different wavefield constituents intermingle. Clearly seen is the source radiation pattern which causes incoherent amplitudes and phase reversals in addition to the influence of the receiver orientation. Wavefield amplitudes are overprinted by receiver orientation geometry factor, causing amplitude variations with azimuth and phase reversals. For example in fig. 4.3 (a) and (d) we observe mixing of direct SH wave and Rayleigh wave indicated by circles. At the same time the direct P wave, Rayleigh wave and SH wave exhibit azimuthal amplitude variations, as can be seen in all panels of the figure. In panel (b) and (c) we observe an obvious phase reversal of the SH wave and the Rayleigh wave, respectively. The synthetic examples show the need to virtually change the original field acquisition shot- and receiver-orientation in order to compensate or even eliminate these effects.

### 4.2.1 Basic vector rotations

Due to the Cartesian acquisition geometry the rather spherical or cylindrical symmetry of wave propagation and vectorial character of particle displacement different wave types mix differently onto individual geophone components. In order to ease interpretation geophones have to be virtually rotated into a cylinder symmetric coordinate system. Although cylinder symmetry is applicable only to wave propagation in 1-D media in a strict sense our data examples show that it may be a reasonable first order approximation even in 3-D media. The recording of two orthogonal geophone orientations, enables us to



**Figure 4.2:** Icon set to display different acquisition configurations or separation and optimization approaches: (0) original field configurations, standing for the four recorded components of a 4C data set; (1) modified receiver orientations after vector rotation, where the two left are the transverse and the two right are the radial configurations; (a) modified source and receiver orientations after vector rotation and source optimization; (b) separated wavefield by curl (left) and divergence (right) estimation; (c) horizontal slowness projection with components rotated into the ray coordinate system, parallel to the wavefront (left) and parallel to the ray (right); (d) horizontal polarization vector; (e) horizontal slowness vector.

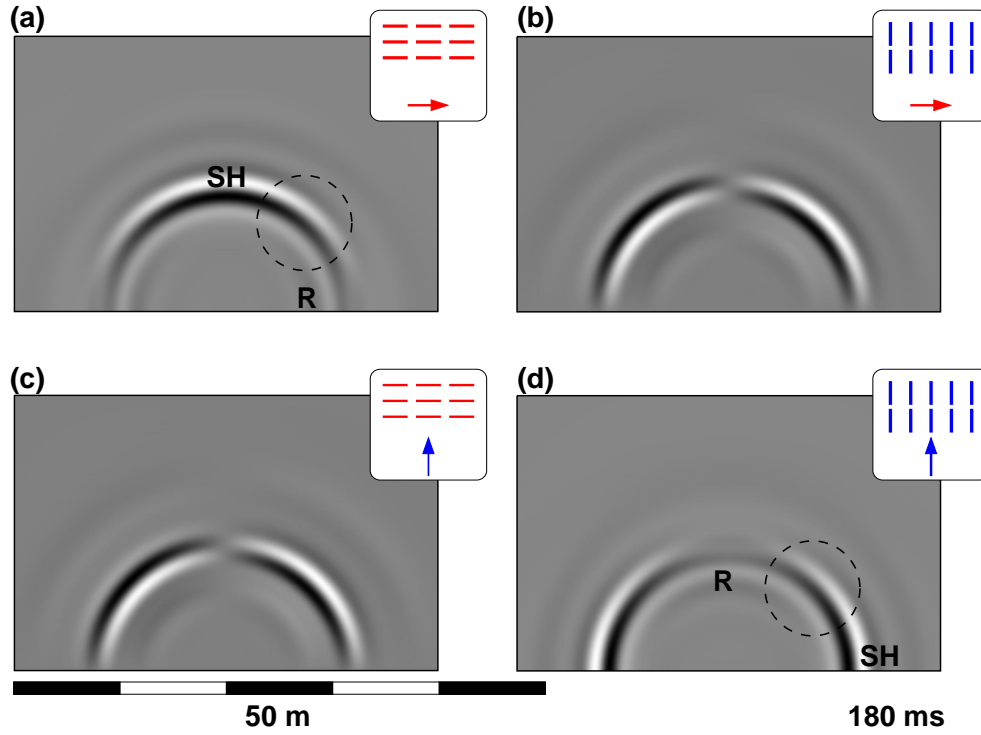


**Figure 4.3:** Synthetic data of four single components with icons indicating the source and receiver orientations on the spread. Clearly seen are source radiation pattern and the intermixing wavefields of P, S, Rayleigh and Love wave due to receiver geometry.

simulate any geophone orientation by elementary vector operations, such as vector addition and rotation of the coordinate system. Thus, the most obvious and easiest way to separate the individual seismic wavefields follows this geometrical concept. Assuming the wavefield traveling along a straight line between source and individual receiver location, we virtually rotate the individual receiver components to point parallel and perpendicular to this direction.

$$\begin{pmatrix} u_t^X \\ u_t^Y \end{pmatrix} = \begin{pmatrix} \cos\alpha & \sin\alpha & 0 & 0 \\ 0 & 0 & \cos\alpha & \sin\alpha \end{pmatrix} \begin{pmatrix} u_x^X \\ u_y^X \\ u_x^Y \\ u_y^Y \end{pmatrix} \quad (4.1)$$

Let  $u_x^X(t)$ ,  $u_x^Y(t)$  and  $u_y^X(t)$ ,  $u_y^Y(t)$  be the four time series recorded for each geophone location, where  $X$  and  $Y$  are the respective shot orientations, and  $x$  and  $y$  are the

geophone orientations. By the use of equations 4.1 and 4.2 we can compute the virtual records of shots  $X$  and  $Y$  for an arbitrary horizontal geophone orientational corresponding to angle  $\alpha$  in the  $x, y$ -coordinate system.

$$\begin{pmatrix} u_r^X \\ u_r^Y \end{pmatrix} = \begin{pmatrix} 0 & 0 & -\sin \alpha & \cos \alpha \\ -\sin \alpha & \cos \alpha & 0 & 0 \end{pmatrix} \begin{pmatrix} u_x^X \\ u_y^X \\ u_x^Y \\ u_y^Y \end{pmatrix} \quad (4.2)$$

$u_t^X$  and  $u_t^Y$  are the transverse wavefield constituents of the shots in  $X$  and  $Y$  direction, and  $u_r^X$  and  $u_r^Y$  are the longitudinal wavefield constituents of the shots in  $X$  and  $Y$  direction, respectively.

Equations 4.1 and 4.2 are applied to our datasets in order to simulate individual geophone orientations for each geophone location corresponding to "transverse" and "radial" configurations. The icon corresponding to this approach and its individual configurations are displayed in figure 4.2, panel (1). In transverse configuration, for example, the receivers are oriented tangentially to circles around the shotpoint. In the radial configuration each receiver is arranged parallel to an imaginary connecting line between the source point and a receiver point. Although derived for 1-D media these configurations simplify the interpretation of the recorded wavefield often also in 3-D media, if ray paths are not too strongly bended in the horizontal plane.

The wavefield is now successfully separated into its pure SH and P/SV/Rayleigh wavefields. However, the underlying assumption of the straight raypath, connecting source and receiver doesn't necessarily hold for field wave propagation, nor does it hold for refracted or reflected wavefield amplitudes. This inherent problem will be discussed by field data examples in chapter 5.

### 4.2.2 Vector field operations *curl* and *divergence*

The elastic particle displacement field  $\mathbf{U}$  can be written as the sum of the gradient and the curl of a scalar and a vector potential, respectively (Morse & Feshbach, 1953):

$$\mathbf{U} = \nabla\psi + \nabla \times \mathbf{A} \quad (4.3)$$

It can be shown that

$$\mathbf{A} = \int_V \frac{\nabla \times \mathbf{U}}{4\pi R} dV \quad (4.4)$$

and

$$\psi = - \int_V \frac{\nabla \cdot \mathbf{U}}{4\pi R} dV \quad (4.5)$$

Moreover the shear energy density  $E_S$  and the compressional energy density  $E_C$  of an elastic wavefield are calculated by using the following equations (Dougherty & Stephen, 1988):

$$E_S = \mu(-\nabla \times \mathbf{U})^2 \quad (4.6)$$

$$E_C = (\lambda + 2\mu)(\nabla \cdot \mathbf{U})^2 \quad (4.7)$$

Thus we have the means to separate transverse and radial wavefield constituents by applying the above equations. However, the resulting fields  $E_S$  and  $E_C$  will only represent the energy density of the wavefield and not the amplitudes. In order to fully estimate  $E_S$  and  $E_C$  not only a horizontal but also a vertical distribution of seismic sensors would be necessary for the calculation of the vector operations curl and divergence. In our case we can only partly calculate  $E_S$  and  $E_C$  since we are lacking a vertical derivative estimate  $\frac{\partial \mathbf{U}}{\partial z}$ . Equation 4.6 and 4.7 now read for the partial energy densities ( $E'_S$  and  $E'_C$ ):

$$E'_S = \mu \left( \frac{\partial U_x}{\partial y} - \frac{\partial U_y}{\partial x} \right)^2 \quad (4.8)$$

$$E'_C = (\lambda + 2\mu) \left( \frac{\partial U_x}{\partial x} + \frac{\partial U_y}{\partial y} \right)^2 \quad (4.9)$$

After applying eq.4.8 to fields  $\mathbf{U}^X$  corresponding to the shot in x-direction and  $\mathbf{U}^Y$  corresponding to the shot in y-direction we obtain part of the pure shearwave energy density,  $E_S^X$  and  $E_S^Y$ , emitted by the sources. The analogous procedure using eq. 4.9 yields the energy density corresponding to the pure radially polarized wavefield ( $E_C^X$  and  $E_C^Y$ ). Figure 4.2, panel (b) shows the icons corresponding to this wavefield separation method (curl to the left and divergence to the right).

Please note, that because geophones record particle velocities instead of displacement, that is  $\mathbf{u} = \dot{\mathbf{U}}$  instead of  $\mathbf{U}$ , and also for the sake of a simple implementation, the exact procedure used here is described by the following equations:

$$\mathcal{P}_S^X = \left( \frac{\partial u_x^X}{\partial y} - \frac{\partial u_y^X}{\partial x} \right) \quad (4.10)$$

$$\mathcal{P}_S^Y = \left( \frac{\partial u_x^Y}{\partial y} - \frac{\partial u_y^Y}{\partial x} \right) \quad (4.11)$$

$\mathcal{P}_S^X$  and  $\mathcal{P}_S^Y$  are proportional to the power and related to  $E_S^X$  and  $E_S^Y$ , respectively. In complete analogy the procedure to yield a representation for the radial wave powers  $\mathcal{P}_C$  is implemented:

$$\mathcal{P}_C^X = \left( \frac{\partial u_x^X}{\partial x} + \frac{\partial u_y^X}{\partial y} \right) \quad (4.12)$$



$$\mathcal{P}_C^Y = \left( \frac{\partial u_x^Y}{\partial x} + \frac{\partial u_y^Y}{\partial y} \right) \quad (4.13)$$

Compared to the vector rotation method described initially this method not only holds for direct waves and media with laterally changing velocity field, but also for refracted and reflected seismic waves. It is applicable even to interfering wavetrains of different polarization. However for field applications there are some limitations to the method as will be discussed in chapter 5.

The divergence and curl vector operations are only approximated for wavefields recorded on a finite regular grid. Thus, their accuracy depends on the grid spacing. For the dominant frequencies used in this experiment we experienced that a grid spacing of 1 *m* even for synthetic data and the complete absence of noise is not sufficient to produce a satisfactory result. Therefore a third approach was investigated.

### 4.2.3 Slowness projection (ray coordinate system)

If the local azimuth of the wavefront normal is known radial and transverse polarization can be distinguish by projecting the wavefield onto this slowness or ray direction. One way to obtain this direction is to calculate the gradient of the wavefield energy *E* or power *P*, respectively:

$$P = \sqrt{u_x^{X^2} + u_x^{Y^2} + u_y^{X^2} + u_y^{Y^2}} \quad (4.14)$$

Since the gradient oscillates in ray direction it has to be multiplied with the wavefield powers time derivative  $sign(\frac{\partial P}{\partial t})$  in order to create a vector pointing in the direction of wave propagation. Thus the ray direction  $\hat{n}$  is given by:

$$\hat{n} = (n_1, n_2)' = sign\left(\frac{\partial P}{\partial t}\right) \frac{\nabla P}{|\nabla P|} \quad (4.15)$$

Wavefield separation can now be performed by projecting the wavefield vectors of each shot onto the ray direction  $\hat{n}$  and onto the perpendicular direction  $\hat{p}$ , parallel to the wavefront:

$$\hat{p} = (-n_2, n_1) \quad (4.16)$$

Hereby we already obtain pure transversely and pure radially polarized wavefields for the two different shots.

$$u_t^X = \hat{p} \cdot \mathbf{u}^X(x, y) \quad \text{and} \quad u_t^Y = \hat{p} \cdot \mathbf{u}^Y(x, y) \quad (4.17)$$

$$u_r^X = \hat{n} \cdot \mathbf{u}^X(x, y) \quad \text{and} \quad u_r^Y = \hat{n} \cdot \mathbf{u}^Y(x, y) \quad (4.18)$$

Again figure 4.2, panel c displays sketches of this method used as icons for the data example. Since we are using a data driven approach this method not only applies to the

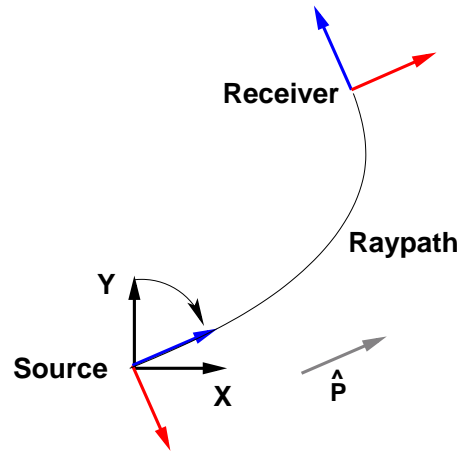


**Figure 4.4:** The shot components have to be rotated into the ray coordinate system corresponding to the ray emerging from the shot and approaching the receiver.  $\hat{p}$  gives the ray direction at the source.

direct wavefields, but also to the refracted and reflected events. Keeping in mind the difficulties encountered with the curl and divergence estimations we expect the current approach to be the most reliable when applied to field data.

### 4.3 Wavefield Optimization

After wavefield separation the individual constituents  $\mathbf{u}_t$  and  $\mathbf{u}_r$ , resp.  $\mathbf{P}_S$  and  $\mathbf{P}_C$  are still overprinted by the source radiation pattern. To remove this imprint the shot components have to be virtually rotated to be parallel and perpendicular to the horizontal direction of the ray emerging from the shot as it corresponds to the ray arriving at the receiver (see sketch 4.4). Here this procedure is referred to as wavefield optimization. Due to reciprocity of respective elements of the Green's tensor (Aki & Richards, 2002), this rotation may also be seen as a projection of the longitudinal wavefields of shot X and shot Y ( $\mathbf{u}_r = (u_r^X, u_r^Y)'$ ) onto the ray direction  $\hat{p}$  at the source and a projection of the transverse wavefields of shot X and shot Y ( $\mathbf{u}_t = (u_t^X, u_t^Y)'$ ) onto the perpendicular direction  $\hat{n}$ :

$$\tilde{u}_t = \hat{p} \cdot \mathbf{u}_t(x, y) \quad \tilde{u}_r = \hat{n} \cdot \mathbf{u}_r(x, y) \quad (4.19)$$

$\tilde{u}_t$  and  $\tilde{u}_r$  are the optimized longitudinal and transverse wavefields, respectively. Panel (a) in figure 4.2 shows the corresponding icons (left and right side). Please note that the second and third icon refer to configurations which in theory yield zero amplitudes. In the following the configuration corresponding to icon 1 will be referred to as *transverse configuration* and icon 4 will be referred to as *radial configuration*. "Transverse" and "radial" refer to a shot-and-geophone orientation perpendicular and parallel to the

horizontal ray direction, respectively.

For the surface wavefield  $\hat{p}$  can be estimated by the straight line connecting source and receiver if the variation of the surface velocity field is not too strong. In the following this approach is used whenever the discussion is focused on the optimization of separated surface wavefields. Figure 4.5, panel (a) shows the results after separating by simple wavefield rotation (eqs.4.1 and 4.2) and subsequently applying equation 4.19 to the synthetic dataset. On the left hand side transverse configuration and on the right hand side radial configuration is shown. In panel (b) we see the results after inserting  $\mathbf{P}_S$  and  $\mathbf{P}_C$  into equation 4.19 instead of  $\mathbf{u}_t$  and  $\mathbf{u}_r$ . The part with longer wavelength visible on the radial configuration after vector rotation panel (a), doesn't show up after divergence estimation due to the highpass filter effect of the derivation. Figure 4.5, panel c shows the synthetic data results for comparison with the other methods for the slowness projection method. Please note the excellent agreement between the vector rotation method and the slowness projection method. For completeness the polarization of shot X is plotted in panel (d) underlain by component  $u_x^X$  to be compared with the horizontal slowness vectors (wavefront gradients on panel e).

In contrast to the radial symmetric case of surface fields, the direction of the emerging ray  $\hat{p}$  cannot be estimated and has to be obtained from the data for the refracted wavefield. The exact way to determine  $\hat{p}$  is to measure the polarization direction of the vectors  $\mathbf{u}_t$  and  $\mathbf{u}_r$ , resp.  $\mathbf{P}_S$  and  $\mathbf{P}_C$ . Following from reciprocity (Claerbout, 1976) this is equivalent to recording the wavefield emitted by a pure longitudinally polarized source at the receivers position with receivers pointing in  $X$ - and  $Y$ -direction at the source position, respectively. Analogously this is equivalent to recording the wavefield emitted by a pure transversely polarized source at the receivers position with receivers pointing in  $X$ - and in  $Y$ -direction at the source position. Polarization is usually calculated by solving the eigenvalue problem of the following covarianz matrix:

$$M = \begin{pmatrix} \text{Var}(u^X) & \text{Cov}(u^X, u^Y) \\ \text{Cov}(u^Y, u^X) & \text{Var}(u^Y) \end{pmatrix} \quad (4.20)$$

with

$$\text{Cov}(u^X, u^Y) = \frac{1}{L} \sum_{k=1}^L u_k^X \cdot u_k^Y \quad (4.21)$$

and

$$\text{Var}(u^X) = \text{Cov}(u^X, u^X) \quad (4.22)$$

$k$  denotes the time sample index of the analysis window of length  $L$ . The eigenvectors then give the directions of the first, second and third principle axes of the polarization ellipsoid. The direction of polarization is given by the largest eigenvalue and its corresponding vector. The polarization direction as obtained from seismic data unfortunately has a  $180^\circ$  uncertainty. This leads to unwanted and unresolvable phase "jumps" in the

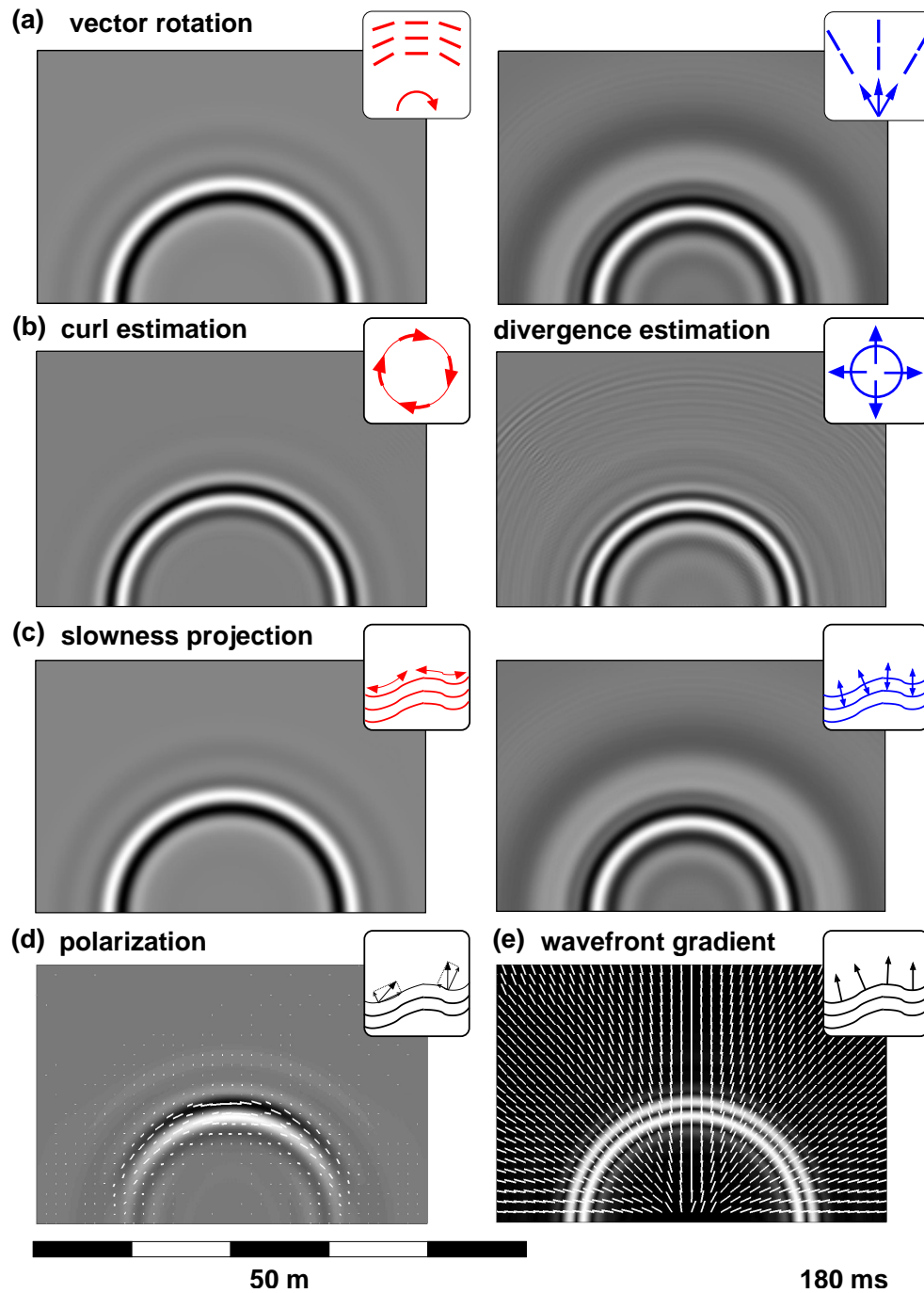


**Figure 4.5:** Synthetic data after applying different wavefield separation approaches (a-c) marked with icons: (a) vector rotation; (b) curl/divergence estimation and (c) horizontal slowness projection. The left column always correspond to the transverse configuration, whereas the right column correspond to the radial configuration. Panel (d) shows the horizontal polarization of a shot in  $x$  direction underlayed by amplitudes of component  $u_x^X$ . For comparison the horizontal slowness vector is shown an panel (e).

obtained wavefields  $\tilde{u}_t$  and  $\tilde{u}_r$  requiring further image processing to unwrap these discontinuities.

Because of this instability of polarization analysis and because trials to estimate take-off angles of rays fail in strongly heterogeneous media, wavefield energy has to be optimized in a different way.

To combine the amplitudes of both shot components in order to enhance the signal to noise ratio of the separated wavefields a heuristic approach is implemented. If we express the seismic trace as the real part of a complex trace::

$$u(t) = \mathcal{E}(t) \cdot \cos(\varphi(t)) \quad (4.23)$$

whereas  $\mathcal{E}(t)$  specifies the envelope and  $\cos(\varphi(t))$  specifies the phase, the above strategy e.g. for optimization of the transverse component can be written as:

$$\tilde{u}_t(t) = \mathcal{E}_t^X(t) \cdot \mathcal{E}_t^Y(t) \cdot \cos(\varphi_t^X(t)) \quad (4.24)$$

The analogue is used to optimize  $\tilde{u}_r(t)$ . The envelope is used to remove phase information from one of the corresponding shot components and is multiplied with the other component in order to retrieve some phase information again. Multiplication was used because it proved to be more stable than summation. So, this procedure removes the energy imprint of the source radiation pattern, thus enhancing the contrast between signal and noise. But it does not remove the phase characteristics of the source.

## 4.4 Refractor Imaging

The ultimate goal of seismic surveying usually is to derive a highly accurate subsurface model. Thus we will now describe a new refractor imaging concept for multi-source 3-D refraction seismic datasets, since existing 2-D methods can not directly be extended to the 3-D case. We have to keep in mind, that for 3-D multicomponent surveys, one of the proceeding wavefield separation concepts and probably optimization by shot rotation has to be applied prior to refractor imaging.

Seismic energy incident on a geological interface showing an elastic impedance contrast will be refracted, i.e. it will travel parallel to and below this interface, if the refracting layer has a higher velocity than the overburden and the angle of incidence is at the critical angle. The principle of refraction seismic surveying is based on the measurement and interpretation of refracted seismic wavefield traveltimes, providing a warped image of the refractor topography, distorted in dependence on the velocities of the traversed media. In order to obtain an topographic map of the refractor we have to correct for velocity influence. For 2-D refraction seismic applications, there is a number of well established mapping method (e.g. plus-minus method and closely related GRM (Hagedoorn, 1959), delay-time method (Gardner, 1939), wavefront reconstructions (Thornburgh, 1930)) based on assuming a two-dimensional velocity structure in the subsurface. As mentioned in the introduction this assumption in many cases is not

correct. The inherent problem at this time is that there is virtual no existing imaging concept for 3-D refraction seismic data. Classical reversed shot methods are not directly transferable to the 3-D case and existing tomographic methods are usually of low and varying resolution.

The imaging concept presented here is implemented in analogy to the exploding reflector imaging concept described by Claerbout (1971, 1985). Claerbout explains seismic imaging or migration by downward continuation of the shot and receiver wavefields until both fields coincide in time and space. An image of a reflector is thus obtained when this imaging condition is satisfied. A concept that is only partly applicable to refraction seismic data, because the incoming wavefield is traveling through the refracting layer before it is emitted again towards the receiver. Thus we have to eliminate the excess traveltimes spent in the refractor from the data prior to migration. This is achieved by applying a velocity reduction thus transforming the seismic refraction section into a pseudo constant-offset section. Figure 4.6 shows the effect on a seismic section: (a) prior to reduction, (b) after reduction, i.e. the constant offset section and (c) the corresponding refractor model. The constant offset still has to be transformed to a zero-offset section by applying further corrections. The method just described is the basis of the imaging concept presented here and will be referred to as "zero-offset transformation". The final and actual imaging step is performed by migration, thus removing false dips, caustics and diffractions from the data.

### Zero-offset transformation

The raypath of the refracted wavefield from the source to the receiver is generally unknown. Thus, we estimate this path by assuming a horizontal two-layer case as shown in figure 4.7. Equation 4.25 sums the traveltimes from the source to the refractor (AB), through the refractor (BC) and back to the surface (CD) to yield an explicit formulation for the total traveltime  $t_t = t(x, z, v_1, v_2)$  depending on geometrical factors and refractor ( $v_2$ ) as well as overburden velocity ( $v_1$ ) (Telford *et al.*, 1991):

$$\begin{aligned}
 t_t &= \frac{AB}{v_1} + \frac{BC}{v_2} + \frac{CD}{v_1} \\
 &= \frac{BC}{v_2} + 2\frac{AB}{v_1} \\
 &= \frac{x - 2z \tan i_c}{v_2} + \frac{2z}{v_1 \cos i_c}
 \end{aligned} \tag{4.25}$$

$x$  denotes the source-receiver offset and  $z$  the refractor depth. The critical angle  $i_c$  is given by  $i_c = \sin^{-1} \frac{v_1}{v_2}$ .

The reduction time  $t_{rp}$  to yield the pseudo constant-offset section eliminating the time traveled in the refractor is given by:

$$t_{rp} = \frac{BC}{v_2}$$

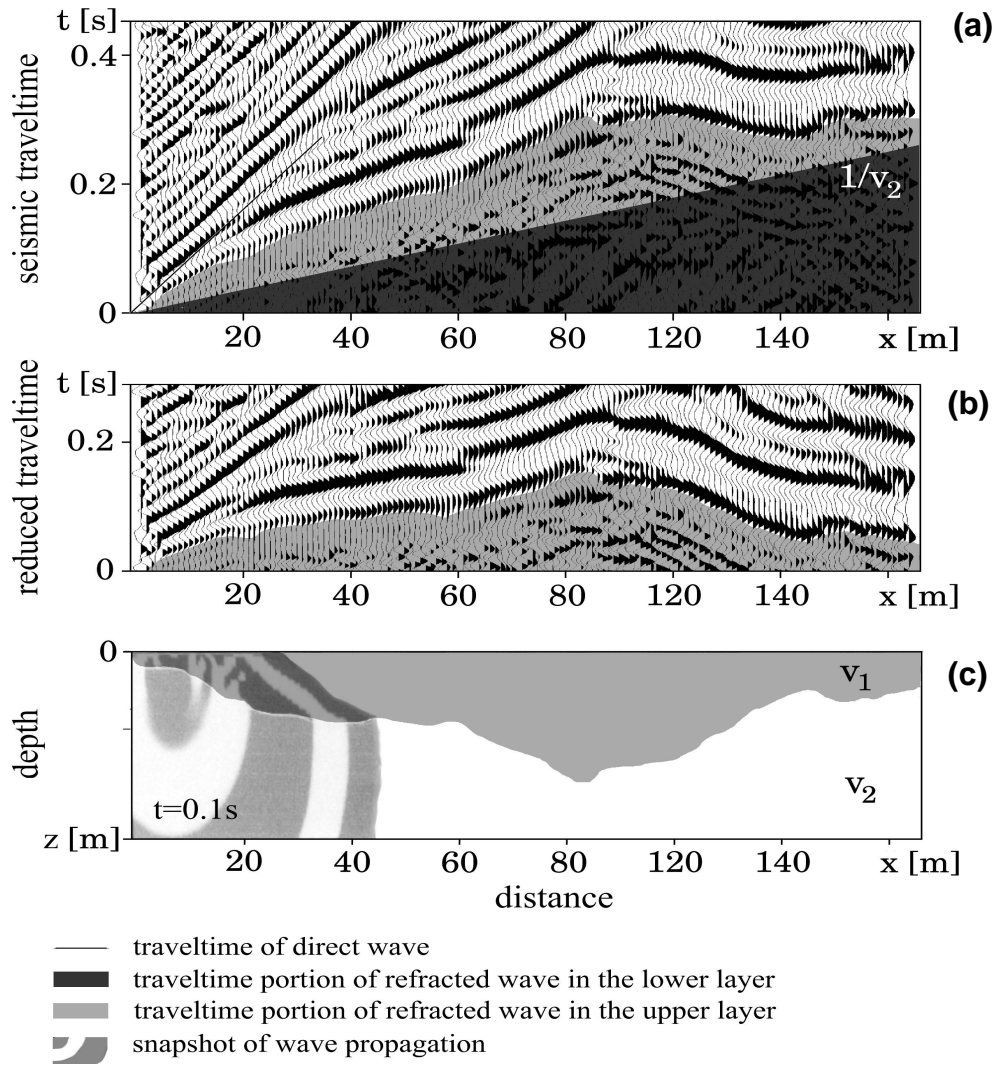


**Figure 4.6:** Principle of refraction seismic with reduction and derived subsurface model: (a) acquired seismic refraction section with the slope of slowness of the upper layer, (b) pseudo constant-offset section obtained by reduction and (c) subsurface model with simulated wavefronts.

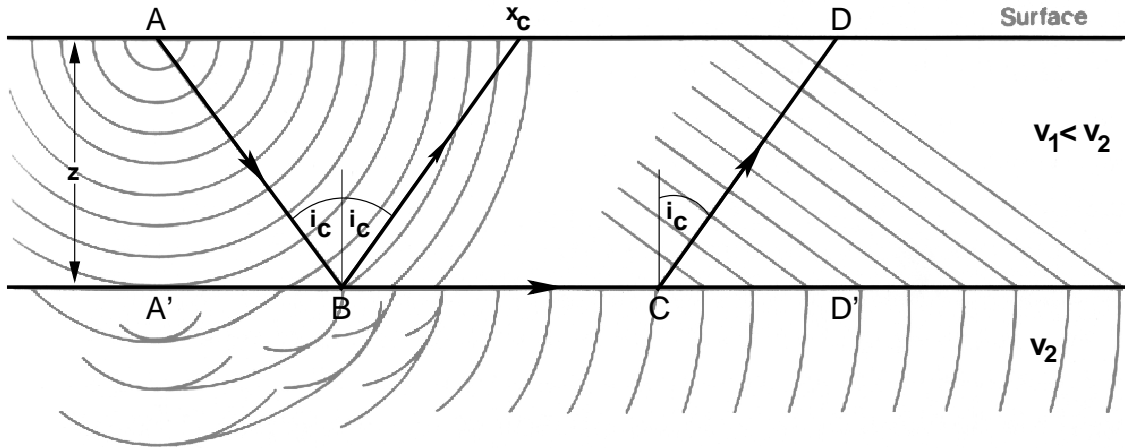


**Figure 4.7:** Raypath for a refracted wave in a horizontally layered two-layer case with  $A$  - source position,  $D$  - receiver position,  $z$  - depth of refractor,  $i_c$  - critical angle and  $BC$  - ray path through the refractor. Gray lines outline the wavefronts.  $x_c$  is the critical offset at which the refractions outruns the direct arriving wavefield.

$$= \frac{x - 2z \tan i_c}{v_2} \quad (4.26)$$

In order to correct for the excess time generated by the remaining offset between source and receiver we have to add  $2dt = 2\frac{AB-z}{v_1}$  to  $t_{rp}$  to yield the zero-offset reduction time:

$$\begin{aligned} t_{rz} &= t_{rp} + 2dt \\ &= \frac{x - 2z \tan i_c}{v_2} + 2 \left( \frac{z}{v_1 \cos i_c} - \frac{z}{v_1} \right) \\ &= \frac{x}{v_2} - \frac{2z \tan i_c}{v_2} + \frac{2z}{v_1} \left( \frac{1}{\cos i_c} - 1 \right) \end{aligned} \quad (4.27)$$

The zero offset section, input to migration, is then obtained after reducing the seismic data  $u(x, t)$  by static correction:

$$u_{red}(x, t') = u(x, t - t_{rz}) \quad (4.28)$$

The second term in equation 4.27 can be regarded as a constant overall shift, if  $v_2$  does not depend on  $x$  and only effects the vertical position of the topographic refractor model but not its shape. The third term in equation 4.27 also contributes an overall static shift but will vanish for small critical angles, that is high velocity contrasts.

### Velocity determination

In order to perform the travelttime reduction described above, we need to determine the refractor velocity  $v_2$ . Conventionally the refractor velocity is calculated from the



reciprocal slope of the refracted event in the seismogram. This velocity is an apparent velocity only true for horizontally bedded layers. For dipping layers data of reverse shots have to be available to calculate the refractor velocity:

$$\frac{1}{v_2} \approx \frac{1}{2} \left( \frac{1}{v_d} + \frac{1}{v_u} \right) \quad (4.29)$$

with  $v_d$  being the velocity of waves traveling downdip and  $v_u$  being the velocity of waves traveling updip.

Problems occur with more complex refractor topographies (e.g. strong curvature or inhomogeneities). In this case the refracted event is not a straight line and has to be calculated piecewise or estimated with linear regression. Without a reverse shot the velocity of a complex refractor remains unknown.

We will now describe a concept to obtain an approximate refractor velocity from 3-D refraction traveltimes data (Musmann, 2003). For each shotpoint  $S_n$  ( $n = 1, \dots, N$ ) the reduced two-dimensional refractor traveltimes field  $t_{S_n}^{red}(x, y, v_2)$  ( $x = i \cdot dx; i = 1, \dots, nx; y = j \cdot dy; j = 1, \dots, ny$ ), should closely resemble the structure of the refractor, if corrected with the true refractor velocity. By iteratively changing the reduction velocity  $v_{red}$  and subsequent comparison of the resulting traveltimes fields, we obtain the best fit refractor velocity when the topographic differences between the individual maps are minimal.

Following equation 4.27 the reduced traveltimes field is given by:

$$t_{S_n}^{red} = t_{S_n} - \frac{x_{S_n}}{v_{red}} \quad (4.30)$$

where  $t_{S_n}$  is the unreduced traveltimes field. The second and third terms of equation 4.27 are ignored leading to constant static shifts which might be different for each shotpoint. Thus, prior to comparing the mean reduced traveltimes  $\bar{t}_{S_n}^{red}$  is subtracted from  $t_{S_n}^{red}$ .

$$t_{S_n}^{red*} = t_{S_n}^{red} - \bar{t}_{S_n}^{red} \quad (4.31)$$

The individual fields are combined to yield a mean total traveltimes field:

$$T^{red} = \frac{1}{N} \sum_{n=1}^N t_{S_n}^{red*} \quad (4.32)$$

The individual reduced traveltimes fields are now compared to the mean traveltimes field  $T^{red}$  by treating them like statistical data and calculating the mean square error  $e_{S_n}^2$ , which we call the "topographic misfit":

$$e_{S_n}^2 = \frac{1}{nx \cdot ny} \sum_{x,y} \left( T^{red}(x, y) - t_{S_n}^{red*}(x, y) \right)^2 \quad (4.33)$$

Finally we average all the errors  $e_{S_n}^2$  to yield:

$$E = \frac{1}{N} \sum_{n=1}^N e_{S_n}^2 \quad (4.34)$$

$E$  indicates the amount of topographic deviation between individual reduced traveltime fields as a function of the reduction velocity  $E = E(v_{red})$ , which we call the "total topographic misfit". By minimizing  $E$  we find  $v_{red}^*$  the optimal reduction velocity which should be in good agreement with the true refractor velocity.

### Model adjustment

The nature of seismic refraction constitutes the fact, that only points beyond the crossover distance, where the refracted energy outruns the direct arrival, carries information about the refractor topography. In order to obtain a model which is accurate at all covered surface positions we have to combine the information acquired from each shotpoint, considering the adversarial influence of the direct arrival which has to be muted, and the reliability of the refraction itself. We thus introduce an offset weighted averaging concept to combine the models from different shotpoints.

The average refractor model  $\tilde{z}(x, y)$  is then given by:

$$\tilde{z}(x, y) = \sum_{n=1}^N \frac{(\hat{x}_{S_n}(x, y))^\gamma \cdot (z_{S_n}(x, y) - \bar{z}_{S_n})}{\sigma} \quad (4.35)$$

where  $\hat{x}_{S_n}(x, y)$  are normalized source-receiver offsets for each shotpoint and  $\gamma$  a tuning factor.  $\sigma$  is the sum of tuned offset weighting factors:

$$\sigma = \sum_{n=1}^N (\hat{x}_{S_n}(x, y))^\gamma \quad (4.36)$$

The average refractor depth  $\bar{z}_{S_n}$  again has to be subtracted before building the model to circumvent the influence of unknown static shifts (term two and three in equation 4.27) and, thus, the model  $\tilde{z}(x, y)$  is undetermined in depth. It can be shifted and tuned to yield a best fit  $\tilde{z}'(x, y)$  if coring information is available:

$$\tilde{z}'(x, y) = \tilde{z}(x, y) - z_0 \quad (4.37)$$

Please refer to section 5.3 for an example application.

# Chapter 5

## Application to Field Data

The two datasets acquired for this investigation and the wavefield separation method as well as the imaging technique described in the preceding chapter 4 shall now be discussed in more detail. Observed wavefield phenomena such as radiation patterns, the dynamics and kinematics of refracted and surface waves are initially scrutinized. Subsequently wavefield separation methods will be applied to both data sets with a focus on improved source characteristic interpretations and further investigations of 3-D effects. Finalizing this chapter the refractor imaging concept will be verified by deriving the topography of the Lions' Harbour basin as covered by the second dataset.

### 5.1 Wavefield Phenomena

In the following we apply vector rotation technique to investigate source characteristics, refracted SH- and Rayleigh-waves. To give an overview, Figure 5.1 shows a sequence of time-slices for data recorded in area  $\mathcal{A}$ . The data is rotated to a transverse geometry (eqs. 4.1 and 4.19) as indicated by the pictogram in the first time-slice at 30 *ms*. Subsequent time-slices are separated by time steps of 30 *ms*. In order to enhance weak arrivals at later recording times and larger offsets, the data was plotted using an AGC of 200 *ms* window length. AGC shadow and amplified noise in the acausal timeslice regions are obvious. In order to correlate distinct kinematic and dynamic features of the wavefield with other geophysical information available for the area, the figure also displays gray-scaled magnetic data and a subsurface model as derived from 2-D refraction seismic (upper left hand corner).

The direct wave is approximately of radial symmetry and coherent (time-slices at 60–180 *ms*), as we would expect in the case of a homogeneous half space. However, its wavefront gets increasingly deformed as it approaches the more shallow zones of the basement.

We observe a weak refracted wave traveling from left to right starting at 210 *ms* right below the upper left corner. It is not connected to the direct wave. At about 300 *ms* it merges with a more obvious refraction, appearing at 270 *ms* in front of the direct wave (see also the broad, white phase in time-slice at 300 *ms*).

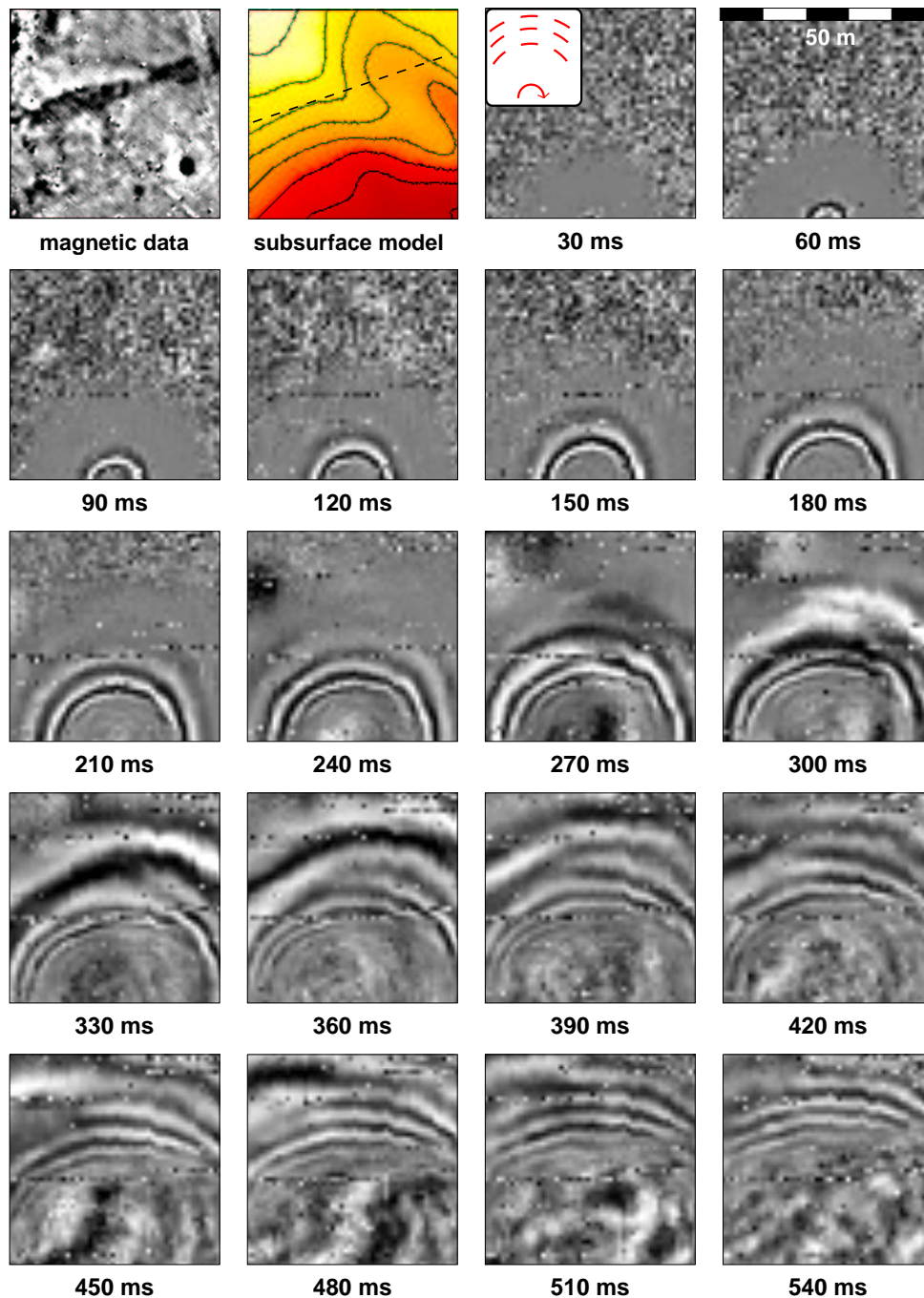


**Figure 5.1:** Timeslice sequence of the so-called transverse geometry of area *A*. Each geophone is rotated transverse to the source point (see also the pictogram on the upper left hand side in the first seismic timeslice at 30 *ms*). Timeslices are shown from 30 *ms* to 540 *ms* in steps of 30 *ms*. In the upper row also shown are magnetic data as gray scaled picture (left) and a subsurface model derived from 2-D refraction seismics with contour lines 2 *m* spaced (aside). In the first timeslices only the direct wave is visible (until 180 *ms*). At 210/240 *ms* the refracted wave appears on the left hand side, at 270 *ms* it outruns the direct wave on the right hand side.

The nature of this refraction will be investigated later in section 5.1.2.

A prominent surface wavefield showing dispersion follows the refraction (time-slices 330–540 *ms*). Like the direct wave it deviates slightly from radial symmetry (540*ms*). This is caused by the decrease in refractor depth towards the upper left hand corner of the area (see subsurface model). This effect is even more pronounced in area  $\mathcal{B}$  and will be discussed in more detail in section 5.1.3.

The SH-reflection from the basin bottom starts at about 240 *ms* and is slightly shifted to the left as a result of the sloping basin.

From 420 to 510 *ms* we can observe a strong surface wave reflection starting in the lower left corner and traveling "backwards", from left to right. Its origin cannot be determined but it suggests that the slope of the basin is possibly stronger than in the smoothed subsurface model derived from 2-D seismic (side reflection).

### 5.1.1 Radiation Patterns

Our three-dimensional four-component seismic measurements provide the possibility to study the radiation pattern of the source. This investigation serves to verify whether or not our man-driven hammer source behaves like a vectorial point source even if its shape is far from being a point. This deviation could be expected to grow with progressive destruction of the soil caused by repeated hammer blows during the experiment (cf. fig. 3.2).

Amplitude fields recorded for four different source-receiver combinations on area  $\mathcal{A}$  are shown in Fig. 5.2, a-d. Source and receiver orientations are symbolized in the icons by arrows and dashed lines, respectively. The amplitude fields represent the interference patterns of at least four, possibly five, different wave types: SH- and SV-type shear waves, Love- and Rayleigh waves plus some weak remnants of the direct P-wave traveling in the narrow land velocity zone above the groundwater table. Because of the Cartesian arrangement of the receivers even waves of different polarity intermix so the individual can hardly be distinguished. The situation improves after receivers have been rotated to radial and transverse orientations (eqs 4.1 and 4.2 applied). The outcome of this operation is shown in Fig. 5.3. Panel (a) and (b) show the wavefield as recorded by transversely and radially oriented geophones, respectively, after excitation in x-direction. The analog for a vector force in y-direction is shown in panel (c) and (d). These displays illustrate the source radiation patterns for the transversely and radially polarized wavefields. Unusual is the fact, that an expected phase reversal in panel (b) is not observed. By applying equations 4.19 a transformation into complete transverse and radial configurations is achieved (see Fig. 5.3 e and f, respectively). After this operation amplitudes appear well equalized along the wavefronts indicating that the hammer source worked reasonably well despite all deviations from an ideal point source. The dashed circle in Fig. 5.3, panel (e) shows the front of direct SH- and Love-waves. The comparison with adjacent timeslices (cf. Fig. 5.1) shows that these fronts move approximately with 90 *m/s*. In the radial configuration timeslice (Fig. 5.3, f) significant energy is found outside the circle which has to be attributed to a direct P-wave traveling with about 220 *m/s* in

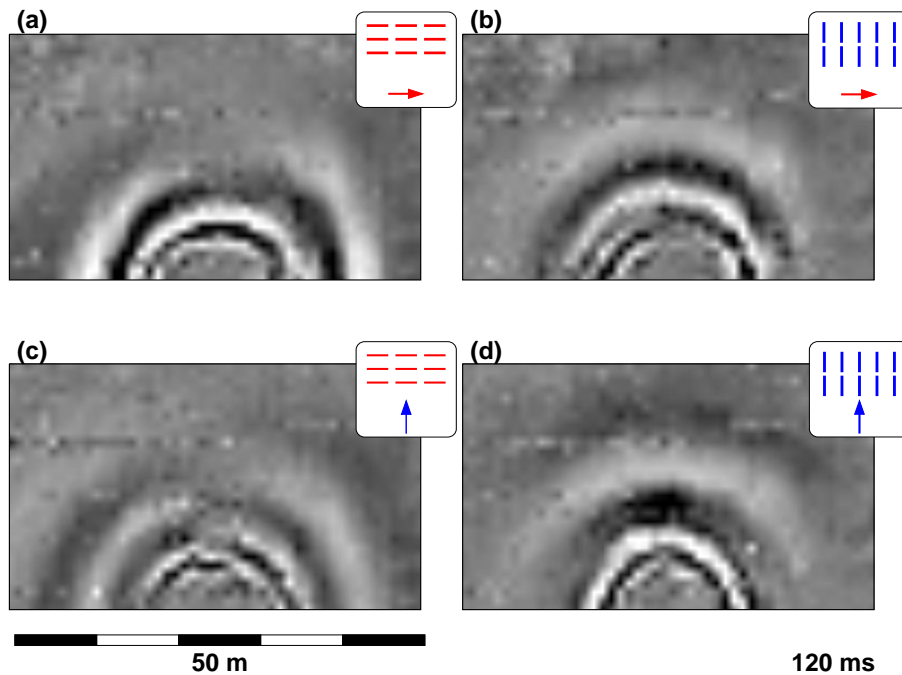


**Figure 5.2:** Four original recorded data from area  $\mathcal{A}$  as timeslices at 120  $m/s$ . a) and b) source in X-direction, c) and d) source in Y-direction; a) and c) receiver in x-direction, b) and d) receiver in y-direction (see pictograms). The line that vertically cuts the timeslice in the middle is equivalent to a "normal SH-spread" for a) and a "normal SV-spread" for d), as well as the line at the lower edge (a) "SV-spread" and d) "SH-spread").

the partially saturated zone above the groundwater table. In addition, the asymmetry inside the dashed circle (Fig. 5.3) shows that the basin fill is heterogeneous. Another example of small scale heterogeneity within a radiation pattern can be detected on area  $\mathcal{B}$ . Figure 5.4 shows rotated data of area  $\mathcal{B}$  at four successive times with 20  $m/s$  separations. Transverse (left) and radial (right) configurations are plotted together in one panel. The shotpoint is located within the grid (diamond in Fig. 5.4 cf fig. 2.8). This example confirms the point source character of the hammer source and show that the wavefront is nearly of perfect radial symmetry (dashed line). Small scale deviations from this symmetry are partly due to geophone gridding, partly larger than grid spacing, an effect we relate to the existence of pronounced mudcracks in this area (Figure 3.3). Note that the P-wave velocity of the Vadose Zone is even lower than in area  $\mathcal{A}$  (140  $m/s$ ).

The velocity of the direct S-wave has not changed from areas  $\mathcal{A}$  to  $\mathcal{B}$  (approx. 90 – 100  $m/s$ ).

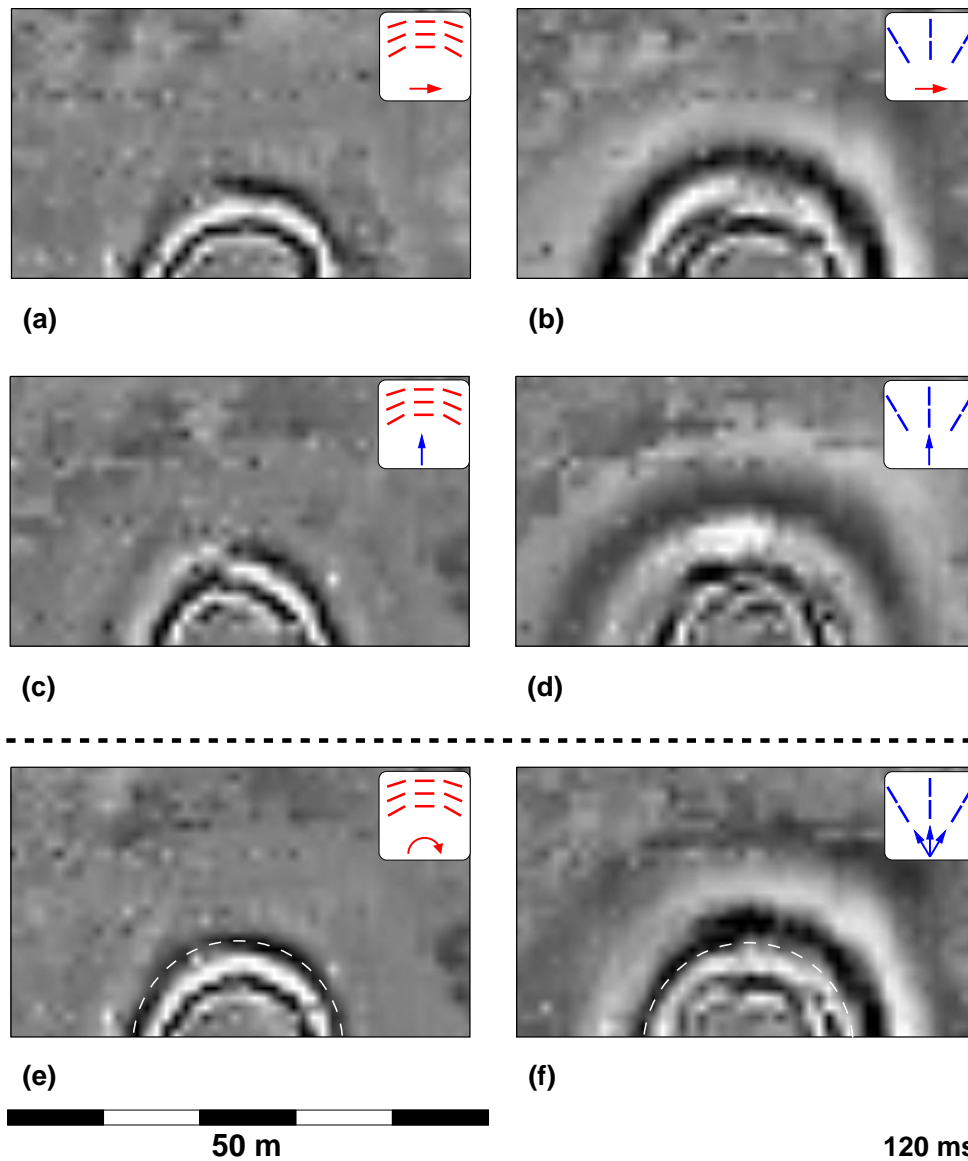


**Figure 5.3:** Six rotated data from area *A* as timeslices at 120 *ms*. The rotation was done by a simple coordinate transformation with a rotary matrix. Panel (a) and (b): wavefield as recorded by transversely and radially oriented geophones, after excitation in *x*-direction. Panel (c) and (d): the same for the *y*-direction source. Panel (e) and (f) display the transverse and radial geometry after rotation the shot components into the estimated ray path direction. The dashed circle indicates the direct SH- and Love-wave fronts (e). In panel (f) significant energy is found outside the circle, attributed to a direct P-wave traveling in the partially saturated zone above the groundwater table.

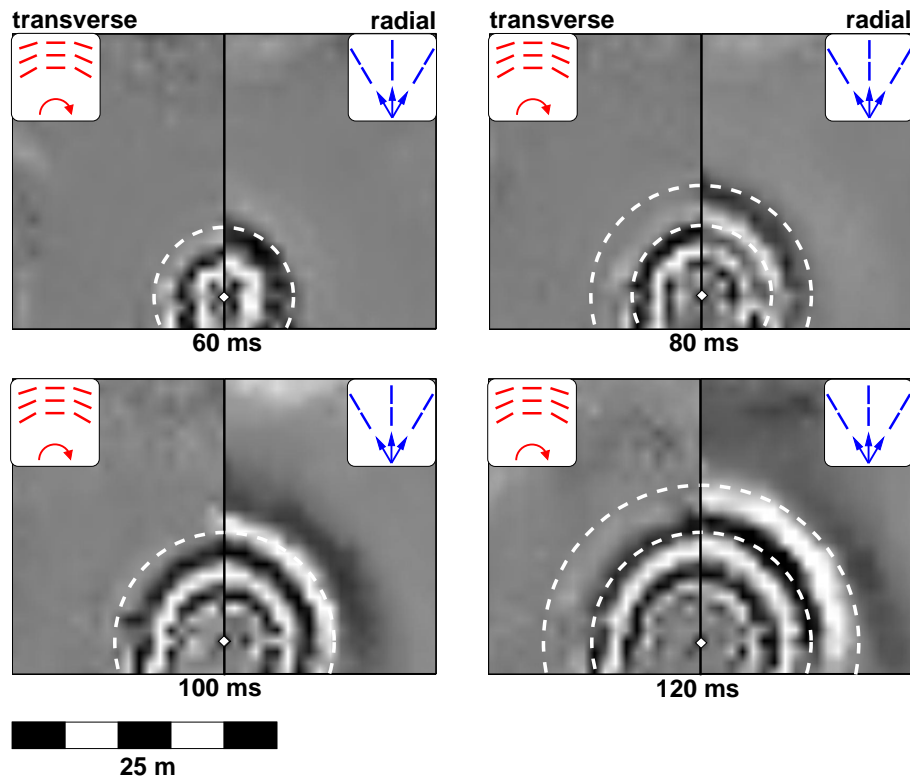


**Figure 5.4:** *Timeslices from dataset  $\mathcal{B}$  at four successive times (60, 80, 100 and 120 ms). In each timeslice the transverse geometry is shown on the left hand side and the radial geometry on the right hand side (see pictograms). Marked with dashed, white semicircles are possible wavefronts after propagation in a homogeneous medium. As one can see, the field data follow mostly this pattern. Minimal differences in velocity of propagation could come from anisotropic media or still mixed wavetypes. The irregular wavefront especially in the transverse case (e.g. time-slice at 100 ms) are caused by mud cracks in the area during acquisition (see also fig. 3.3).*

### 5.1.2 Refracted waves

The curved bedrock topography below area  $\mathcal{A}$  (Fig. 2.8) gives us the opportunity to study corresponding distortions of refracted wavefields. The dashed lines in the timeslices of Fig. 5.5 show the approximate position of the refracted S-wave heading upwards along the slope of the ancient Milesian shore (Fig. 5.5 top right). Such obliquely incident wavefronts are the main error source in 2-D refraction seismic.

In order to investigate this effect, the model derived from a previous survey (please see section 2.3) with parallel 2-D refraction lines (Fig. 5.6, a) and an improved model from the 3-D survey (Fig. 5.6, b) were used to compute FD first break traveltimes. The bedrock topography was inverted by using S-wave velocities known from previous



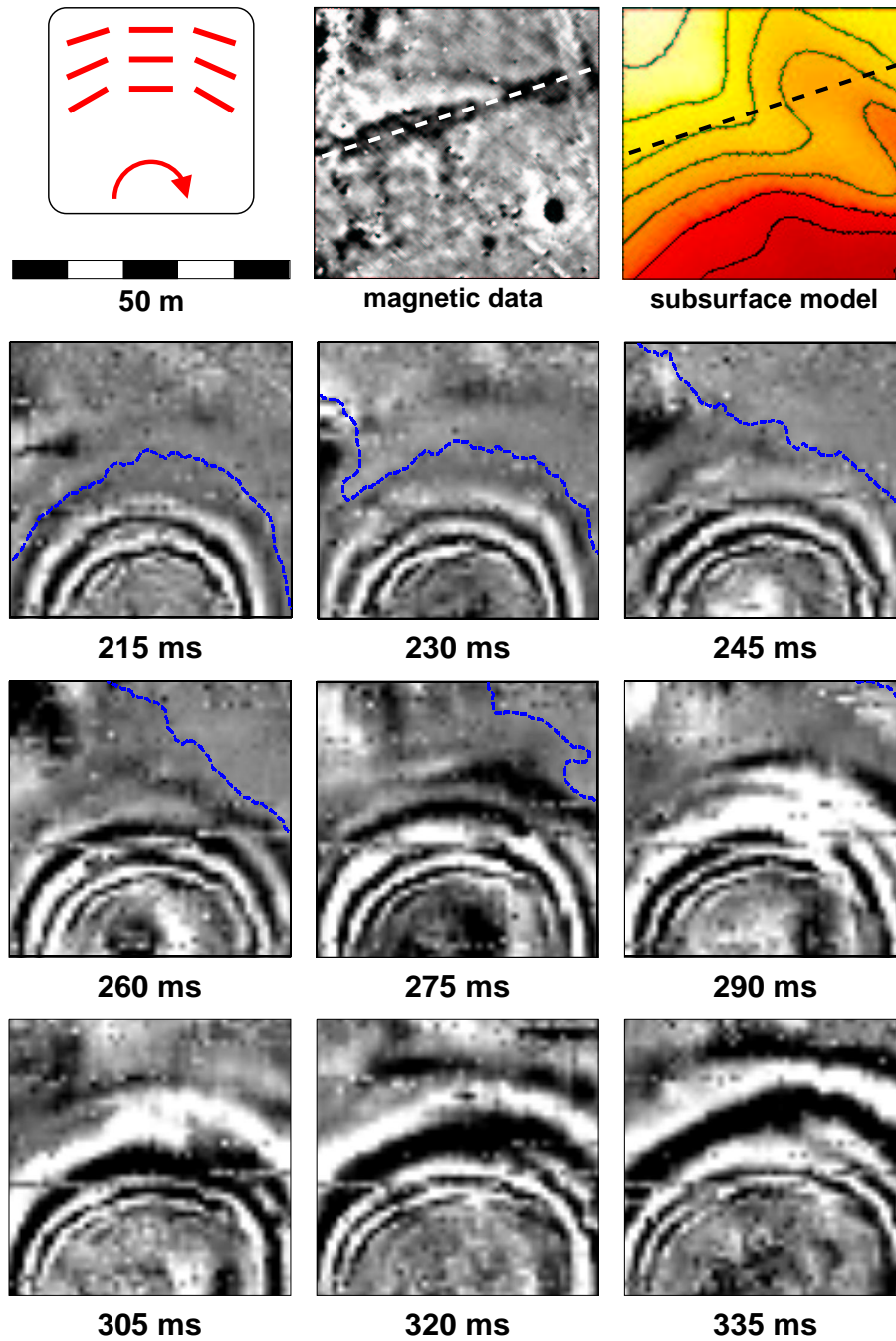


**Figure 5.5:** Timeslice sequence from dataset  $\mathcal{A}$  for refracted wave phenomena from 215 to 335 ms in steps of 15 ms. First appearance of refracted wave is about 215 ms on the upper left hand corner of the area. Later on at about 275 ms the refracted wave shows up in the middle of the right side. It seems that both parts merge into one wavefront at about 320 ms.

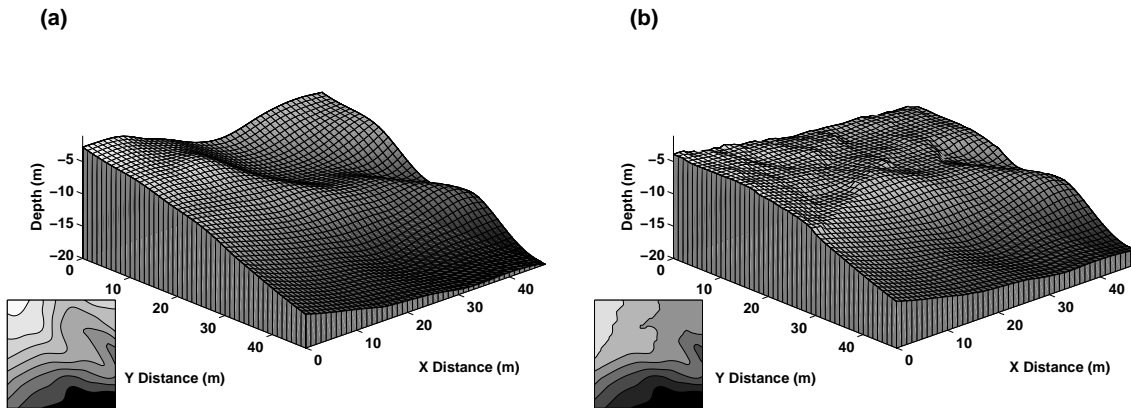


**Figure 5.6:** Subsurface models for area  $\mathcal{A}$  as they were used for FD traveltimes modeling (cf. fig. 5.7). Panel (a) shows the old model derived from parallel 2-D refraction lines and panel (b) shows the improved model from the 3-D survey. Please note, that the deeper part of model (b) is cloned from model (a). The inlays on the lower left corners show contour plots of the models.

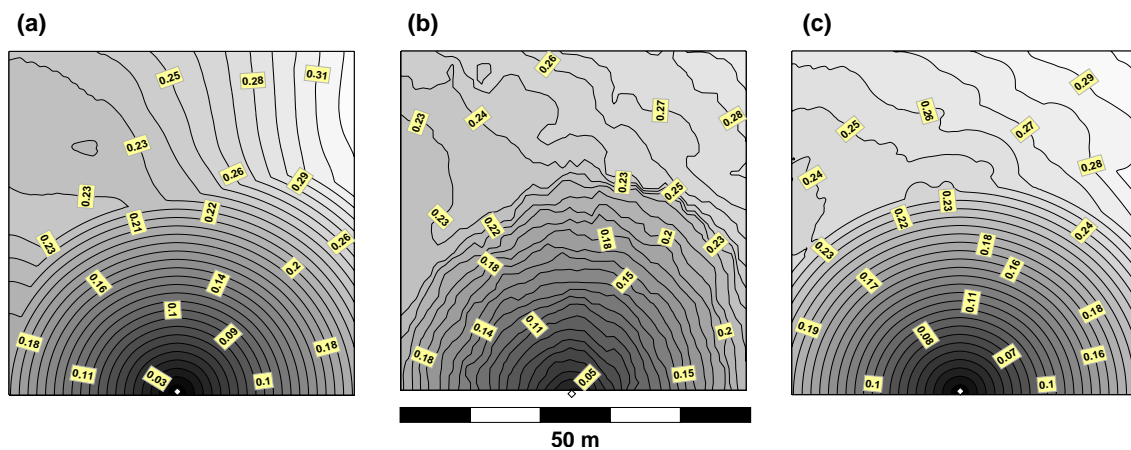


**Figure 5.7:** FD traveltimes modeling results for old and new subsurface models (panel a and c), compared to picked first breaks from dataset  $\mathcal{A}$ , panel (b).

measurements and applying the delay-time method. The deeper part of model (b) is cloned from model (a) because this area is masked by the direct arriving wavefield in the 3-D survey. The new model indicates that the refractor is more flat than initially assumed. Also, due to the dense geophone grid the 3-D survey reveals greater topographic detail with resolution on the meter-scale.

The calculations served to be compared with picked traveltimes, in order to verify the previous 2-D and new 3-D interpretations. From figure 5.7 it becomes obvious, that the 3-D model better fits the picked travel times. For forward modeling an overburden velocity of  $120\text{m/s}$  and a refractor velocity of  $500\text{m/s}$  were assumed.

### 5.1.3 Surface waves

Similarly to area  $\mathcal{A}$ , the previously determined basement contour of area  $\mathcal{B}$  (Fig. 2.8) was confirmed in its basic features by 3-D shear wave refraction measurements leaving a discrepancy between magnetic anomaly and basement contour. A surface wave study based on the 3-D data set of area  $\mathcal{B}$  showed that the magnetic structure is probably too shallow and too thin to be "seen" by refracted S-waves. A sequence of timeslices from area  $\mathcal{B}$  showing propagating Rayleigh waves is compared in Fig. 5.8 with magnetic contours and a geological site sketch.

Soil heterogeneity causes a strong deformation of the originally circular wavefronts (cf. Fig. 5.4 vs. 5.8 and 5.9). More than  $10\text{ m}$  phase advance occurs in the area of excavation debris (lower right corner of Figs. 5.8, 5.9 left hand column). Additional phase advance is observed in the upper center of the figures in an area bounded by the contour of the questionable magnetic anomaly (indicated by a thin white line in Fig. 5.8). Between  $260$  and  $350\text{ ms}$  phases propagate at  $130\text{ m/s}$  within the area bounded by the magnetic anomaly, that is about  $50\%$  faster than outside. Also, the dispersion pattern changes abruptly along the magnetic line (very clearly visible in  $320$  and  $350\text{ ms}$  timeslices in Fig. 5.8).

A spectral decomposition of data volume  $\mathcal{B}$  (Fig. 5.9) shows that the discontinuity of the Rayleigh wavefront is best observed at frequencies between  $16$  and  $32\text{ Hz}$ . At higher and lower frequencies phases tend again to get more circular (Fig. 5.9, right hand column).

Assuming that the apparent wavelength of the spectral components of the Rayleigh wave correspond approximately to their penetration depth, we estimate that the magnetic heterogeneity should be found at about  $3$  to  $6\text{ m}$  depth.

Besides surface wave behavior, the spectral decomposition discovers a ground coupled air wave to be observed at the  $90\text{ ms}$  timeslice between  $126 - 256\text{ Hz}$  (Fig. 5.9, bottom left). Its front corresponds exactly to a circular wave of  $330\text{ m/s}$  velocity followed by an irregular coda of about  $10\text{ m}$  length. The coda could be caused by acoustic energy trapped in the porespace of the mud cracks (cf. Fig. 3.3).

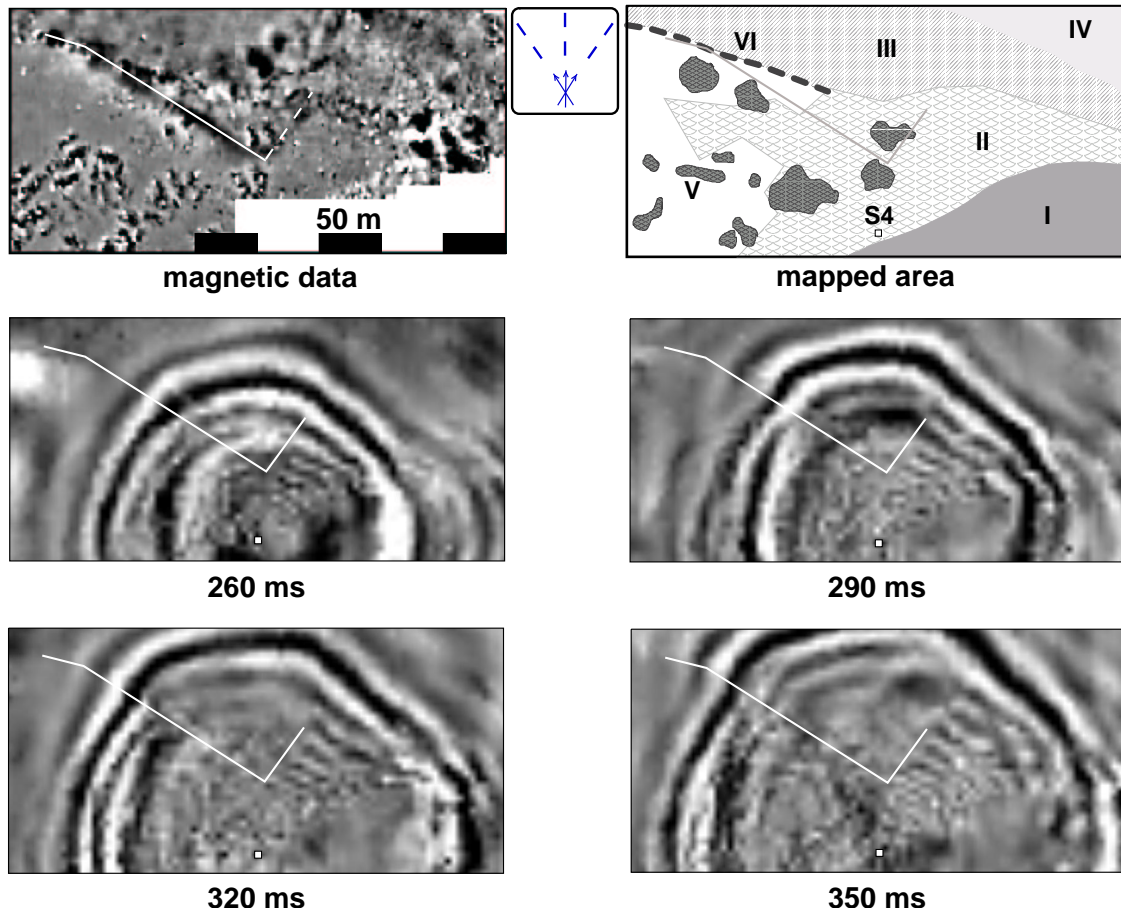


**Figure 5.8:** Timeslices from dataset  $B$  at four successive times (260, 290, 320 and 350 ms) compared to the magnetic map on the upper left hand side and the mapped area on the upper right hand side (I-excavation debris, II-mud cracks, III-tamarisks roots, IV-slight slope, V-small excavation piles, VI- marble remains). Timeslices come from the rotated data in radial geometry. The solid white line marks the position of the magnetic anomaly. The surface waves show clearly a deformation in its wavefront coming from different propagation velocities.

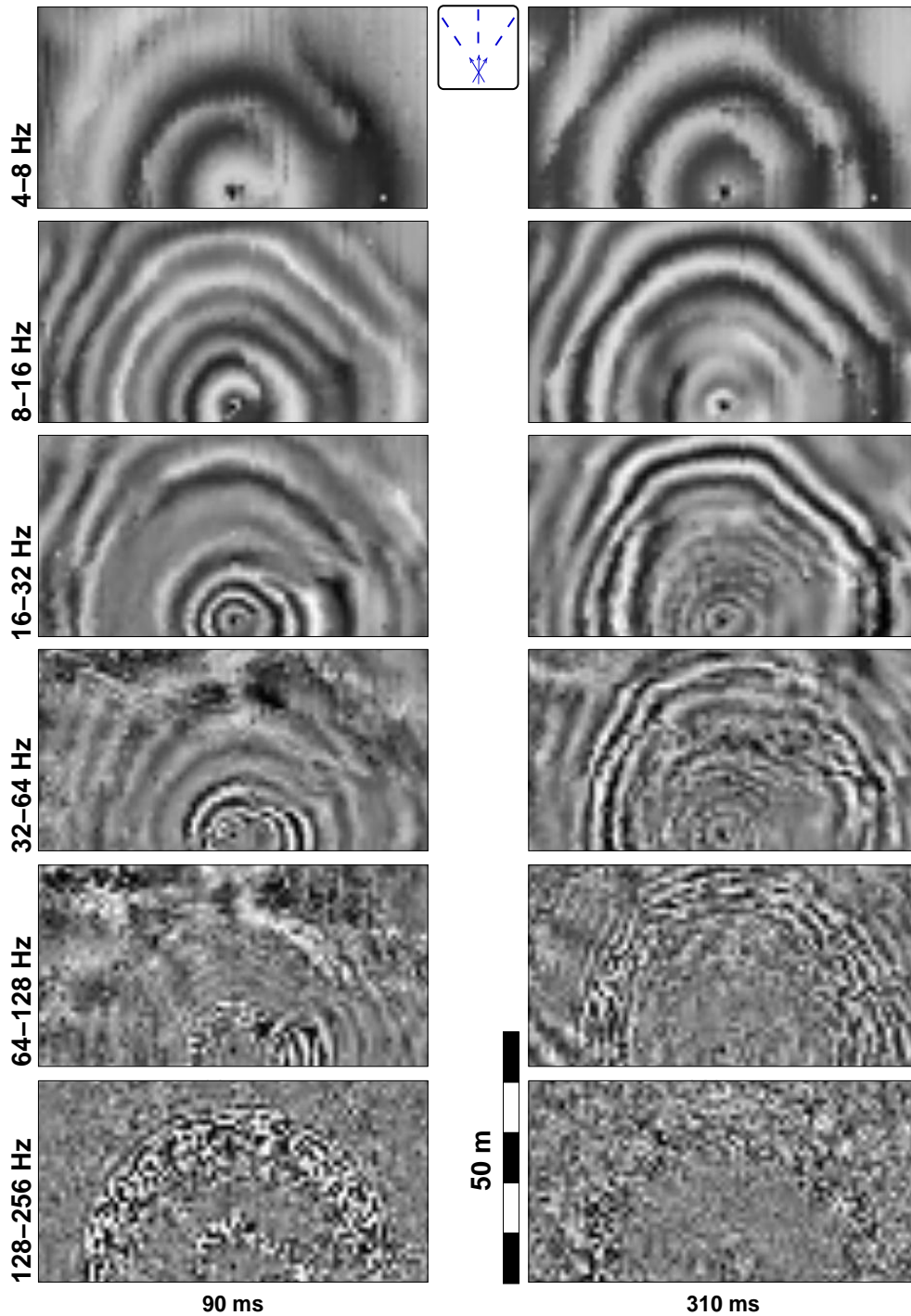


**Figure 5.9:** Timeslices from dataset  $\mathcal{B}$  at two successive times (90 ms left and 310 ms right). Timeslices come from the rotated data in radial geometry and are bandpass filtered in octaves.

## 5.2 Separation of wavefield constituents

The methods discussed in section 4.2 shall now be applied to the field data sets. First, however, we will take a closer look at the data of the first survey (fig. 2.8,  $\mathcal{A}$ ). This dataset is characterized mostly by direct and surface waves, because of the nearby shot point location (1 m aside the area). Reflected or refracted events are rarely observed and partly covered by strong surface waves. Therefore this dataset serves as a good example to study source and receiver characteristics and to proof the methods discussed above to be valid for wavefield separation of direct and surface wavefields. A discussion of wavefield optimization results concludes the section.

### 5.2.1 Source characteristics

Figure 5.2 displays the four single wavefield components that are obtained from survey  $\mathcal{A}$ . The icon in the upper right corner of each panel indicate the source and receiver direction of these components. As illustrated earlier by the synthetic data example we observe also in the field data intermixing of different wave types and azimuthal amplitude variations, due to the source radiation and receiver patterns, as well as acquisition geometry. The amplitude fields represent the interference patterns of at least four, possibly five, different wave types: SH- and SV-type shear waves, Love- and Rayleigh waves plus some weak remnants of the direct P-wave traveling in the narrow land velocity zone above the groundwater table. Because of the Cartesian arrangement of the receivers even waves of different polarity intermix so the individual contributions can hardly be distinguished. This problem shall now be resolved by applying the introduced wavefield separation approaches. Figure 5.10 shows the results of all methods applied to field data for comparison. Wavefield separation was done using the discussed approaches (see section 4.2) and for wavefield optimization the ray path was assumed to be a straight line connecting source and receiver. The outcome of each method is again labeled with the corresponding icon. Panel (a) shows results of the vector rotation method, the transversely rotated case left and the radially rotated case on the right side. We clearly see the wavefield separated into two different wavetypes with different velocities of propagation. Please note, that the velocities of all observed wavetypes are very small, e.g.  $v_s \approx 110$  m/s  $v_p \approx 200$  m/s. The distribution of SH energy is of almost perfect radial symmetry and coherent, whereas the direct P wavefield, which has already traveled further due to its higher velocity, shows a stronger deviation from the symmetry on the right side (as indicated by the arrow). The increase of velocity is also documented by increasing of the apparent wavelength. Obviously the underlying near surface velocity field is not homogenous. These velocity changes could be caused e.g. by changes in porosity and changes in percentage fluid content. However, since we succeeded in decomposing the wavefield, lateral velocity changes seem to be small enough not to significantly violate the underlying assumption of a straight raypath leading from source to receiver. The events with smaller wavelength following the direct P wave, can only be related to the Rayleigh wavefield, traveling with slightly lower velocity than the S wave. This wavefield

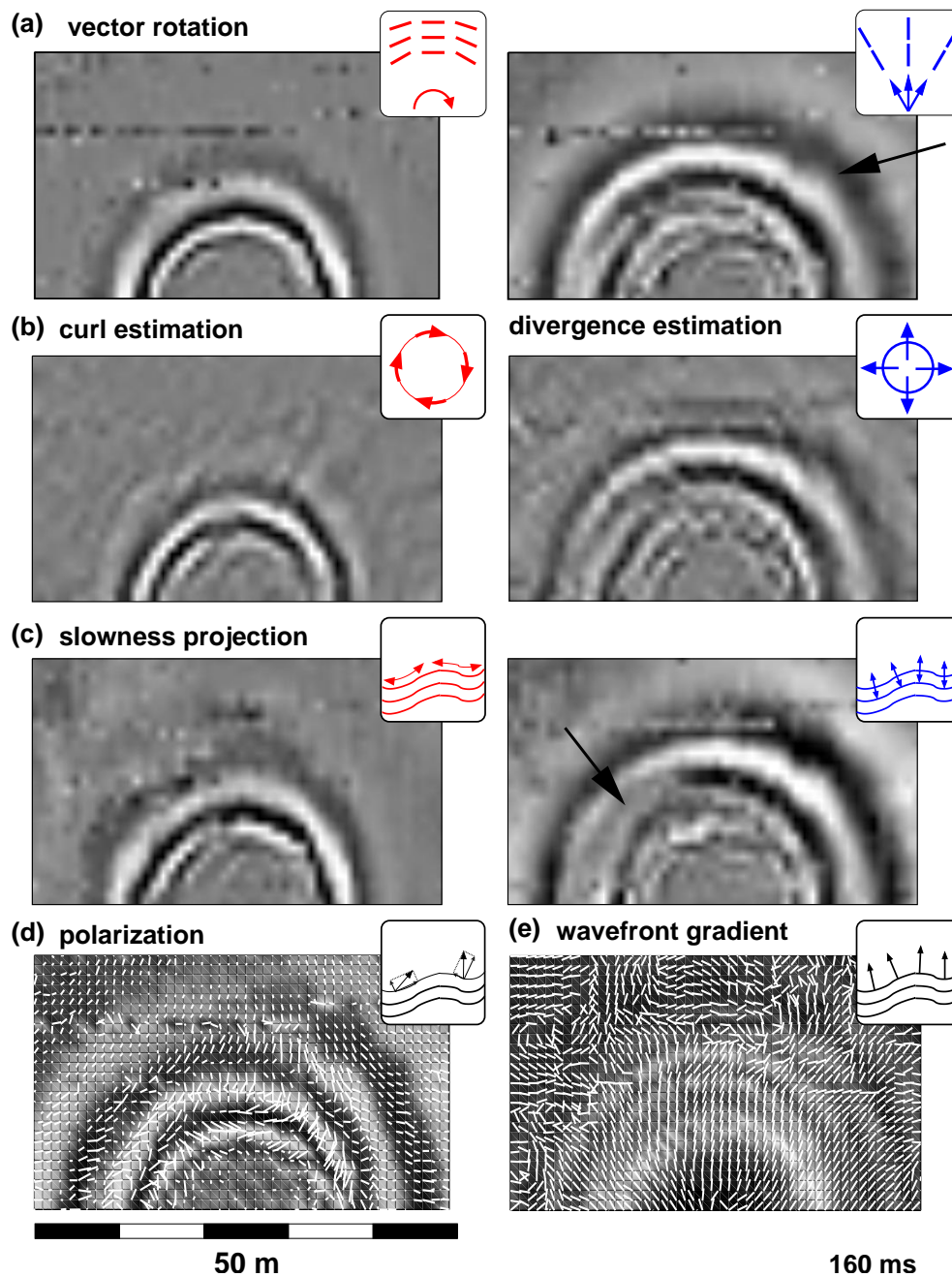


**Figure 5.10:** Time slices of survey *A* after applying the different methods (a-c) marked with icons: (a) vector rotation; (b) curl/divergence estimation and (c) horizontal slowness projection to perform wavefield separation and optimizing by rotation onto a radial emission vector. The left column always correspond to the transverse configuration, whereas the right column correspond to the radial configuration. Panel (d) shows the horizontal polarization of a shot in  $x$  direction underlayed by amplitudes of component  $u_x^X$ . For comparison the horizontal slowness vector is shown an panel (e).

exhibits the characteristics of a coda, indicating the presence of a velocity gradient in the surface layer.

The source frequency content as well as the occurring seismic velocities apart from P wave velocities are comparable to those used in the finite difference simulation. As mentioned before we experienced that a grid spacing of 1 *m* already constitutes the verge of the curl and divergence operators under these circumstances. However, the results of applying curl and divergence operators for wavefield separation to the field data are quite encouraging. Figure 5.10, panel (b) shows the corresponding shearwave energy distribution on the left side and the compressional energy distribution on the right side. The timeslices compare remarkably well with those obtained by vector rotation. We conclude that this method in spite of the difficulties described above should yield acceptable results also when applied to comparable field data sets.

From the discussion based on simulated seismic data, we would expect that under the given circumstances the slowness projection method will perform best. However, comparing panel (c) of fig. 5.10 which displays these results with panel (a) of fig. 5.10, we find that, e.g. for the P wave, wavefield separation was not completely successful (see arrow). This effect can be explained when scrutinizing the local polarization and the slowness vector extracted from the data itself (panel d and e in figure 5.10). Obviously the amplitude and polarization distribution along the wavefront is not coherent enough to fully produce the desired result. These variations can be related to local conditions at the geophones, such as coupling, misalignment or heterogeneity in the surface layer. In addition source force amplitude and direction surely varied not only for each line, but also for each shot.

### 5.2.2 3-D effect

After evaluating the three proposed methods for a rather simple field example we will now move on to take a closer look at survey *B* (see fig. 2.8 in section 2.3) which is certainly more complex. Lets start by taking a look at the individual components as acquired in the field (figure 5.11). We will limit our demonstration to the dataset acquired for shot location *S3* (please compare with figure 2.8, area *B*). All timeslices from this data set shown in the following are rotated counter clockwise by 90 degrees. In contrast to survey *A* the shot location is much further away from the spread (10 *m* separation) and the sensor area is almost twice as long. Also in this case Gal'perin geophones were used, which provide a defined relationship between *x* and *y* receiver components and thus should provide a better polarization quality. The larger source distance allows for the direct wavefield to travel a longer distance than in survey *A*. It has lost its radial symmetry completely after propagating through the heterogeneous near surface layer. It's worth noting, that the acquisition area was characterized by mud cracks and excavation debris (cf. figure 3.3). In addition the area used to be overgrown with tamarisks, which were cut just shortly before the survey, with their large roots still remaining in the ground. Also please note that in the spread the area marked by a dashed line was slightly elevated, provoking the advanced first arrival events observed here. A well developed re-



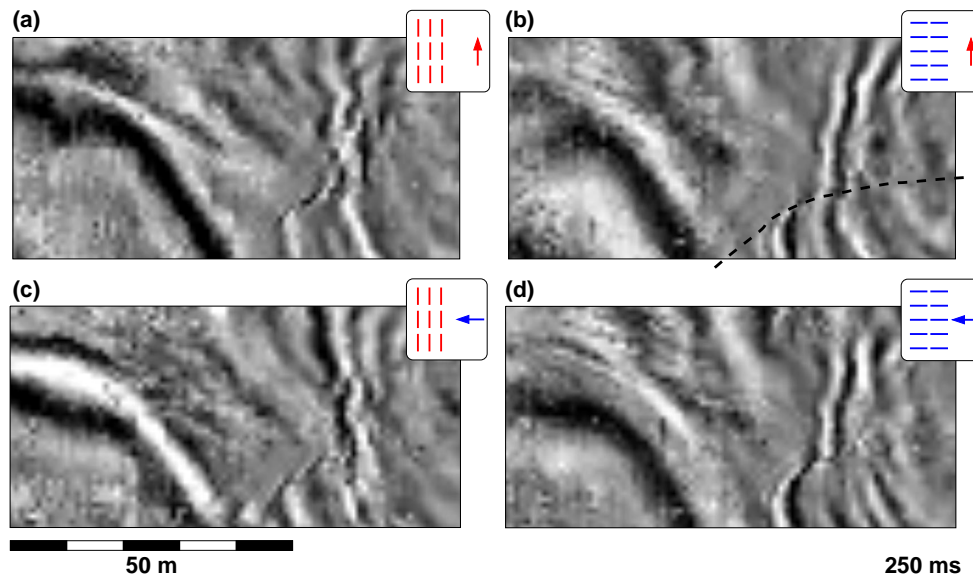


**Figure 5.11:** Time slices of four recorded single components of survey  $B$ , which show a complex pattern of direct and surface waves and strong refracted phases. Icons illustrate source and receiver orientations.

fracted wavefield is visible on all components in the left part of each panel in figure 5.11. Also this refracted wavefield strongly deviates from radial symmetry indicating a strong 3-D topography of the refracting hardrock layer (see figure 2.8 for basin topography). The refraction shows different amplitude characteristics on each panel even when equal geophone components (panel a and c, or b and d) or equal shot components (panel a and b, or c and d) are compared.

In the following the wavefield separation methods are applied to this dataset and results are displayed in figure 5.12 (shot in  $x$ - and  $y$ -direction, respectively) in the same way as in fig. 5.10. Although the vector rotation method is not applicable in this situation it still helps in understanding and verifying the other methods as we will see shortly.

The curl and divergence vector operations and the slowness projection approach are the more appropriate methods to be applied here. However, the direct wavefield has much shorter wavelength than the refracted wavefield. As a consequence we expect the curl and divergence operators to suffer more from the large spatial sampling interval of the spread in case of the direct wavefield. On the other hand, comparing the right sides of panels (a), (b) and (c) suggests that the Rayleigh wave is well extracted not only in panel (c) after slowness projection, but also in panel (b). Again note that the difference in signal shape is due to the fact that we are looking at a representation of seismic power in panel (b) and seismic amplitudes in panel (c). Moreover the curl and divergence operators perform a high pass filter effect enhancing the imprint of the surface wavefield. On the left hand side of panel (a), (b) and (c) we expect to find the SH and Love waves which travel at a slightly larger speed than the Rayleigh wave. The behavior of this

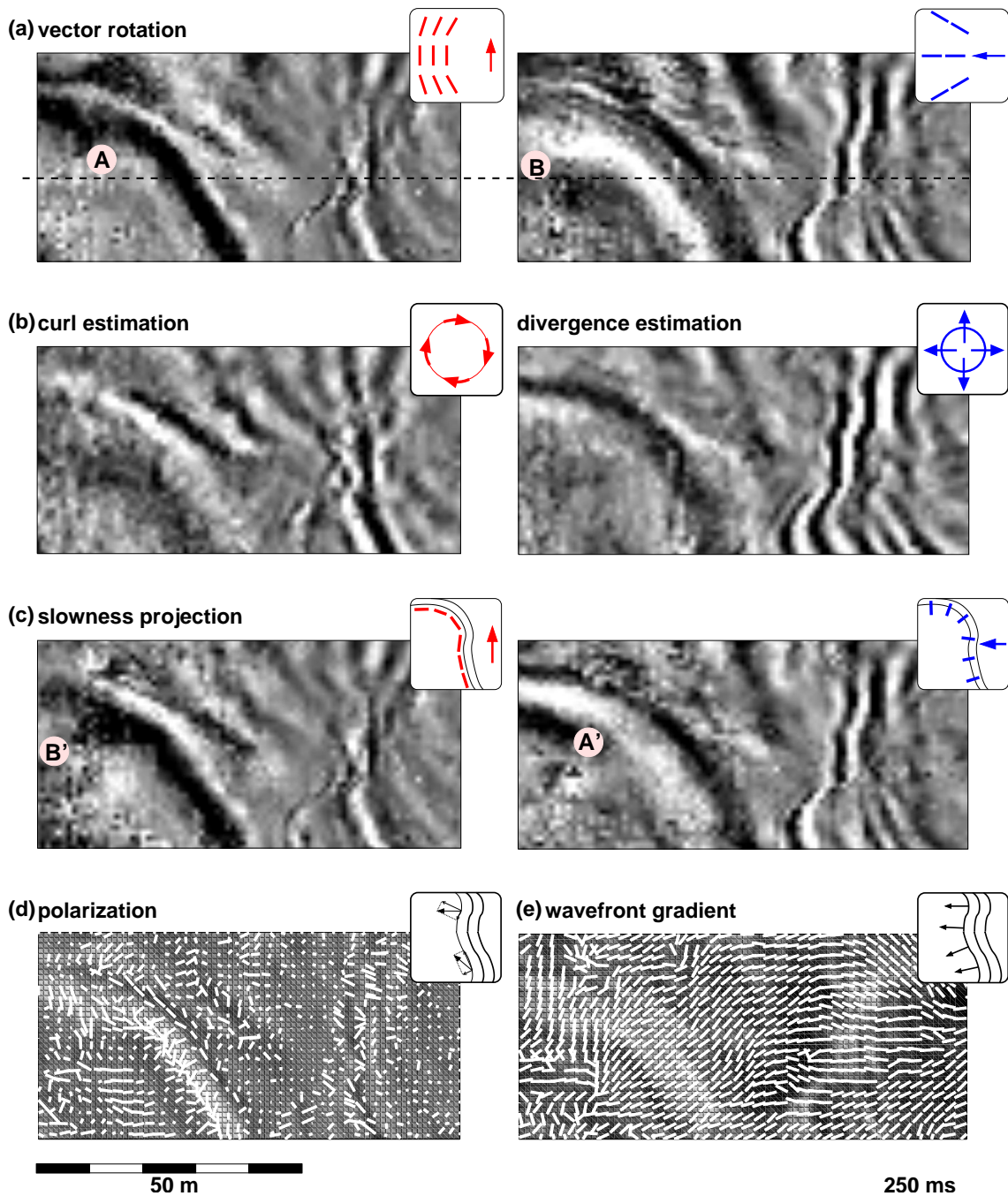


**Figure 5.12:** Time slices of survey  $B$  after applying the different methods. Again the transverse case for shot direction  $X$  is shown on the left side, the radial case for shot direction  $Y$  is shown on the right side: (a) vector rotation; (b) curl/divergence estimation; (c) horizontal slowness projection; (d) horizontal polarization vector and (e) horizontal slowness vector.

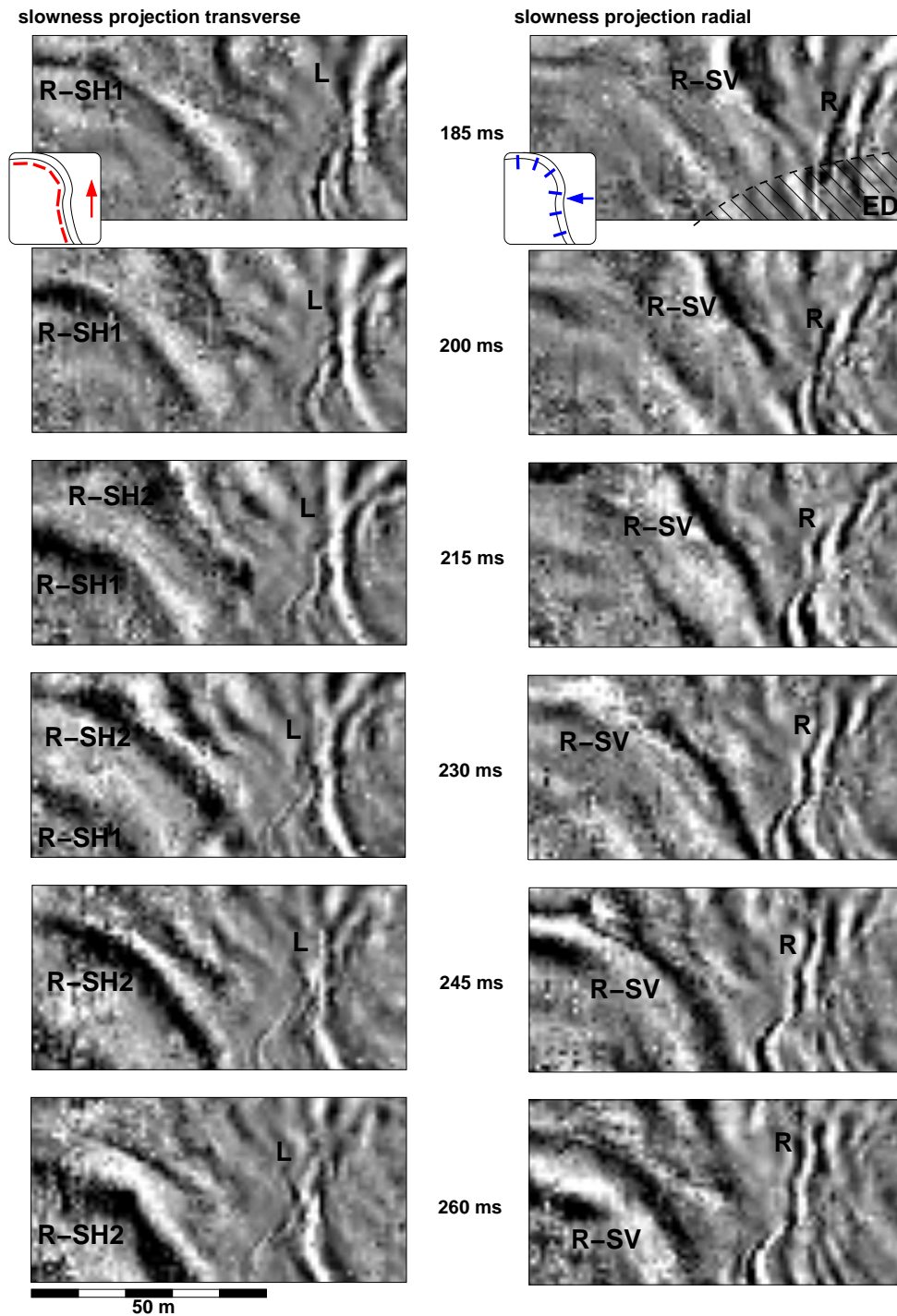


**Figure 5.13:** Time slice sequence in steps of 15 ms (185 to 260 ms) from data set  $\mathcal{B}$  after rotating into the ray coordinate system (horizontal slowness projection). The left side corresponds to amplitudes polarized perpendicular to the ray path and shot direction  $X$ , the right side correspond to amplitudes polarized in ray direction and shot direction  $Y$ .

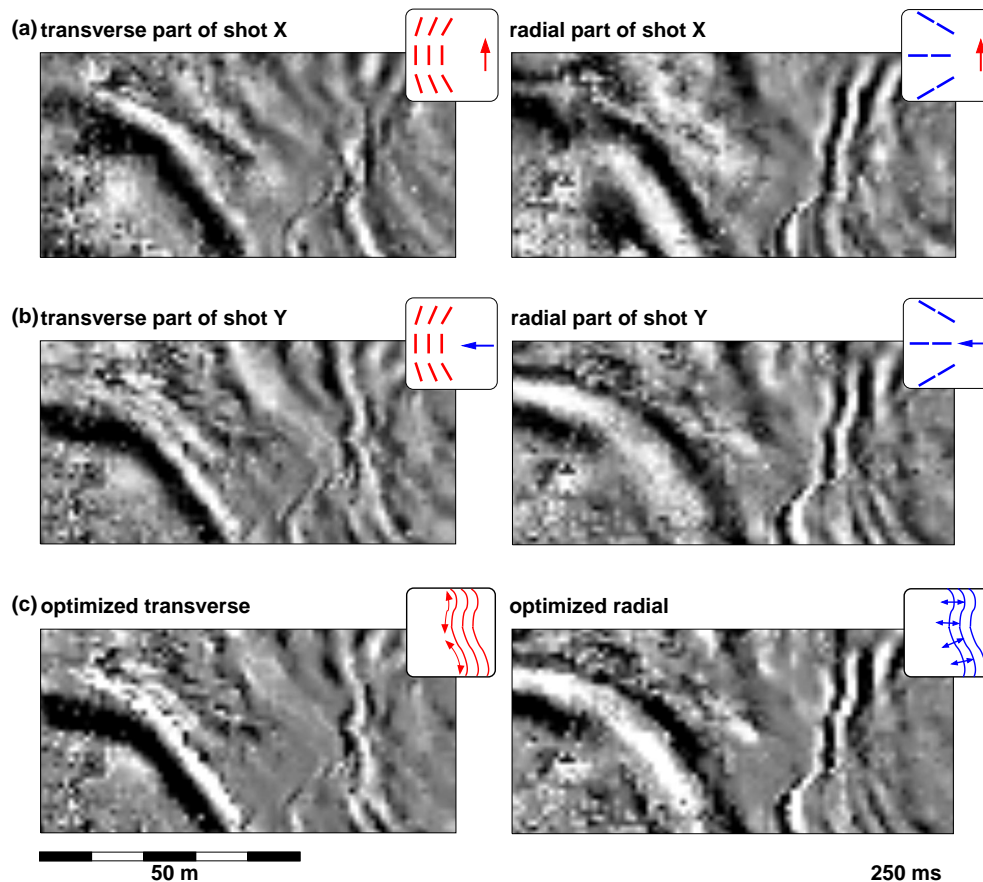


**Figure 5.14:** Time slices of survey *B* after applying the slowness projection method and wavefield optimization. (a) Transverse and radial wavefield constituents for shot direction *X*, left and right, respectively, (b) transverse and radial wavefield constituents for shot direction *Y*, left and right, respectively, and (c) optimized wavefield.

wavefield in relation to the Rayleigh wavefield is difficult to understand from just looking at one timeslice. Therefore we postpone the discussion towards the end of this chapter, where the timeslice sequence is presented (figure 5.13).

As already seen in the raw field data another dominant and interesting feature is the refracted arrival traveling on an arching path. The far offset part of this event is traveling almost perpendicularly to the line connecting source and receivers. Thus vector rotation of the amplitude related to this event leads to enhancement of radially polarized amplitudes (A) in the *transverse configuration* (left side of panel a) and to the enhancement of transversely polarized energy (B) in the *radial configuration* (right side of panel a). This behavior actually causes the vector rotation output to perform with reversed roles. Therefore it is not surprising to find, e.g. the amplitude pattern (A) extracted with the vector rotation *transverse configuration* in the output of the slowness projection *radial configuration* (A') (panel c, right side). The same applies to the corresponding events B

and B' in panel (a), right side and panel (c), left side. The high pass filter effect of the curl and divergence vector operations mentioned earlier, is the reason for the observation that only little energy of these events is extracted and appears only faintly in panel (b). From the previous discussion we conclude that the refracted wavefield was most successfully separated with the slowness projection method and that the events marked by B' and A' can be assigned to the refracted SH wavefield (left side) and SV-wavefield (right side), respectively. One possible reasons for the obvious delay of SV wave A' is anisotropy causing shearwave splitting.

To give a synopsis of the separated wavefields we selected the result obtained from the slowness projection approach to be displayed in a short timeslice sequence of survey  $\mathcal{B}$  (figure 5.13, please refer to the appendix B for further examples). This sequence shall serve to understand the relation between the Rayleigh and SH/Love wavefield and also to illustrate the propagation of the refracted waves. In the left column of figure 5.13 a series of time slices with  $15\text{ ms}$  separation for the *transverse configuration* of the shot in  $X$ -direction, by definition only representing amplitudes polarized perpendicular to the raypath, is displayed. For comparison in the right side column we show the synchronized sequence for the *radial configuration* (i.e. amplitudes polarized in ray direction) for the shot in  $Y$ -direction. In total five major wavefield phases can be observed. We see a surface wavefield separated into its Love ( $L$ ) and Rayleigh ( $R$ ) constituents, as well as different phases of the refracted wavefield, labeled by  $R\text{-SH1}$ ,  $R\text{-SH2}$  and  $R\text{-SV}$ . The high dynamic and kinematic complexity of all wavefield phases becomes now apparent to the observers eye. For example, the Rayleigh wave does not simply follow the Love wave, as it would be the case for a constant gradient surface layer, but partly seems to advance. This effect might be due to the fact that the Love wave is decelerated when traveling in the excavation debris area (shaded area  $ED$  on the right side of the uppermost panel). Another interesting phenomenon is the existence of at least two refracted SH phases ( $R\text{-SH1}$ ,  $R\text{-SH2}$ ), which show almost the same kinematic behavior, i.e.  $R\text{-SH2}$  is following  $R\text{-SH1}$ . In the radial-configuration part of the figure, we see a corresponding  $R\text{-SV}$  phase, which, however, does not show an echoing second phase. The multi-phase refracted SH wavefield might be due to a multiply refracted primary wavefield reverberating between the surface and the refractor.

Wavefield optimization as discussed in section 4.3 shall now be exemplarily performed on transverse and radial constituents derived from separation with slowness projection (figure 5.14). Panel (a) shows wavefields separated into transverse and radial constituents of shot direction  $X$ , left and right, resp., and panel (b) shows separated wavefields of shot direction  $Y$ . In panel (c) the optimized wavefields for the transverse case (left) and the radial case (right) is shown. Clearly seen in both wavefields is the preserved phase characteristics, of shot direction  $Y$  (panel b). The wavefield is enhanced in signal and noise contrast and thus, well prepared for identifying and picking first arrivals.

### 5.2.3 Discussion

The pros and cons of the different wave field separation methods shall now be discussed. The straight forward but simple vector rotation approach is not reasonable for refracted events in 3-D media, because of raypaths deviate from shot point centered radial symmetry. However, for direct and surface waves in homogenous, horizontally layered or gradient media this approach serves as a simple tool to test and evaluate source emission patterns.

Estimating curl and divergence of the wavefield at the surface serves to separate wavefields independently of specific ray directions. Thus, the method is in principle applicable to surface and refracted, as well as reflected wavefields. The approach is sensitive to grid spacing and might require high spacial sampling to perform satisfactorily.

Best performance for refracted waves as it is of primary interest in this investigation was provided by the so named "slowness projection", i.e. rotation into the ray coordinate system. This approach is data driven as is the previous, but is less sensitive to grid sampling effects.

An optimization by rotating separated wavefield constituents into the emerging ray coordinate system could not be performed due to instabilities of polarization analysis. Wavefield optimization using the envelopes yielded good results in improving signal to noise ratio, but does not remove the shots phase characteristic. Slowness projection is thus used in the following to prepare the data as input for refractor imaging.

## 5.3 Refractor Imaging

To derive the refractor topography the imaging technique described in section 4.4 will be applied to field dataset  $\mathcal{B}$ , covering the south-eastern area of the Lions' Harbour. This technique leads from area-wide picked traveltimes, over the calculation of an average refractor velocity and migration of reduced data to subsurface models for each shotpoint. The models are merged to yield one final refractor topography interpretation and adjusted in depth by coring information. This section closes with a discussion including result from tomographic travelttime inversion.

### 5.3.1 Topography of Lions' Harbour (east)

As a first step in applying the imaging method, the refracted wavefield has to be identified and picked in the individual seismic sections. Figure 5.15 shows four different seismograms corresponding to each shotpoint as acquired along the geophone line indicated in the acquisition geometry sketch (see figure center). These seismograms result from applying the wavefield separation technique described in section 4.2.3 to the field data and comprise seismic energy which is polarized in direction of wavefield propagation, i.e. SV and Rayleigh waves. We choose to identify and pick the directly arriving Rayleigh and the refracted SV wave at their most prominent phase as indicated by arrows in the figure. This decision is motivated by possible identification difficulties caused by multiply

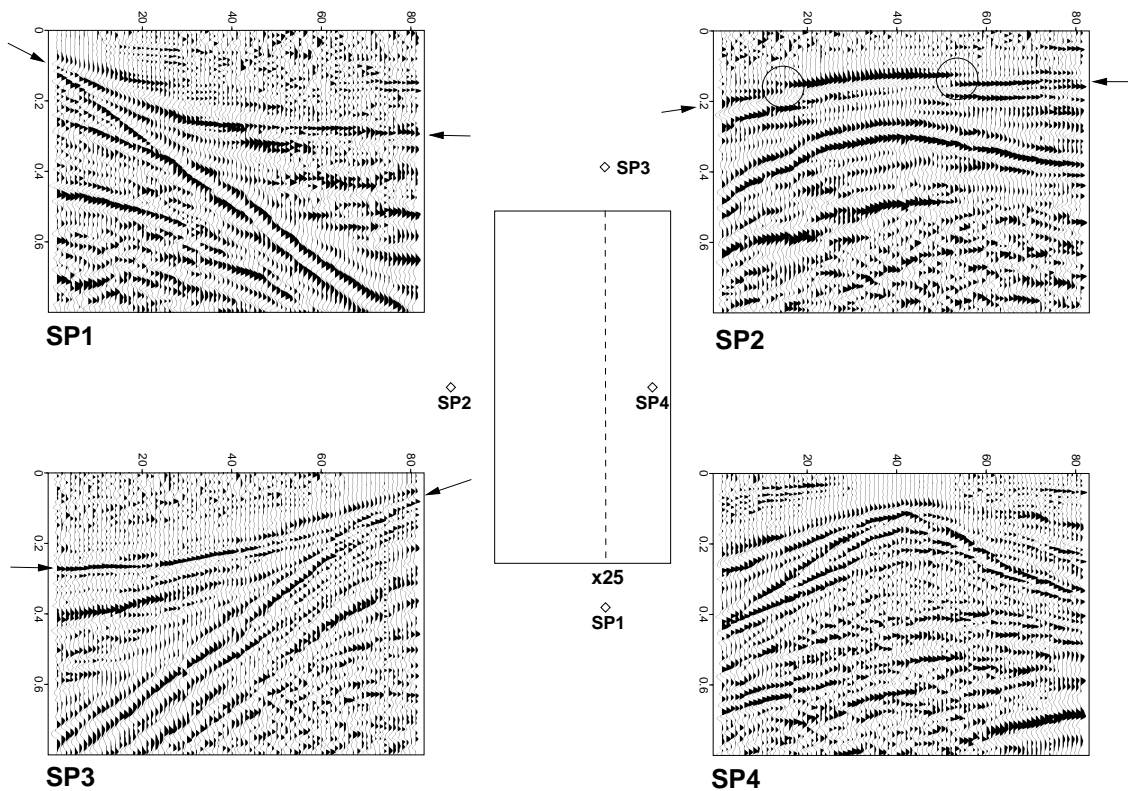


**Figure 5.15:** Example seismic sections from the 3-D survey corresponding to shotpoints one through four (SP1-SP4) obtained after applying wavefield separation by slowness projection (Wölz & Rabbel, 2003). Data were recorded along the profile as indicated by the dashed line in the geometry sketch. Arrows indicate the picked first arrival phase. Circles indicate phase shifts hampering travelt ime interpretation.

observed SH events, as seen in figure 5.13. The data are of an overall good quality, but still in particular situations it is difficult to identify the phase to be picked, as indicated by the circles in the upper right hand panel leading to possible misinterpretation. The first arrival seems to either change phase or exhibits a step in travelt ime. One possible explanation is a rapid change in refractor topography. However, this characteristic is not observed on any of the other shotpoints datasets.

Shotpoint four was not included in the following analysis, because of its position lying within the seismic spread and thus showing mainly direct and surface waves on the recordings. It was used to determine an estimate for the overburden velocity  $v_1$  ( $\approx 120$  m/s). As mentioned earlier the true kinematic nature of the refraction only becomes obvious in the time slice sequence.

Figure 5.16 displays such a sequence with a 10 ms timestep for shotpoint three (SP3). The position of the shotpoint is indicated in the first panel (upper left hand corner). Also indicated is an area of excavation debris (ED), which is elevated above the rest of

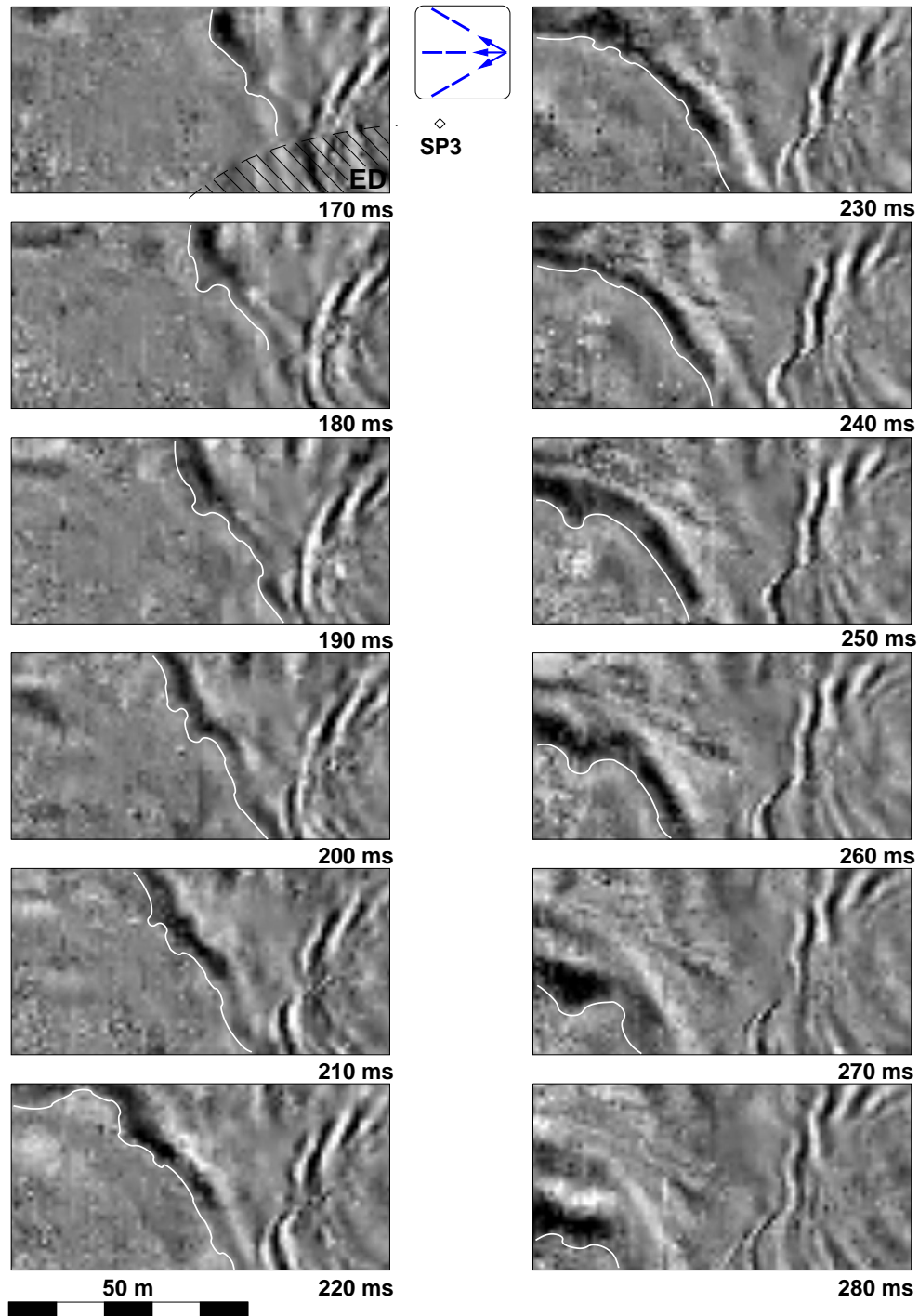


**Figure 5.16:** Timeslice sequence acquired at shotpoint SP3 with refracted wave energy outlined by the white line. The shaded area marked ED indicates excavation debris at the surface. Further description in text.



the survey area and sloping up to a total of about 1 m height. It virtually accelerates the direct wavefield over the refracted wavefield. On the right side of each panel the direct and surface waves are breaking radial symmetry, thus indicating a highly variable surface velocity. The refracted phase is outlined by the white line demonstrating the obvious influence of refractor topography on its propagation direction.

Following the imaging concept introduced previously, the velocity of the refractor was estimated by using an error minimization method. Figure 5.17 shows the topographic

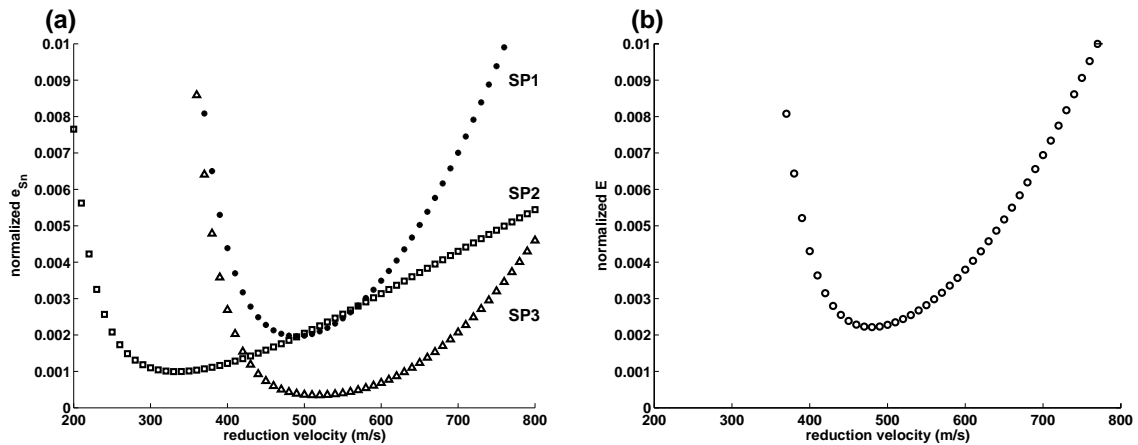


**Figure 5.17:** Topographic misfit (a) for shots SP1-SP3 and total topographic misfit (b) as a function of the reduction velocity. The minimum gives the optimum refractor velocity used for reduction.

misfits as a function of reduction velocity of the three shotpoints used here (panel (a) individual misfits  $f_{S_n}^2$ , panel (b) total misfit  $f$ ). While shotpoints SP1 and SP3 show an optimum refractor velocity estimate of about  $v_{red}^* \approx 500$  m/s and are in good agreement, shotpoint SP1 yields a smaller velocity of about  $v_{red}^* \approx 320$  m/s. The total misfit yields a velocity of  $v_{red}^* \approx 480$  m/s and is used for further analysis.

Subsequently the 3-D seismic data are reduced using equation 4.28, however, the second and third terms of equation 4.27 are ignored. The possible static shifts will be accounted for later by using available coring information.

Figure 5.18 displays the migrated seismic section arranged in the same way as in figure 5.15. A simple constant velocity 2-D Stolt migration algorithm (Stolt, 1978) was used, successively applied to inline and then to crossline sections. Directly arriving and refracted seismic events are more coherent than in the original seismic sections and therefore picking is eased. It was possible to identify the same phases as used for refractor velocity estimation (see arrows). Regions of discontinues events pose the same difficulty as above (indicated by circles). The seismic sections are overprinted by strong isochrone noise at later arrival times, which is not surprising, because the applied traveltimes reduction is tailored to image the refracted energy. Shotpoint SP4 cannot be used for further processing for the same reasons as mentioned above. The individual traveltimes fields resulting from picking the first arrivals on the migrated sections each representing the

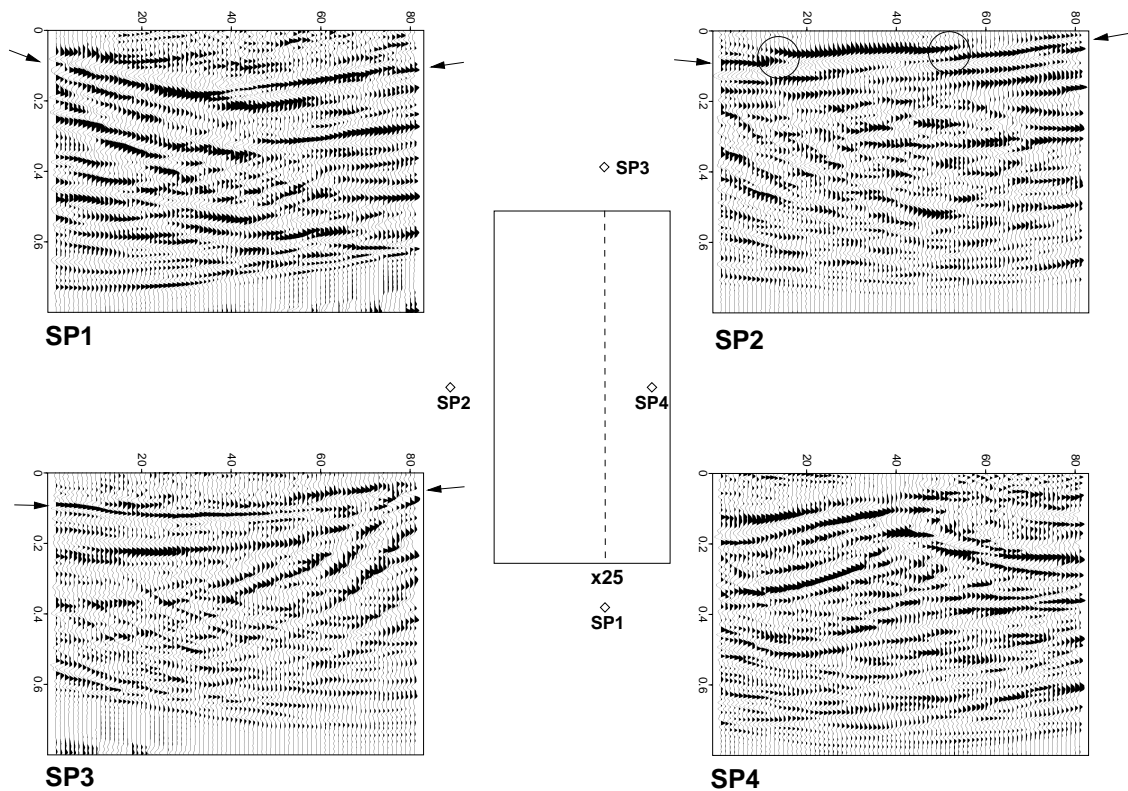


**Figure 5.18:** *Seismic sections after reduction and Stolt migration. Please compare with figure 5.15. Arrows again indicate the picked first arrival phase. Circles indicate phase shifts hampering travelt ime interpretation.*

refractor topography, are now converted to topographic models  $z_{S_n}(x, y)$ , by multiplying with the overburden velocity  $v_1$  (figure 5.19). Please note, that each model is distorted in the vicinity of the corresponding shotpoint by the imprint of the direct arrival. This imprint either locally "decreases" the refractor depth, as seen in panel (a) or generates distortions of the topography due to misinterpretation of interfering direct and refracted wavefields (panel (c), arrows, also compare with figure 5.16 at 180  $m/s$ ). The obvious protrusion observed in panel (b) (arrow), is not observed in the other models. This might be explained by the fact, that refracted rays emanating from other shot points do not travel in the same regions of the refractor and thus, are simply not sensitive to this topographic feature.

The nature of seismic refraction constitutes the fact, that only points beyond the crossover distance, where the refracted energy outruns the direct arrival, carries information about the refractor topography. In practice often only refracted arrival beyond the crossover distance can be clearly identified. In order to obtain a model which is accurate at all covered surface positions we have to combine the information acquired from each

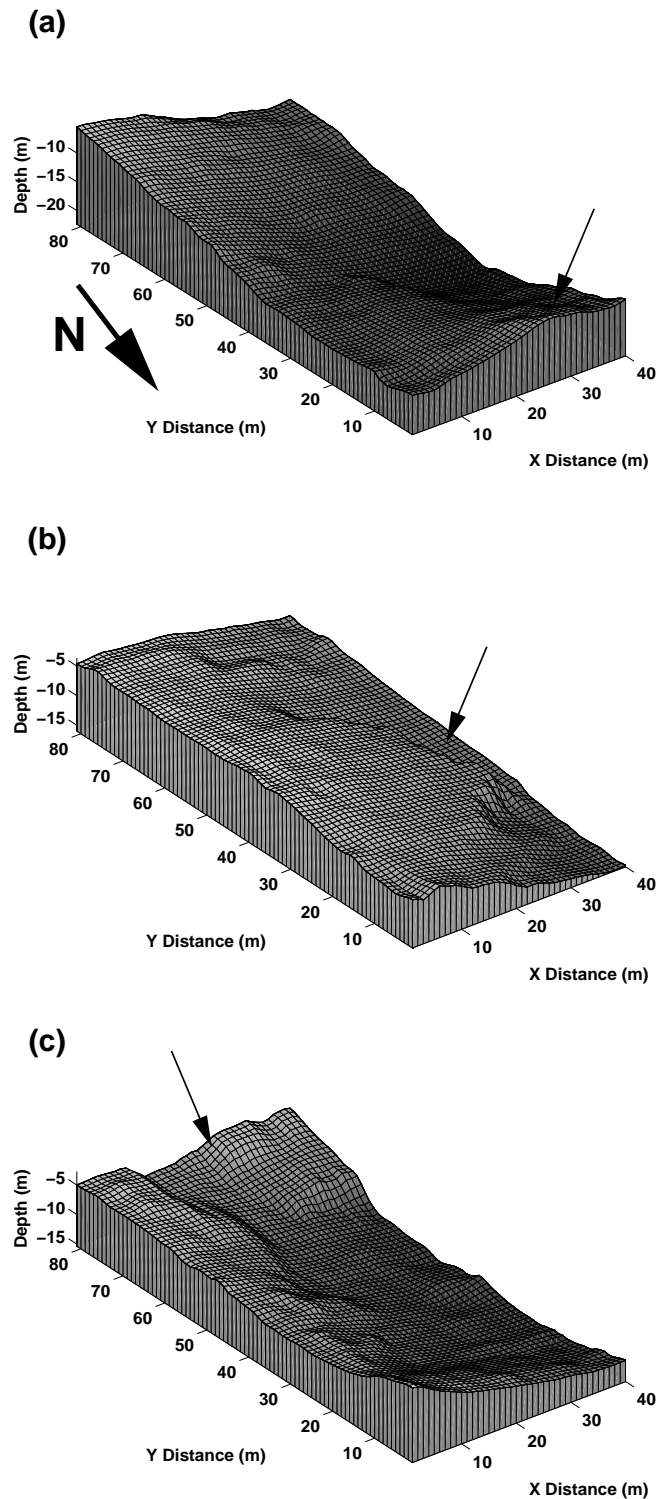


**Figure 5.19:** Individual topographic models resulting from picking the first arrival on the migrated sections of shotpoints S1-S3, converted to depth by multiplication with the overburden velocity  $v_1$ . Arrows indicate regions of direct arrival distortions. While models of S1 and S3 show similarities, the model of shotpoint S2 shows different depth and shape. A possible reason might be due to picking errors.

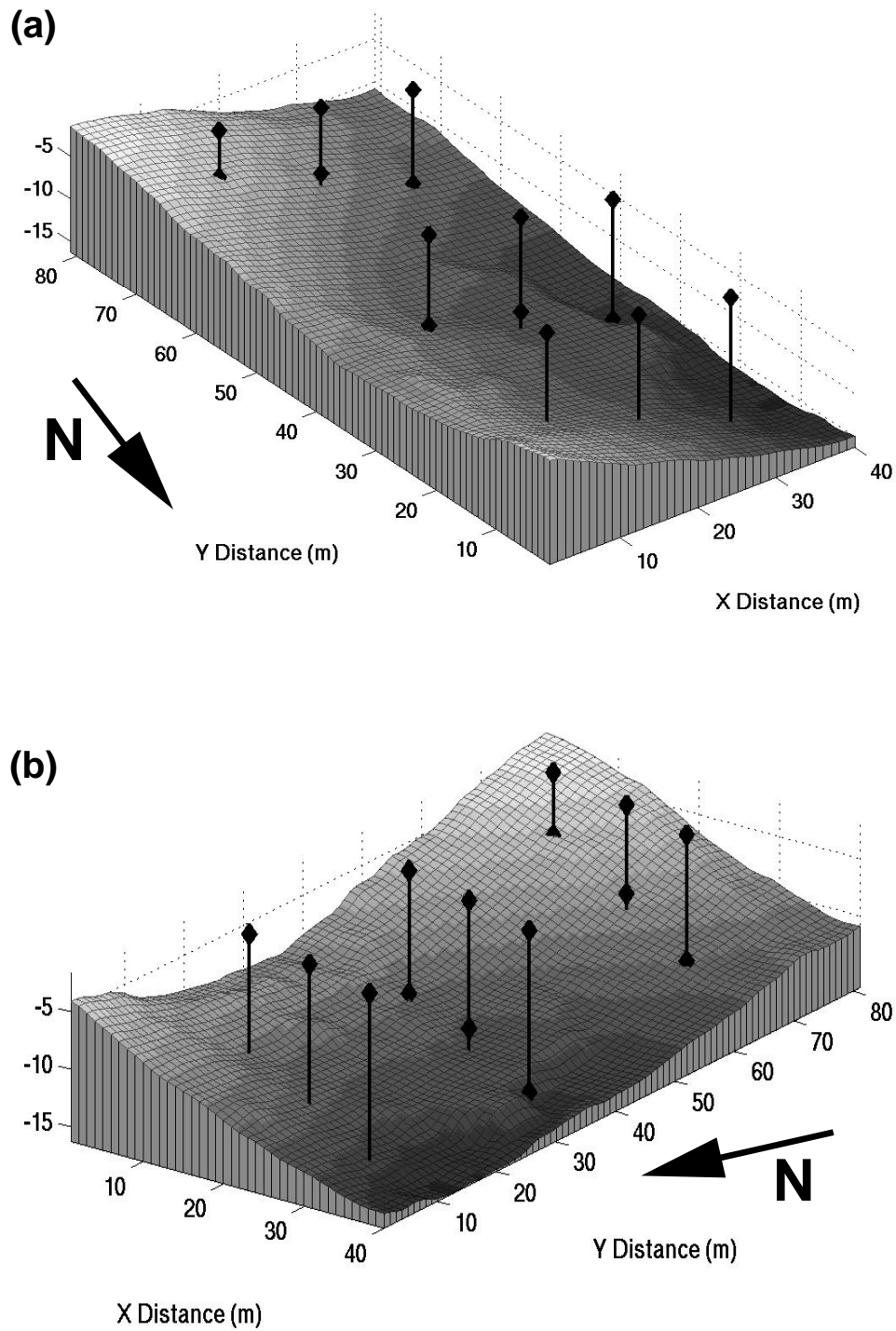


**Figure 5.20:** Final topographic model from different viewpoints. Black lines indicate coring hole positions and diamond markers indicate the surface and cored bedrock depths, respectively. The refractor model and the cored bedrock depth of nine corings are in excellent agreement, although the refractor depth is slightly underestimated in the northernmost part (Brückner, pers. communication).

shotpoint, considering the adversarial influence of the direct arrival and the reliability of the refraction itself. We thus introduce an offset weighted averaging concept (section 4.4) to combine the three models shown in figure 5.19.

A coring campaign in summer 2003 carried out by H. Brückner provided in situ geological information that was used to determine the local refractor depth at nine different positions. The refractor model which still has an error in depth was adjusted with this information.

The minimum rms-error  $\epsilon$  between cored bedrock depth and tuned refractor model is  $\epsilon = 0.44 \text{ m}$  (4.2 %) with an average refractor depth  $z_0 = 10.5 \text{ m}$ . The best tuning factor was  $\gamma = 4$ . Figure 5.20 shows the resulting topographic model  $\tilde{z}'(x, y)$  from different viewpoints. Black lines indicate coring hole positions and diamond markers the surface and cored bedrock depths, respectively. The refractor model and the core bedrock depth are in excellent agreement, although, the refractor depth is slightly underestimated in the northern most part.

### 5.3.2 Interpretation and Discussion

Ground-truthing with coring information has shown, that the 3-D 9-C refraction seismic acquisition and interpretation concept proposed in this paper yields a "high fidelity" refractor topography.

However, the method suffers from a number of drawbacks due to simplifications as shall now be discussed. First of all, the depth of the refractor near the shotpoints is difficult to determine. In principle it can be derived from the intercept formula, but with strongly undulating refractor topography and an unknown overburden velocity at the shot point this information is probably not reliable enough. Thus, coring information had to be used to eliminate the overall erroneous static shift from the final model. It still has to be investigated, if this extra effort can be circumvented by determining the total refractor depth from the seismic data itself with sufficient precision, e.g. by using more shotpoints to determine the overburden velocity.

Also, for reduction and migration constant velocity estimates had to be used for the refractor and the overburden in lack of other information, explaining the remaining misfit between cored bedrock depths and inverted refractor depths, especially obvious in the northernmost part of the refractor. Another explanation for this misfit might be the presence of erosional slope debris causing refracted seismic energy to not directly travel within the bedrock.

In order to further investigate the influence of velocity variations within the refractor and overburden forward finite difference traveltimes modeling (Vidale, 1990; Hole & Zelt, 1995) was performed using the inverted refractor model and the field acquisition geometry. The results are shown in figure 5.21, column three for shots SP1, SP2 and SP3. Figure 5.21, column one shows the picked field data traveltimes and column two shows the percent differences between picked and modeled traveltimes. Comparison reveals a good fit in traveltimes trends but significant misfit in absolute traveltimes. We explain this misfit by the inappropriate assumption that the refractor and the overburden show

a constant velocity field. Tomographic inversion as implemented by Hole (1992), was performed to find the velocity variations which explain the field data traveltimes. The results after 40 iterations are shown in column four of figure 5.21 using a smoothed version of the derived refractor topography as a starting model. The resulting traveltimes are in excellent agreement with the picked field data traveltimes. The corresponding velocity model is shown in figure 5.22. This model exhibits a slight increase in surface velocities (a) and a prominent high velocity zone in the refractor (b). The fact that the derived topographic model shows a reasonable fit with coring information allows for some confidence in the tomographically obtained velocity model.

Figure 5.23 displays the old refractor model (a), derived from 2-D seismics, the magnetic map (b) and the new refractor model (c), derived from 3-D refraction seismics. Compared to the former, the latter shows good correlation with observed linear anomalies (dashed white line in the figure). No significant man-made topographic features such as quay walls or harbour foundations are evident in the refractor. However, the anomaly apparently contours the basin topography. Considering, that the basement of the Milesian Lions' Harbour is shallow enough, it seems possible that appropriate ground could have been prepared by antique workers to found quay wall on sediments or debris.

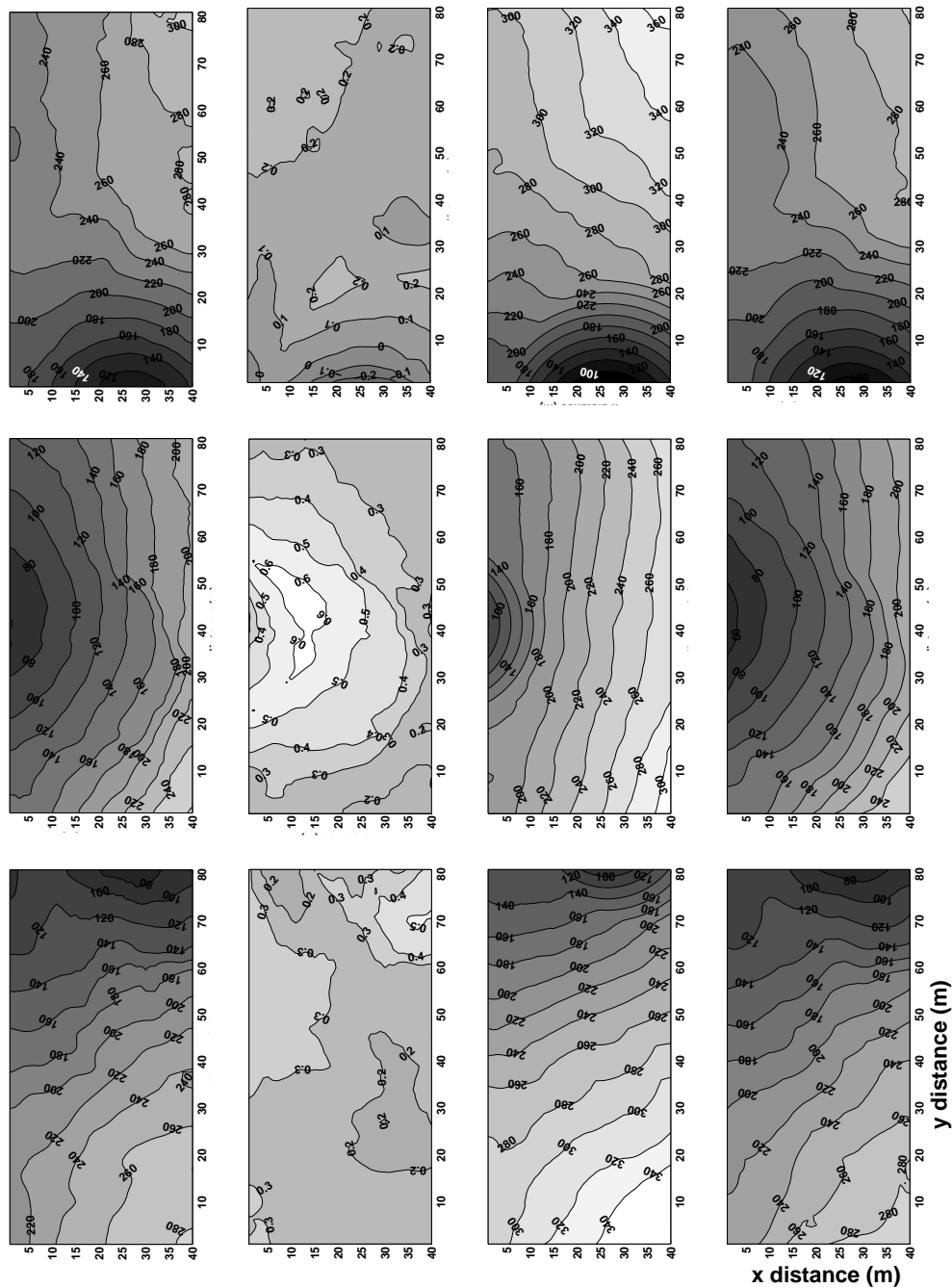


**Figure 5.21:** Results from forward finite difference traveltimes modeling (Vidale, 1990; Hole & Zelt, 1995) using the inverted refractor model and the field acquisition geometry. Column 1 shows the picked field data traveltimes, column 3 modeled traveltimes and column 2 shows the percent differences between picked and modeled traveltimes for shots SP1, SP2 and SP3 (rows 1,2 and 3, respectively). Comparison reveals a good fit in traveltime trends but significant misfit in absolute traveltimes. Column 4 shows results from tomographic inversion (Hole, 1992) in excellent agreement with the picked field data traveltimes.

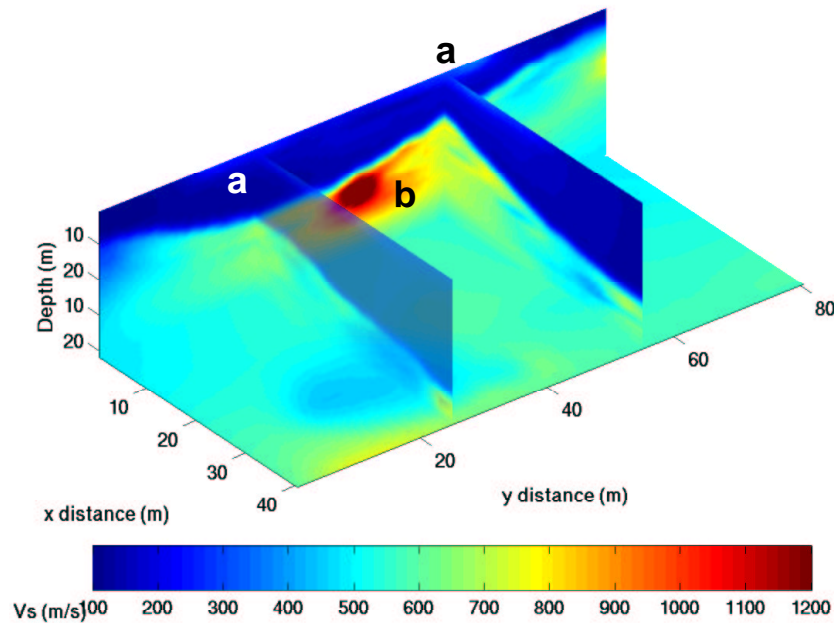


**Figure 5.22:** Velocity model after 40 iterations with tomographic inversion (Hole, 1992). This model exhibits a slight increase in surface velocities (a) and a prominent high velocity zone in the refractor (b).

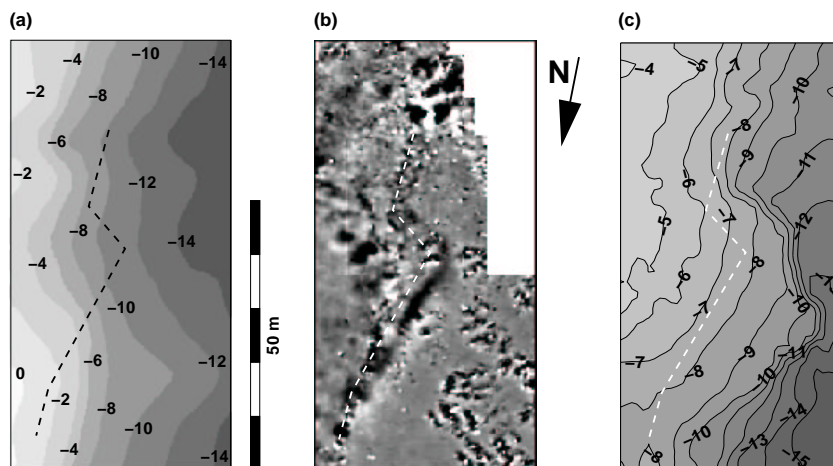


**Figure 5.23:** Comparison between old refractor topography, derived from 2-D surveys (a), magnetic map (b) and new refractor topography, derived from the 3-D survey (c). The magnetic anomaly is indicated by a dashed line. While in the old model the line apparently does not correlate with depth structures, in the new model it contours the basin topography.



# Chapter 6

## Discussion and Conclusions

In the scope of this thesis a new high resolution 3-D multi-component shearwave refraction seismic technique for shallow acquisition was developed. Preceding geophysical work in the alluvial sedimentary environment of the archaeological site of Miletus' Lions' Harbour (Turkey) raised the question whether suspicious anomalies observed on magnetic data could be related to man-made structures in the subsurface. Close-spaced 2-D shear wave seismic refraction surveys did not provide sufficient lateral resolution. Thus, reliability and two 3-D multi-component refraction surveys were carried out covering the anomalies in order to clarify the situation. The experiment, moreover, aimed to evaluate the potential of this new technique. The acquisition concept was verified, complex dynamic and kinematic wavefield phenomena were scrutinized, as well as wavefield separation techniques and a new refractor imaging method were developed and tested. The test site, the silted Lions' harbour of the antique ruin city of Miletus, provided us with a lithologically simple situation where structural complexity is introduced by remnants of buildings and basement topography.

A number of new and important insights was obtained. We were able to proof that the acquisition concept, i.e. shooting lines successively, rather than acquiring in one full 2-D spread is suited to record a coherent wavefield. The resulting geophone grid with 1 *m* spacing provides sufficient lateral sampling. The realization of a vector source with a man-driven sledgehammer was repeatable enough to serve our purpose. From our experience recording three components simultaneously with Gal'perin geophones results in better polarization quality than the use of single component geophones. Although the geological setting makes the Lions' Harbour an almost perfect field laboratory, in the second experiment problems occurred with geophone planting and coupling due to significant mud cracks and tamarisk cover. The most obvious disadvantage of the method is the relative great logistic effort and the large amount of data involved. In addition, in this particular case the extremely dry and hard surface sediments made planting of the geophones only possible by pre-drilling holes. In the second experiment the vertical source and receiver component was recorded but not used in the subsequent processing and imaging (see appendix B).

---

The complexity of the direct, refracted and reflected wavefield was impressive already at the first data inspection. Methodically the following aspects turned out to be important:

- An isotropic radiation pattern of compressional shear- and surface waves can be generated without practical problems by simple vector arithmetics even if man-driven hammer blows act as a seismic source.
- Wavefront bending due to refractor geometry or velocity heterogeneity is significant. Effects are amplified by the enormous velocity contrast found in near surface layers. The comparison between refractor models derived from "true" 3-D seismic acquisition and parallel 2-D lines showed that the refractor is more flat than initially assumed but greater topographic detail was revealed.
- We were surprised by the richness of geological details even below the wavelength limit. Surface waves are able to map sharp lateral material contrast with lower than wavelength accuracy. Even the influence of mud cracks could be imaged in the coda of ground coupled airwaves and radiation patterns. Simple delay time techniques applied to SH-refracted arrivals are capable to map coherent basement structures in the meter-scale which would clearly have been smoothed out as "noise" if data had been acquired in a coarser grid or along linear 2-D profiles.

If acquired in 3-D seismic vector data have the potential to resolve lateral velocity heterogeneity with high resolution. However, due to acquisition geometry and wavefield characteristics different phases of the wavefield intermix. Interpretation of S-wave data in 3-D is improved if orthogonal horizontal point sources are applied. Simple mathematical vector operations help significantly in the interpretation even of complex wavefields. To avoid complications in travelttime interpretation the wavefield must be separated leading to transverse or radial acquisition geometries.

Three different approaches to wavefield separation were investigated. The first and most naive concept uses simple wavefield component rotation to geometric ray direction and is strictly valid only for the direct wavefield, where it works best. This idea, however, suffers from the simplifying assumption of a cylinder symmetric direct wavefield which does not hold for the Lions' Harbour surveys, where velocity variations in the surface layer are obvious. Also this approach is strictly invalid for the refracted wavefield if refracted events are bended. Application to field data, however, shows that the seismic vectorfield was recorded with sufficient accuracy to apply vector based wavefield separation techniques.

The second approach is based on separating the wavefield by calculating curl and divergence at the surface, thus yielding energy sections only comprising longitudinally and transversely polarized wavefield components. These contain only part of the respective energy contribution, because the vertical derivative can not be calculated due to the lack of spatial sampling in depth. Also the operations are sensitive to the grid spacing realized in the field. Surface wavefield separation performed better than refracted wavefield separation. One possible explanation is the high-pass filter effect caused by the

derivative operator.

The best result for direct as well as refracted wavefields was yielded by the so-called slowness projection, aligning the recorded wavefield approximately parallel or perpendicular to the wavefronts. Slowness is determined data-driven and thus, the method depends on good signal to noise ratio and polarization fidelity, proving the sufficient quality of the data acquired here.

The refractor imaging technique developed in this thesis uses data separated by slowness projection as input. The method relies on interpreter interaction and some experience with 3-D data and in identifying the direct and refracted wavefield in the seismogram. Which also is a possible source for error to some extent. Confidence in the resulting subsurface model is increasing with the amount of shotpoints used, alas also is acquisition effort. Other sources of error are the estimated and assumed constant velocities of the refractor and overburden, which influence the necessary velocity reduction and following migration. The resulting model is undetermined in depth, but in our case should be adjusted by available coring information. The minimum rms-error  $\epsilon$  between cored bedrock depth and tuned refractor model is  $\epsilon = 0.44m$  (4.2 %) with an average refractor depth of  $z_0 = 10.5m$ . Supplemental tomographic inversion using the refractor topography model as input in addition provided a plausible velocity model, exhibiting characteristic surface anomalies and a prominent high velocity zone in the refractor.

Regarding the archaeological background of our measurements we could show that the antique moles, possibly represented by coinciding magnetic anomalies and Rayleigh velocity contrasts, were apparently not founded on solid rock but on sediments or debris. Unfortunately, we were not able to explain the origin of magnetic anomalies or give an archaeological explanation by now. Spectral analysis of the surface wavefield, however, gave some indication for a seismic anomaly in about 3 – 6 m depth, which is not "seen" by the refracted wave. Thus, we conclude, that there are no topographic features in the former harbour basin, explicitly representing a quay wall. On the other hand, it was shown that the basement of the Milesian Lions' Harbour is shallow enough to provide appropriate ground for antique construction workers to found such structures.

A new robust and simple seismic method is developed and presented, which allows for imaging refractor topography with high fidelity in 3-D.

# References

- AKI, K., & RICHARDS, P.G. 2002. *Quantitative Seismology*. second edn. Sausalito, California, USA: University Science Book.
- ATKINSON, R. J. C. 1952. Methodes electriques de prospection en archeologie. *Pages 59–70 of: LAMING, A. (ed), La Decouvert de Passe*. Paris: Picard.
- BAY, B. 1996. *Das Neogen der Umgebung von Milet*. Diplomkartierung, Universität Bochum, Bochum.
- BAY, B. 1999. *Geoarchäologie, anthropogene Bodenerosion und Deltavorbau im Büyük Menderes Delta (SW-Türkei)*. D294. Herdecke: GCA-Verlag. Dissertation Universität Bochum.
- BAYHAN, S. 1997. *Priene-Miletos-Didyma*. Keskin Color Kartpostalcilik LTD. STI, Matbaasi, Sirkeci, Türkiye.
- BELFER, I., BRUNER, I., KEYDAR, S., KRAVTSOV, A., & LANDA, E. 1998. Detection of shallow objects using refracted and diffracted seismic waves. *Journal of Applied Geophysics*, **38**, 155ff.
- BENJUMEA, B., TEIXIDO, T., PEÑA, J. A. BENJUMEA, B., TEIXIDO, T., & PEÑA, J. A. 2000. Application of the CMP refraction method to an archaeological study (Los Millares, Almería, Spain). *Journal of Applied Geophysics*, **1274**, 2–8.
- BENNETT, G. 1999. 3-D seismic refraction for deep exploration targets. *Leading Edge*, **18**, 186–191.
- BLOTT, J.E., DAVIS, T.L., & BENSON, R.D. 1999. Morrow sandstone reservoir characterization: A 3-D multicomponent seismic success. *Leading Edge*, **18**, 394ff.
- BOHLEN, T. 2002. Parallel 3-D viscoelastic finite difference seismic modelling. *Computer & Geosciences*, **28**(8), 887–899.
- BRÜCKNER, H. 1996. Geoarchäologie an der türkische Ägäisküste. *Geographische Rundschau*, **48**, 568ff.

- BRÜCKNER, H. 1998. Coastal Research and Geoarchaeology in the Mediterranean Region. *Page 235ff of: KELLETTAT, D.H. (ed), German Geographical Coastal Research - The Last Decade.* Tübingen, Germany: Institut for Scientific Co-operation.
- BRÜCKNER, H. 2003. Delta Evolution and Culture - Aspects of Geoarchaeological Research in Miletos and Priene. *Chap. 9, page 121ff of: WAGNER, G.A., PERNICKA, E., & UERPMANN, H.-P. (eds), Troia and the Troad - Scientific Approaches.* Berlin, Heidelberg, New York: Springer-Verlag.
- BRÜCKNER, H., MÜLLENHOFF, M., HANDL, M., & KLAAS, B. VAN DER. 2002. Holocene landscape evolution of the Büyük Menderes Alluvial Plain in the environs of Myous and Priene (Wetsren Anatolia, Turkey). *Z. Geomorph. N.F., Suppl.-Bd. 127*, 47–65.
- CARDARELLI, E., & NARDIS, R. DE. 2001. Seismic refraction, isotropic anisotropic seismic tomography on an ancient monument (Antonio and Faustina temple AD 141). *Geophys. Prospecting*, **49**, 228–240.
- CLAERBOUT, J. 1976. *Fundamentals of Geophysical Data Processing.* New York: Mc-Graw-Hill.
- CLAERBOUT, J.F. 1971. Toward a unified theory of reflector mapping. *Geophysics*, **36**(3), 467–481.
- CLAERBOUT, J.F. 1985. *Imaging the Earth's Interior.* Oxford: Blackwell Scientific Publication.
- CLAYTON, R. W., & A., MCMECHAN G. 1981. Inversion of refraction data by wave field continuation. *Geo*, **46**(6), 860–868.
- CLIET, C., & DUBESSET, M. 1987. Three-component recordings - interest for land seismic source studies. *Geophysics*, **52**, 1048–1059.
- DELLINGER, J., & J., ETGEN. 1990. Wave-field separation in two-dimensional anisotropic media. *Geophysics*, **55**(7), 914–919. Short Note.
- DELLINGER, J., BRANDSBERG-DAHL, S., CLARKE, R., & THOMSON, L. 2002. Alford rotation after tensor migration. *Pages 982–985 of: SEG International Exposition and 72nd Annual Meeting.* SEG, Salt Lake City, Utah, USA.
- DOBECKI, T. L., & SCHOCH, R. M. 1992. Seismic investigations in the vicinity of the Great Sphinx of Giza, Egypt. *Geoarchaeology*, **7**, 527–544.
- DOUGHERTY, D.E., & STEPHEN, R.A. 1988. Seismic energy partitioning and scattering in laterally heterogeneous oceanic crust. *Pure and Applied Geophysics*, **128**, 195ff.

- EBROM, D., KRAIL, P., RIDYARD, D., & SCOTT, L. 1998. 4-C/4-D at Teal South. *Leading Edge*, **17**, 1450ff.
- ERKUL, E. 2003. Development of a mobile multi-sensor system: first results. *Pages 159–160 of: KOBYLÍŃSKI, Z., & HERBICH, T. (eds), Archaeologia Polona*, vol. 41. Warsaw, Poland: Institute of Archaeology and Ethnology, Polish Academy of Sciences.
- GAISER, J.E. 1999. Applications for vector coordinate systems of 3-D converted-wave data. *The Leading Edge*, **18**(11), 1290–1300.
- GAL'PERIN, E. I. 1984. *The Polarization Method of Seismic Exploration*. Dordrecht: D. Reidel Publishing Company.
- GARDNER, L.W. 1939. An areal plan of mapping subsurface structure by refraction shooting. *Geophysics*, **4**, 247–259.
- GRAEVE, V. VON. 1996. Zu den Hafenlöwen von Milet. *Pages 317–327 of: BLAKOLMER, F., KIERER, K.R., KRINZINGER, F., LANDSKRON-DINSTL, A., SZEMETHY, H.D., & ZHUBER-OKROG, K. (eds), Fremde Zeiten*, vol. Bd.1. Wien, Austria: Phiobos Verlag.
- HAGEDOORN, J.G. 1959. The plus-minus method of interpreting seismic refraction sections. *Geophysical Prospecting*, **7**, 158–182.
- HARDAGE, B.A., DEANGELO, M., & MURRAY, P. 2003. Defining P-wave and S-wave stratal surfaces with nine-component VSPs. *Leading Edge*, **22**(8), 720–729.
- HILL, N.R. 1987. Downward continuation of refracted arrivals to determine shallow structure. *Geophysics*, **52**, 1188–1198.
- HOLE, J.A. 1992. Nonlinear High-Resolution Three-Dimensional Seismic Travel Time Tomography. *J. Geophys.Res.*, **97**(B5), 6553–6562.
- HOLE, J.A., & ZELT, B.C. 1995. 3-D finite difference reflection traveltimes. *Geophys. J. Int.*, **121**, 427–434.
- KÄHLER, S., & MEISSNER, R. 1983. Radiation and Receiver Pattern of Shear and Compressional Waves as a Function of Poisson's Ratio. *Geophysical Prospecting*, 421ff.
- KARASTATHIS, V.K., & PAPAMARINOPOULOS, S.P. 1997. The detection of king Xerxes canal by use of shallow reflection and refraction seismics - preliminary results. *Geophysical Prospecting*, **45**, 389ff.
- KLEINER, G. 1968. Die Ruinen von Milet. *Walter de Gruyter & Co. Berlin*.

- KOMMEDAL, J.H., & TJOSTHEIM, B.A. 1989. A Study of different methods of wavefield separation for application to VSP data. *Geophysical Prospection*, **37**, 117–142.
- LEVANDER, A.R. 1988. Fourth-order finite-difference P-SV seismograms. *Geophysics*, **53**(11), 1425–1436.
- LIU, E., MAULTZSCH, S., CHAPMAN, M., LI, X.-Y., QUEEN, J.H., & ZHANG, Z. 2003. Frequency-dependent seismic anisotropy and its implication for estimating fracture size in low porosity reservoirs. *TLE*, **22**(7), 662ff.
- MARGRAVE, G.F., LAWTON, D.C., & STEWART, R.R. 1998. Interpreting channel sands with 3C-3D seismic data. *Leading Edge*, **17**, 509ff.
- MAULTZSCH, S., CHAPMAN, M., LIU, E., & LI, X.-Y. 2003. The potential of measuring fracture size with frequency-dependent shear-wave splitting. *FB*, **21**(7), 45ff.
- MORSE, P., & FESHBACH, H. 1953. *Methods of Theoretical Physics*. McGraw-Hill.
- MUSMANN, P. 2003 (Februar). *3D-Refraktionsseismisches Imaging am Beispiel des Kalabaktepe in Milet*. Diplomarbeit, Christian-Albrechts-Universität, Institut für Geowissenschaften, Abteilung Geophysik, Kiel.
- NIEMEIER, B., & NIEMEIER, W.-D. 1997. Projekt minoisch-mykenisches bis proto-geometrisches Milet: Zielsetzung und Grabung auf dem Stadthügel und am Athenatempel. *AA*, 189–249.
- PALMER, D. 1981. The generalized reciprocal method of seismic refraction interpretation. *Geophysics*, **46**, 1508–1518.
- PALMER, D. 1986. Refraction seismics - the lateral resolution of structure and seismic velocity. In: HELBIG, K., & TREITEL, S. (eds), *Seismic exploration*, vol. 13. London: Geophysical Press.
- PALMER, D. 2001a. Amplitude "statics" in shallow refraction seismology. In: *15th Geophysical Conference and Exhibition*. ASEG. Extended Abstracts.
- PALMER, D. 2001b. Imaging refractors with the convolution section. *Geophysics*, **66**(5), 1582–1589.
- PALMER, D. 2001c. Resolving refractors ambiguities with amplitudes. *Geophysics*, **66**(5), 1590–1593.
- PIIP, V.B. 2001. 2D inversion of refraction travelttime curves using homogeneous functions. *GP*, **49**, 461–482.

- RICHWALSKI, S., ROU-CHOWDHURY, K., & MONDT, J.C. 2000. Practical aspects of wavefield separation of two-component surface seismic data based on polarization and slowness estimates. *Geophysical Prospecting*, **48**(4), 697–722.
- ROBERTSSON, J.O.A, & CURTIS, A. 2002. Wavefield separation using densely deployed three-component single-sensor groups in land surface-seismic recordings. *Geophysics*, **67**(5), 1624–1633.
- ROBERTSSON, J.O.A, & MUYZERT, E. 1999. Wavefield separation using a volume distribution of three component recordings. *Geophysical Research Letters*, **26**(18), 2821–2824.
- ROBERTSSON, J.O.A, BLANCH, J.O., & SYMES, W.W. 1994. Viscoelastic finite-difference modeling. *Geophysics*, **59**(9), 1444–1456.
- SCHRÖDER, B., BRÜCKNER, H., STÜMPEL, H., & YALCIN, Ü. 1995. Geowissenschaftliche Umfelderkundung. *AA*, 238–244.
- STOLT, R.H. 1978. Migration by Fourier Transform. *Geophysics*, **43**(1), 23–48.
- STRIGHT, M. J. 1986. Evaluation of archaeological site potential on the Gulf of Mexico continental shelf using high-resolution seismic data. *Geophysics*, **51**, 605–622.
- STÜMPEL, H. 2001. Geophysikalische Prospektion in Milet 1998-1999. *Archäologischer Anzeiger*, 418ff.
- STÜMPEL, H., & MEISSNER, R. 1982. Haithabu - Entdeckung neuer Funde durch hochauflösende kleinseismische Messungen. *Naturwissenschaften*, **69**, 353–360.
- STÜMPEL, H., KÄHLER, S., MEISSNER, R., & MILKERREIT, B. 1984. The use of seismic shear waves and compressional waves for lithological problems of shallow sediments. *Geophysical Prospecting*, **32**, 662–675.
- STÜMPEL, H., RABEL, W., & SCHADE, J. 1988. Oberflächennahe geophysikalische Untersuchungen im Mündungsgebiet des Rio de Velez und des Rio Algarrobo. *Madriider Beiträge*, **14**, 60ff.
- STÜMPEL, H., DEMIREL, F., LORRA, S., & WENDE, S. 1995. Geophysikalische Messungen im Umfeld von Milet. *Archäologischer Anzeiger*, 245ff.
- STÜMPEL, H., BRUHN, C., DEMIREL, F., GRÄBER, M., PANITZKI, M., & RABEL, W. 1997. Stand der geophysikalischen Messungen im Umfeld von Milet. *Archäologischer Anzeiger*, 124ff.
- STÜMPEL, H., DEMIREL, F., RABEL, W., TRINKS, I., & WÖLZ, S. 1999. Geophysikalische Prospektion im Umfeld von Milet 1996-1997. *Archäologischer Anzeiger*, 89ff.



- TELFORD, W.M., GELDART, L.P., & SHERIFF, R.E. 1991. *Applied Geophysics*. 2nd edn. Cambridge: Cambridge University Press.
- THORNBURGH, H.R. 1930. Wavefront diagrams in seismic interpretation. *Bull. A. A. P. G.*, **14**, 185–200.
- TSOKAS, G.N., PAPAACHOS, C.B., VAFIDIS, A., LOUKOYIANNAKIS, M.Z., VARGEMEZIS, G., & TZIMEAS, K. 1995. The detection of monumental tombs buried in tumuli by seismic refraction. *Geophysics*, **60**, 1735ff.
- TUTTAHS, G. 1995. Wasserbauliche Problemfelder am Grabungsplatz Milet: Zustand und Aufgaben. *AA*, 265–275.
- VIDALE, J.E. 1990. Finite-difference calculation of traveltimes in three dimensions. *Geophysics*, **55**(5), 521–526.
- WEINSTEIN-EVRON, M., MART, Y., & BECK, A. 1991. Geophysical investigations in the el-Wad Cave, Mt. Carmel, Israel. *Geoarchaeology*, **6**, 355–365.
- WINTERSTEIN, D., STEFANI, J., JOHNSON, S., & JULANDER, D. 1998. 9-C time lapse VSP monitoring of steam injection at Cymric Oil Field. *Leading Edge*, **17**, 527ff.
- WÖLZ, S., & RABBEL, W. 2003. Shear wave polarizations in exploring shallow 3-D media. *in preparation*.
- WULLSTEIN, A. 2001. *Die holozäne Landschaftsentwicklung im Gebiet der antiken Stadt Milet. Ein Beitrag zur Paläogeographie Westanatoliens*. Diplomarbeit, Philipps-Universität, Marburg.
- WYNN, J. C. 1986a. Archaeological prospection - an introduction to the issue. *Geophysics*, **51**, 533–537.
- WYNN, J. C. 1986b. A review of geophysical methods used in archaeology. *Geoarchaeology*, **1**, 245–257.

# Appendix A

## Technical Miscellanea

In this appendix a set of additional information is given, regarding circumstances of the acquisition, and basic processing.

At the time of actual acquisition in survey  $\mathcal{B}$  the survey area was characterized by significant mud cracks due to the dry soil, tamarisk roots remanent from preparatory cutting by local workers, excavation debris and obvious topography. During the campaign the area was thus mapped visually, aided by the measuring tape used to position the geophones, to serve as a reference when interpreting surface wavefields or possible artefact observed in the data. Figure A.1 shows the resulting map.

For the same survey three-component Gal'perin geophones were used. These geophones also referred to as triphons are built from three identical receivers which are dipping  $54.7^\circ$  from vertical and are rigidly mounted into their housing. The azimuth between the individual components is  $120^\circ$  (Gal'perin, 1984).

In order to illustrate the principle assembly of these geophones figure A.2a shows a technical sketch. In panel (b) the geometry of the Gal'perin coordinate system with components  $u, v, w$  and its relation to the Cartesian coordinate system  $x, y, z$  is displayed. Also shown are the corresponding transformation equations.

For detailed processing steps please refer to figure A.3.

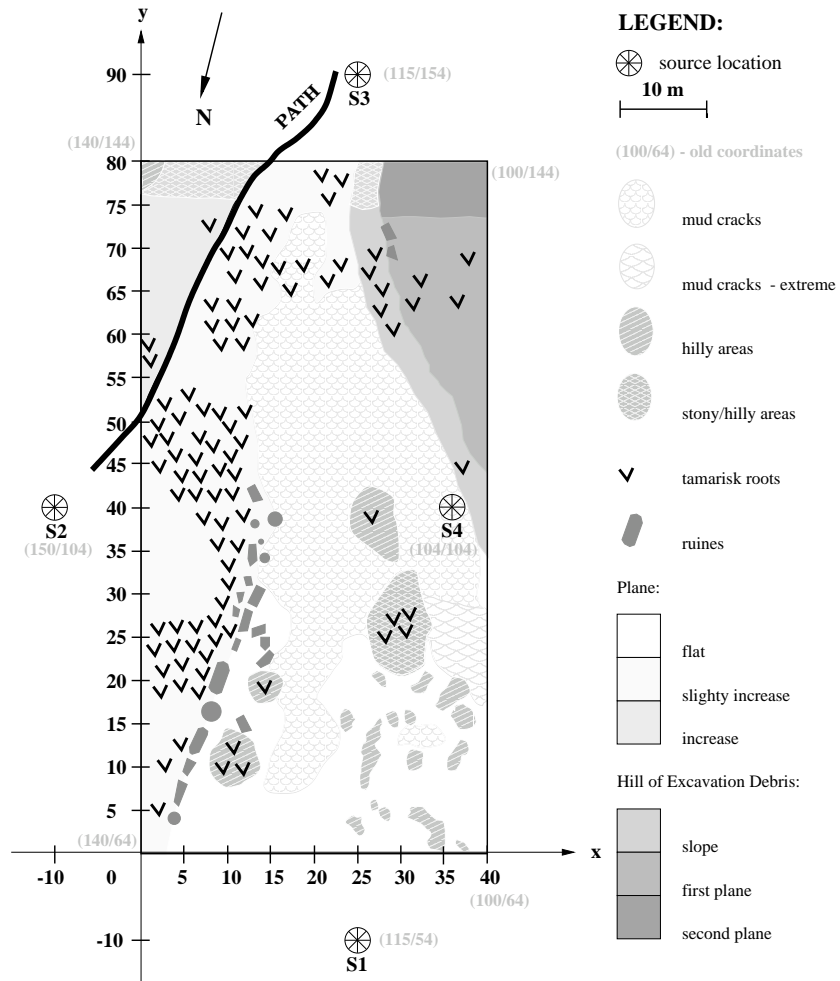


**Figure A.1:** Mapped area of survey  $\mathcal{B}$  as it was in summer 2000

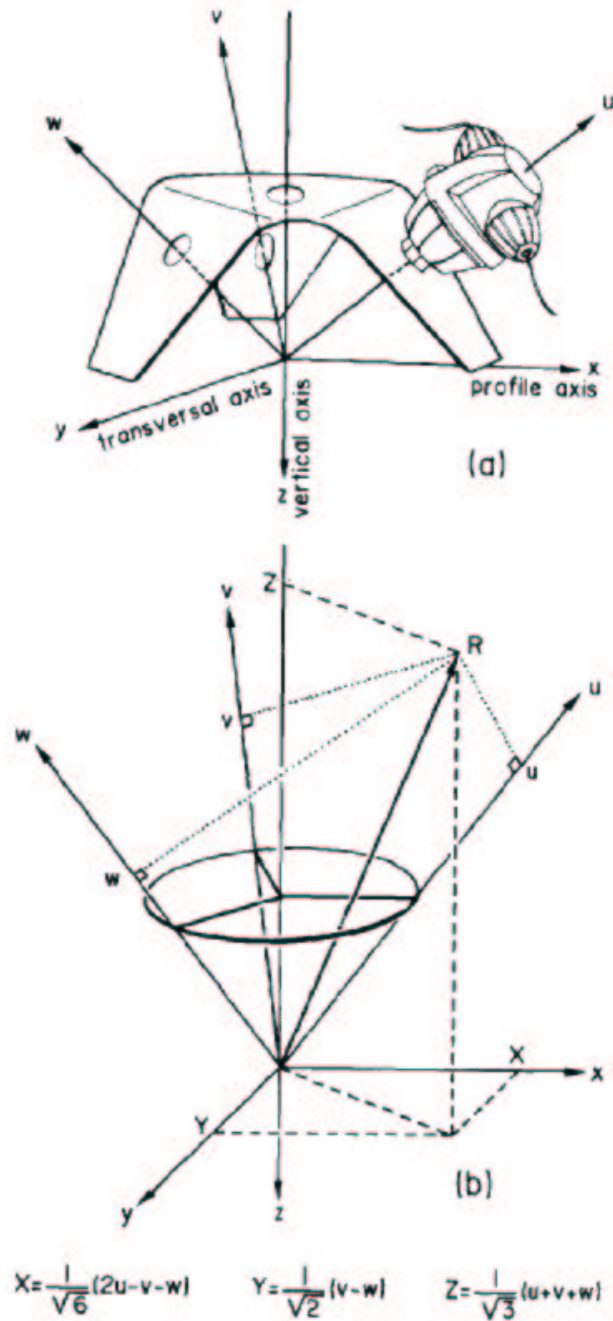


**Figure A.2:** (a) schematic view of the triphon, only one of the three geophones is represented; (b) Principle of the triphone showing the basic trihedron and the resultant R after Cllet & Dubesset (1987).

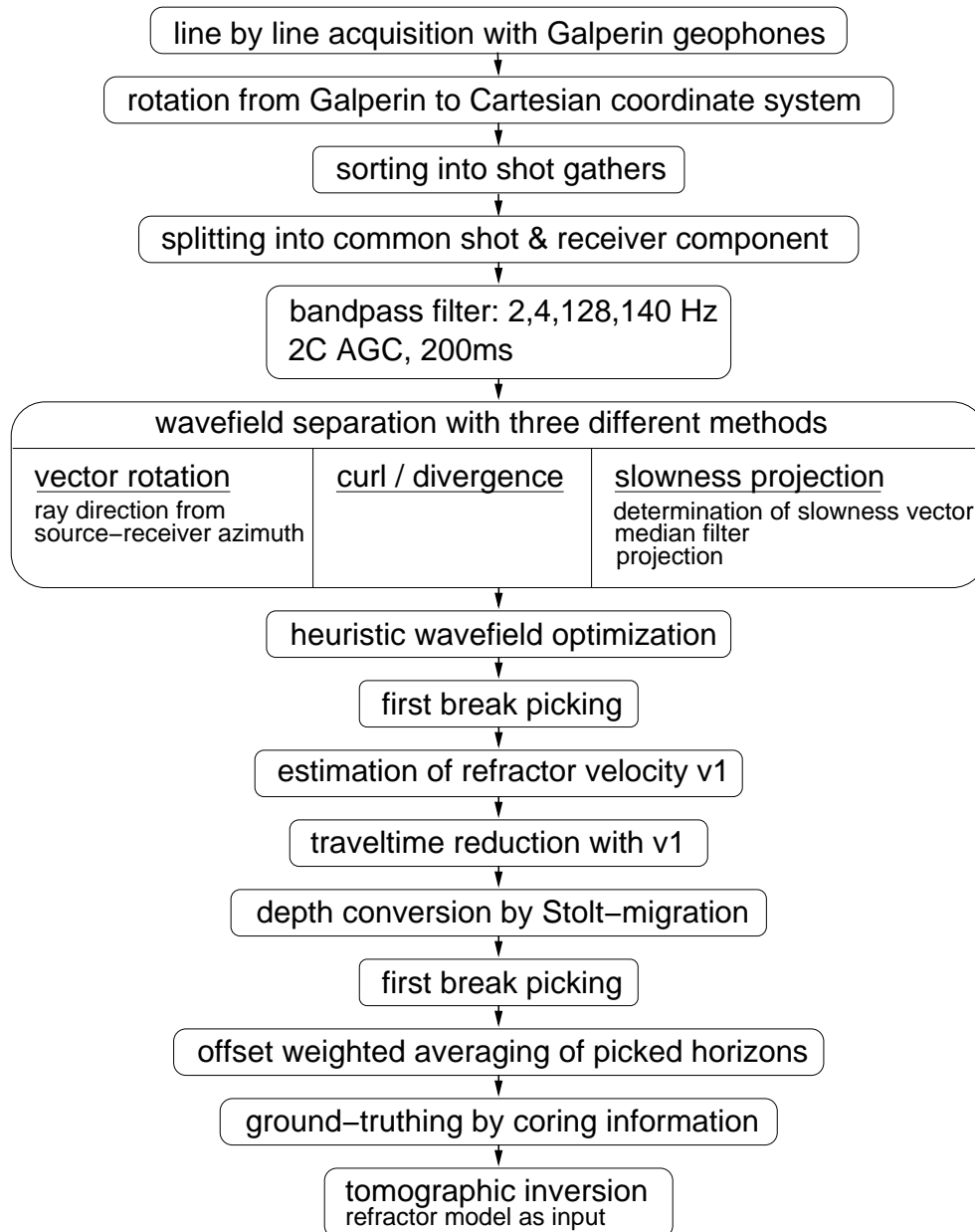


**Figure A.3:** Processing flow.

# Appendix B

## Additional Data Examples

In the following timeslices of all four shotpoints from area *B* are plotted in sequences from 60 *ms* to 280 *ms* with 20 *ms* separation. This assembly is intended to give an overview of the data multiplicity and richness of wavefield phenomena as well as to further document the performance of the "slowness projection" wavefield separation method. The figures also demonstrate how well recordings of the vertical wavefield component correspond to the radial configuration obtained after wavefield separation. The sequences also illustrate how the refracted P wave rapidly escapes in the water table and thus, cannot be used for refractor topography investigation.

For a listing of all figures please refer the table shown below. Please note, that data displayed in figures B.2, B.5, B.8, and B.11 were involved in the imaging process described in section 5.3.

<b>Shotpoint</b>	vertical component	radial component (slowness projection)	transverse component (slowness projection)
<b>S1</b>	B.1	B.2	B.3
<b>S2</b>	B.4	B.5	B.6
<b>S3</b>	B.7	B.8	B.9
<b>S4</b>	B.10	B.11	B.12

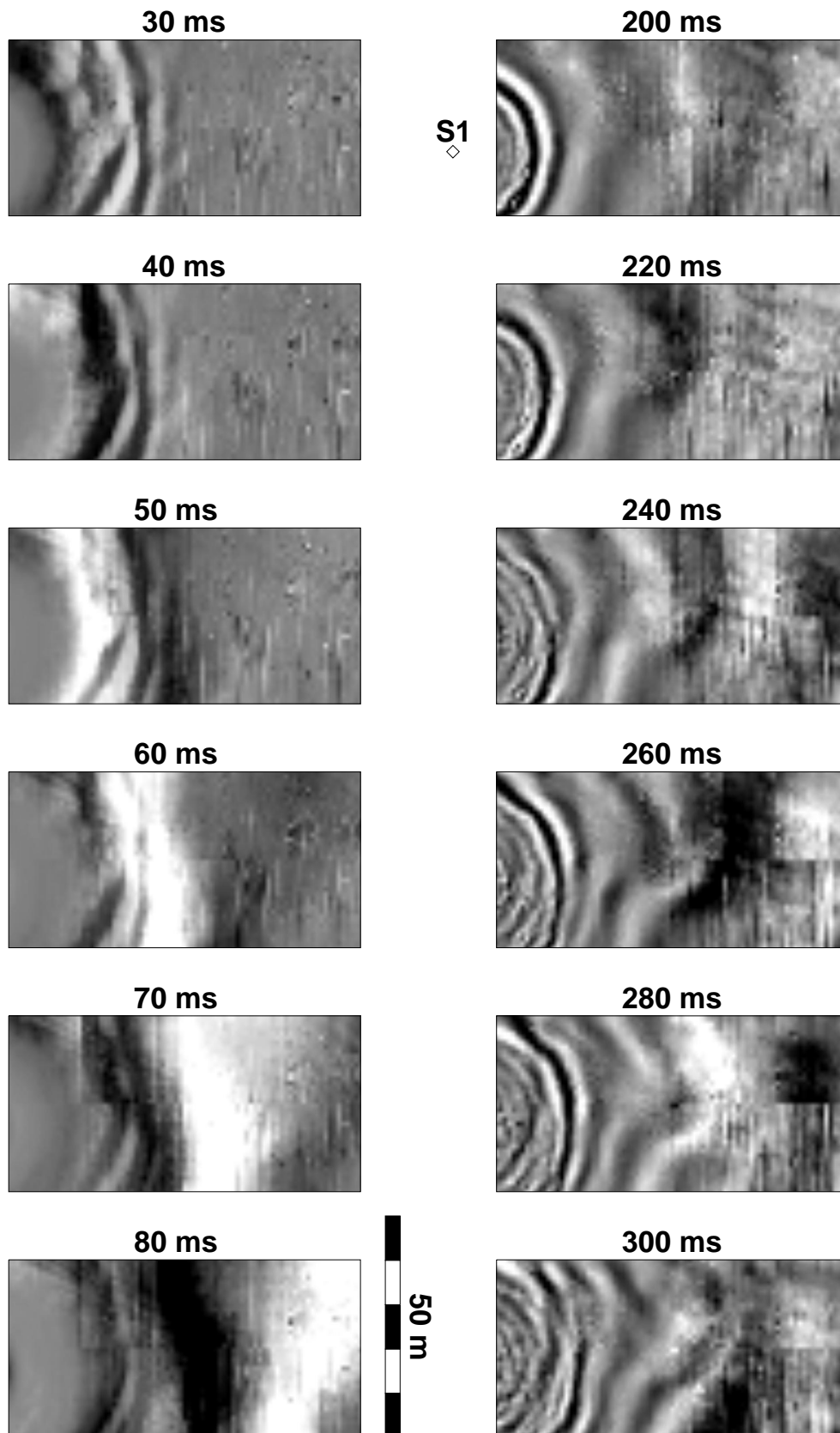


**Figure B.1:** Sequence of time slices for the recorded vertical component of shotpoint S1. On the left hand side time slices start at 30ms with 10ms time increment for illustration of P waves refracting into the water table. On the right hand side timeslices start at 200ms with 20ms time increment illustrating converted and surface waves.

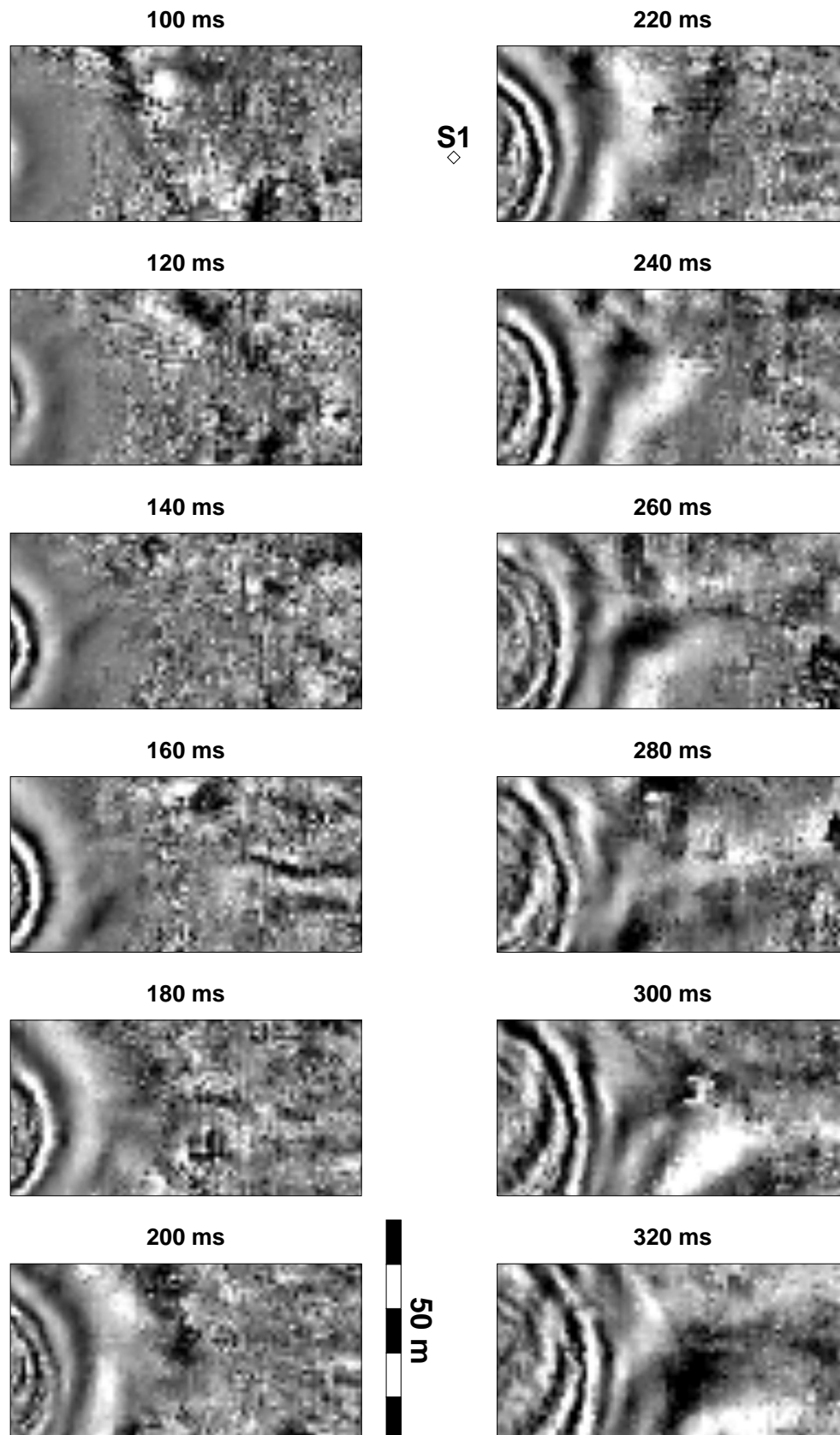


**Figure B.2:** Sequence of time slices with 20ms time increment, starting at 100ms for the radial configuration after slowness projection for shotpoint S1 with shot direction Y.



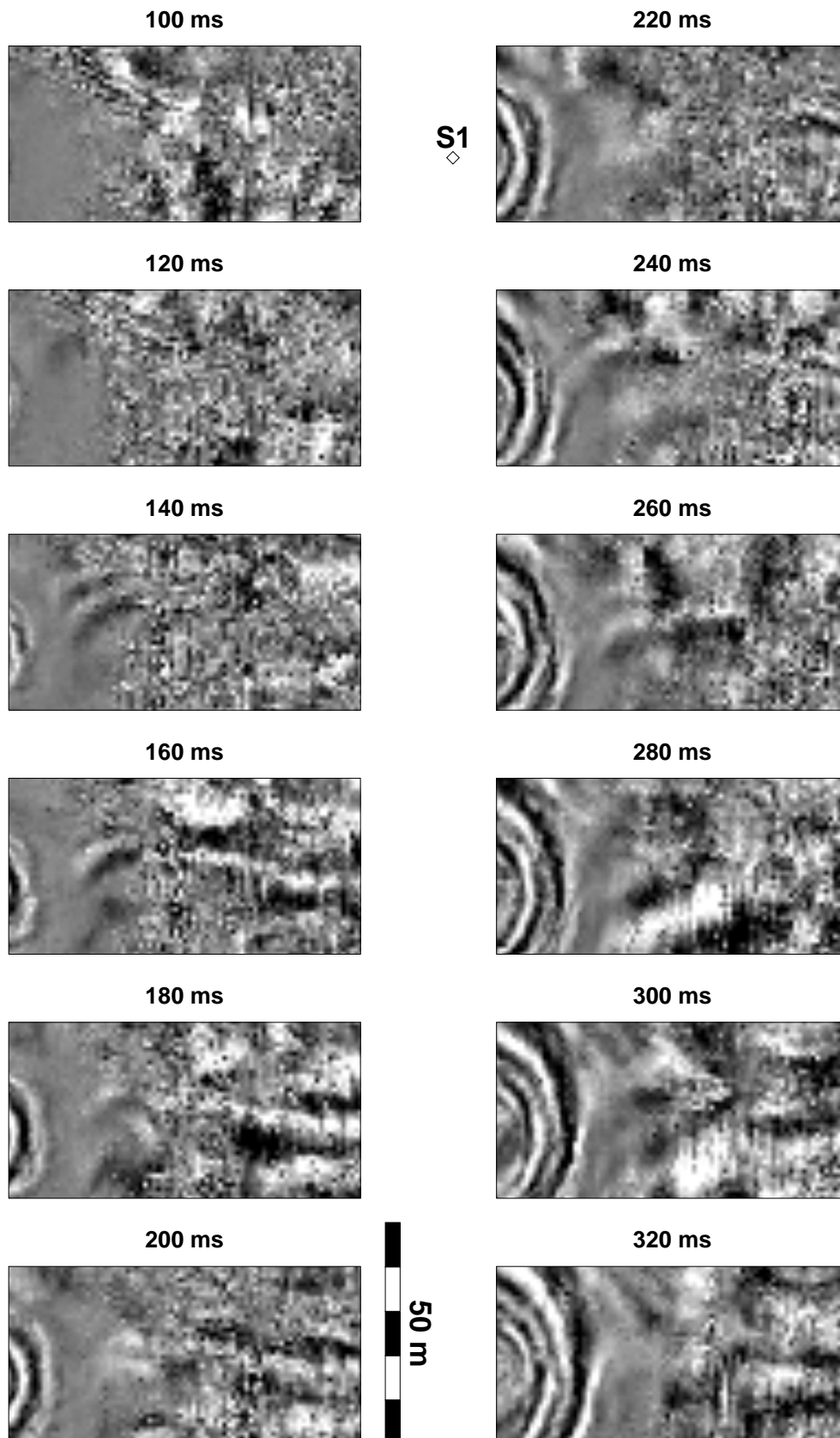


**Figure B.3:** Sequence of time slices with 20ms time increment, starting at 100ms for the transverse configuration after slowness projection for shotpoint S1 with shot direction  $X$ .

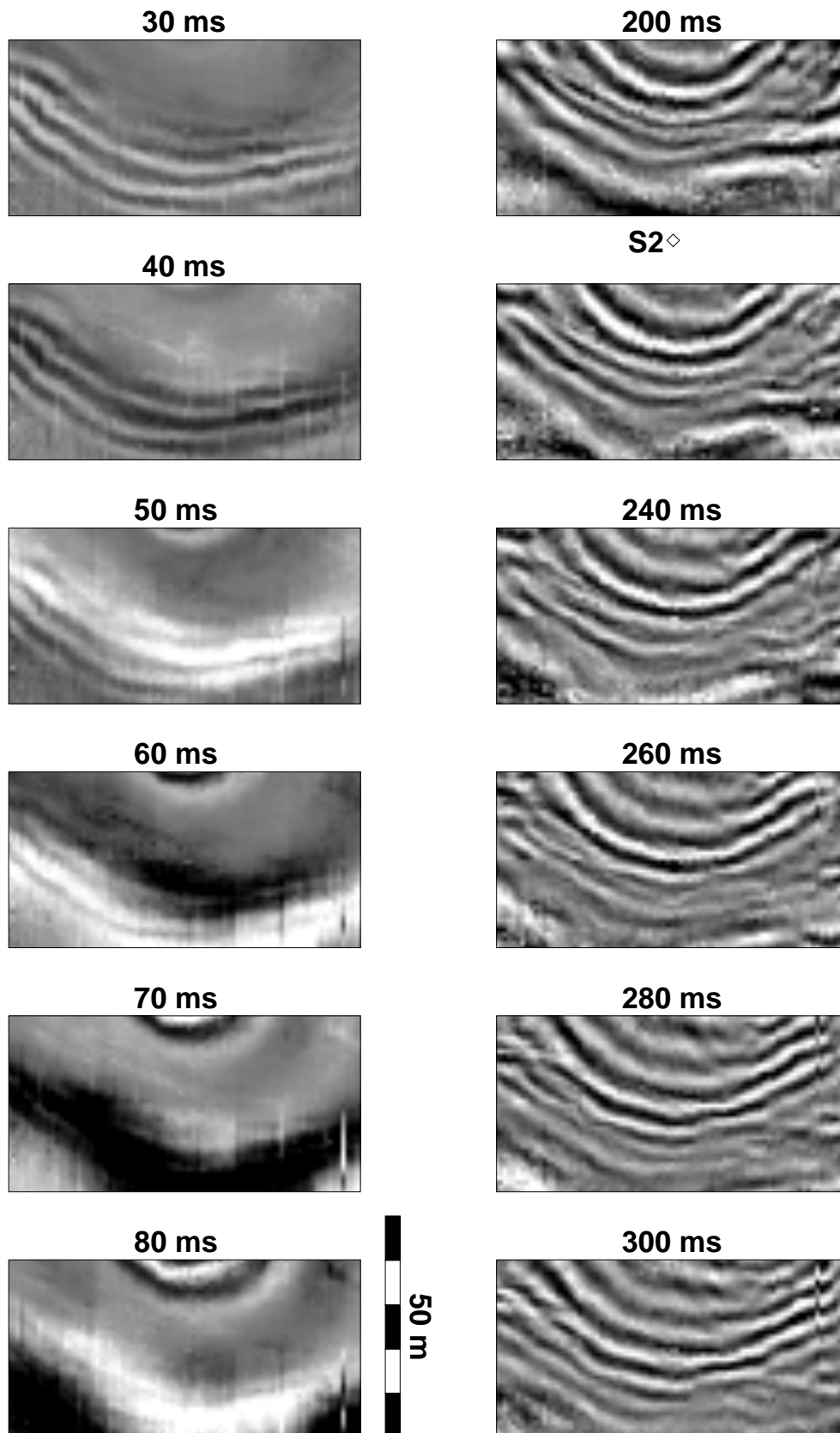


**Figure B.4:** Sequence of time slices for the recorded vertical component of shotpoint S2. On the left hand side time slices start at 30ms with 10ms time increment for illustration of P waves refracting into the water table. On the right hand side timeslices start at 200ms with 20ms time increment illustrating converted and surface waves.

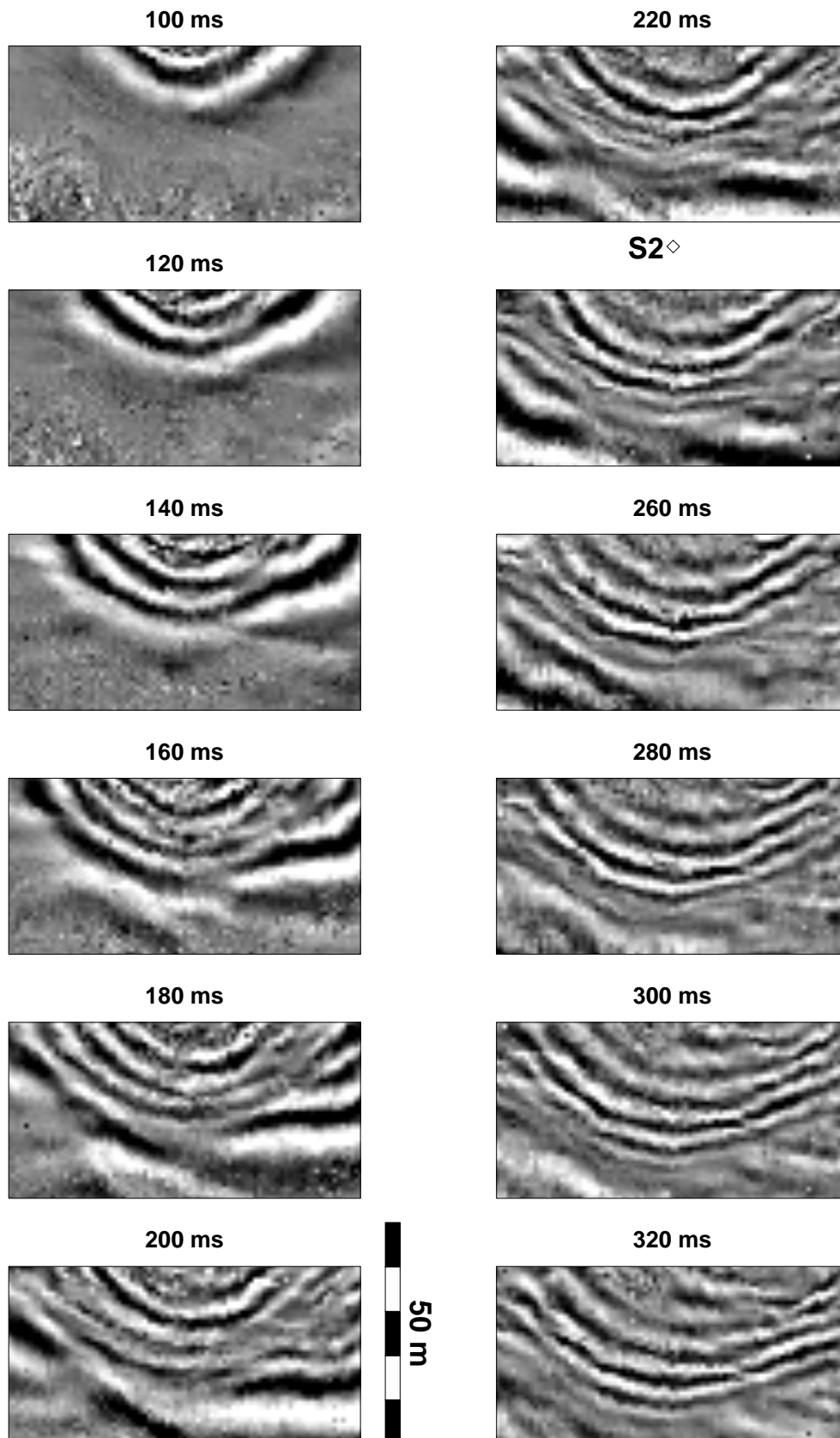


**Figure B.5:** Sequence of time slices with 20ms time increment, starting at 100ms for the radial configuration after slowness projection for shotpoint  $S2$  with shot direction  $Y$ .

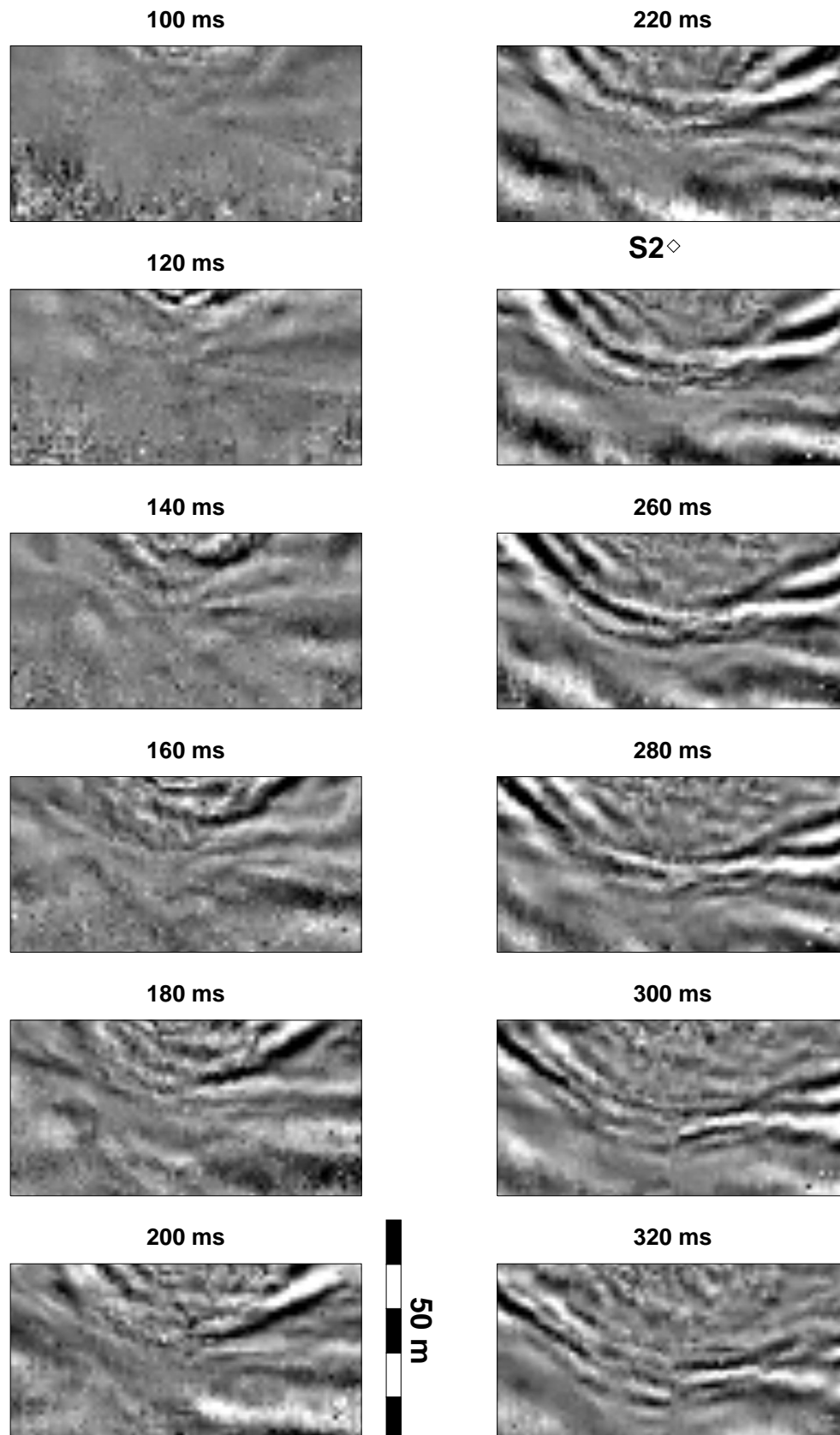


**Figure B.6:** Sequence of time slices with 20ms time increment, starting at 100ms for the transverse configuration after slowness projection for shotpoint S2 with shot direction  $X$ .

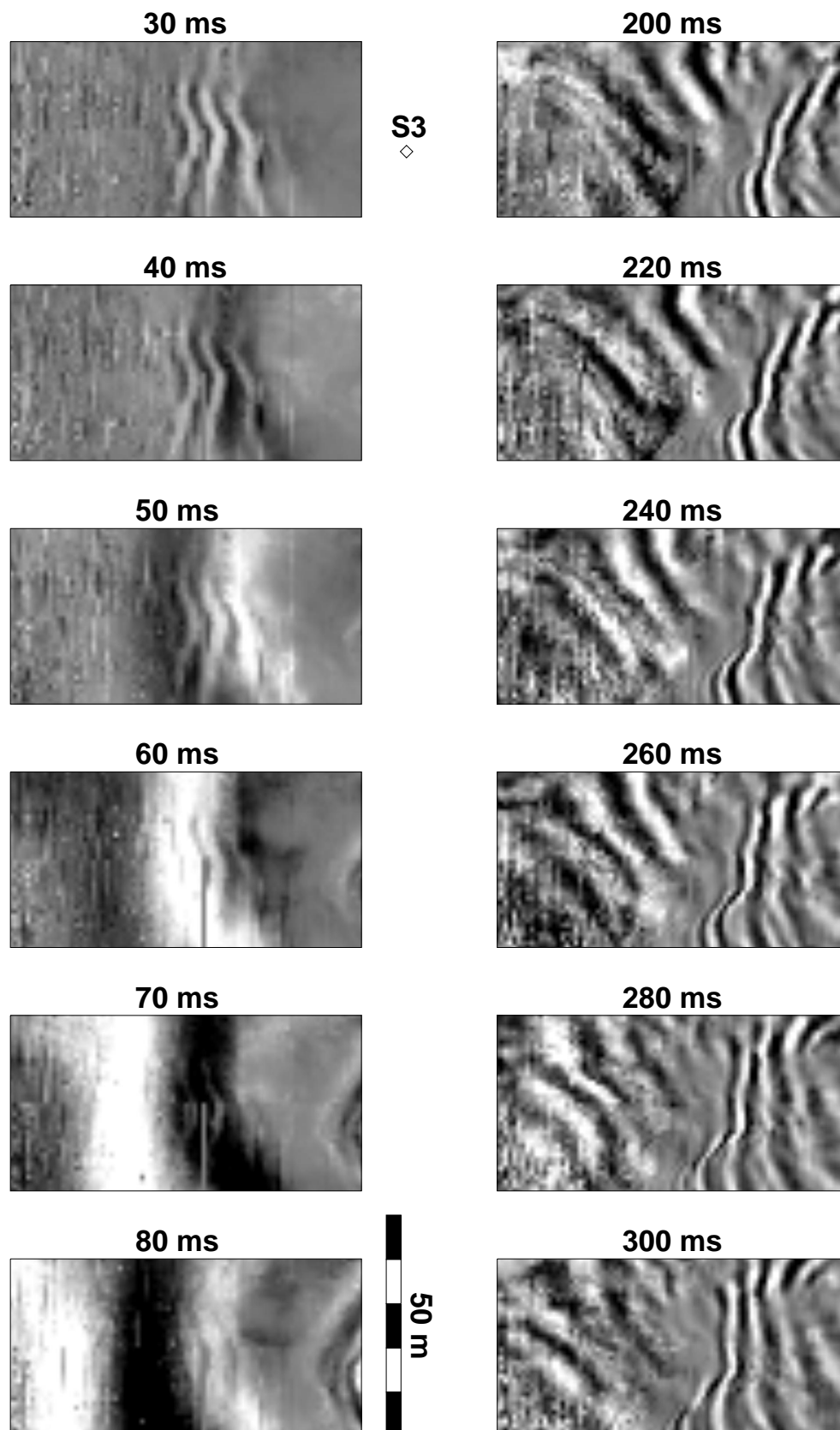


**Figure B.7:** Sequence of time slices for the recorded vertical component of shotpoint S3. On the left hand side time slices start at 30ms with 10ms time increment for illustration of P waves refracting into the water table. On the right hand side timeslices start at 200ms with 20ms time increment illustrating converted and surface waves.

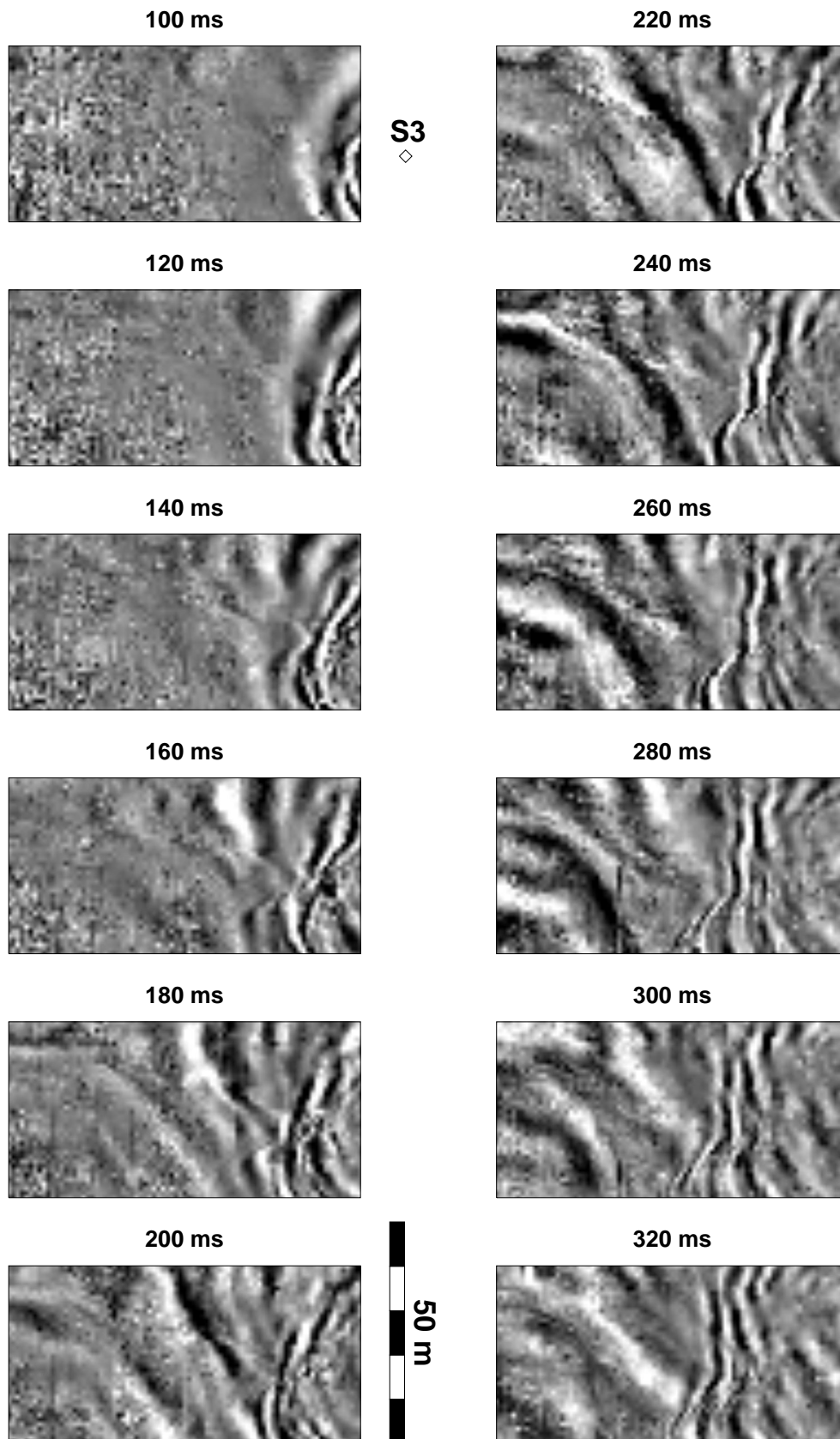


**Figure B.8:** Sequence of time slices with 20ms time increment, starting at 100ms for the radial configuration after slowness projection for shotpoint S3 with shot direction Y.

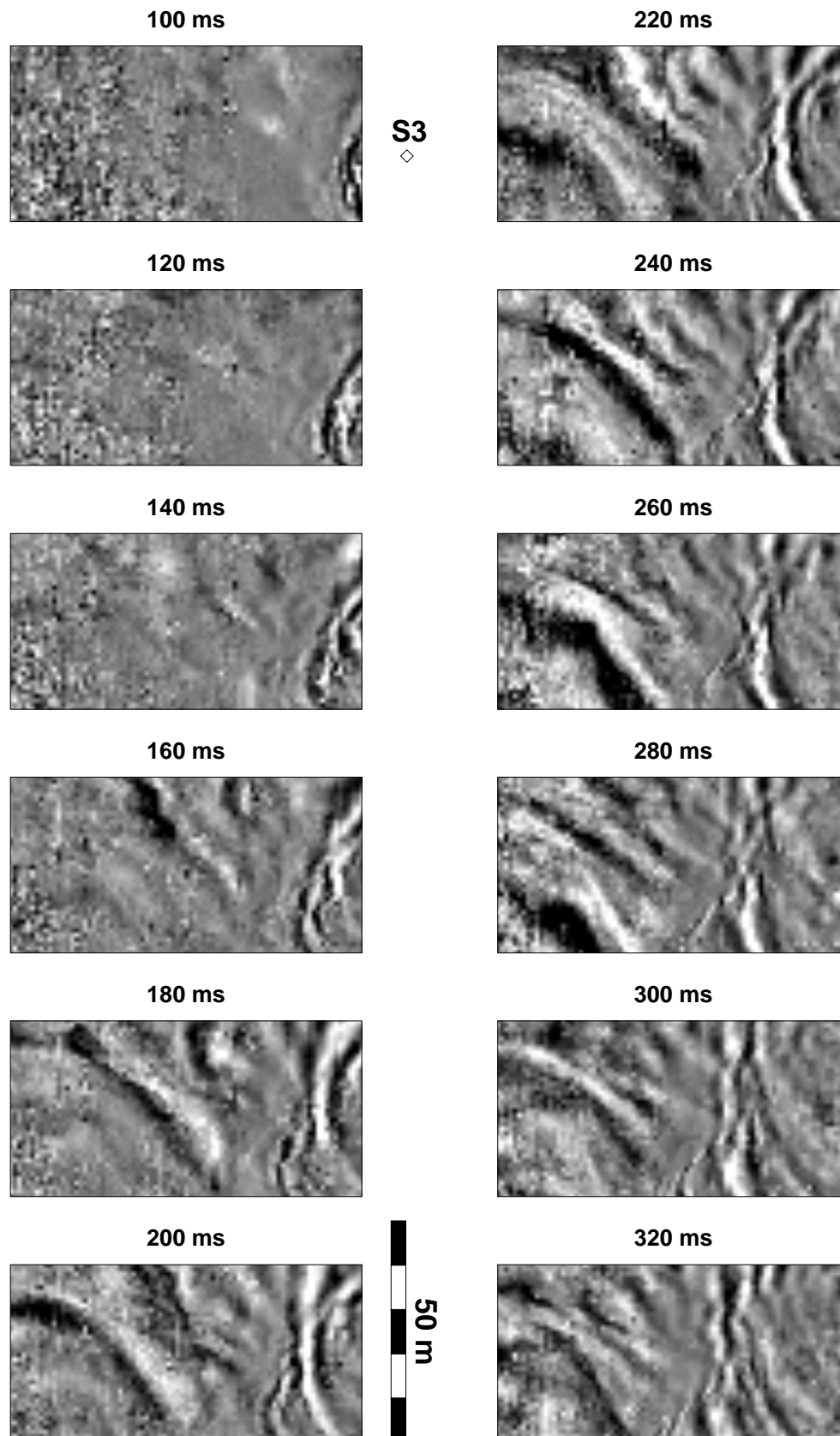


**Figure B.9:** Sequence of time slices with 20ms time increment, starting at 60ms for the transverse configuration after slowness projection for shotpoint S3 with shot direction X.

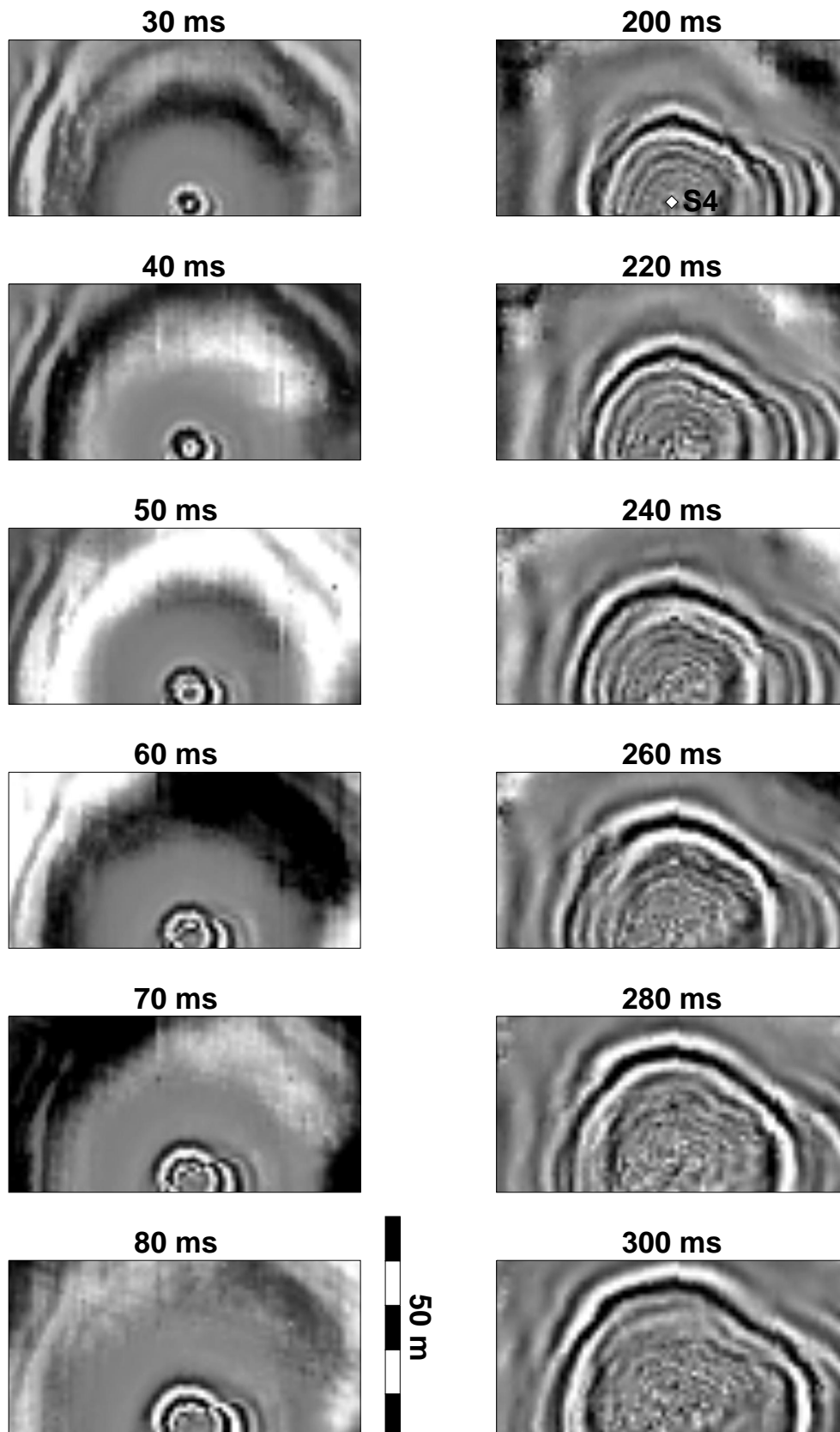


**Figure B.10:** Sequence of time slices for the recorded vertical component of shotpoint S4. On the left hand side time slices start at 30ms with 10ms time increment for illustration of P waves refracting into the water table. On the right hand side timeslices start at 200ms with 20ms time increment illustrating converted and surface waves.



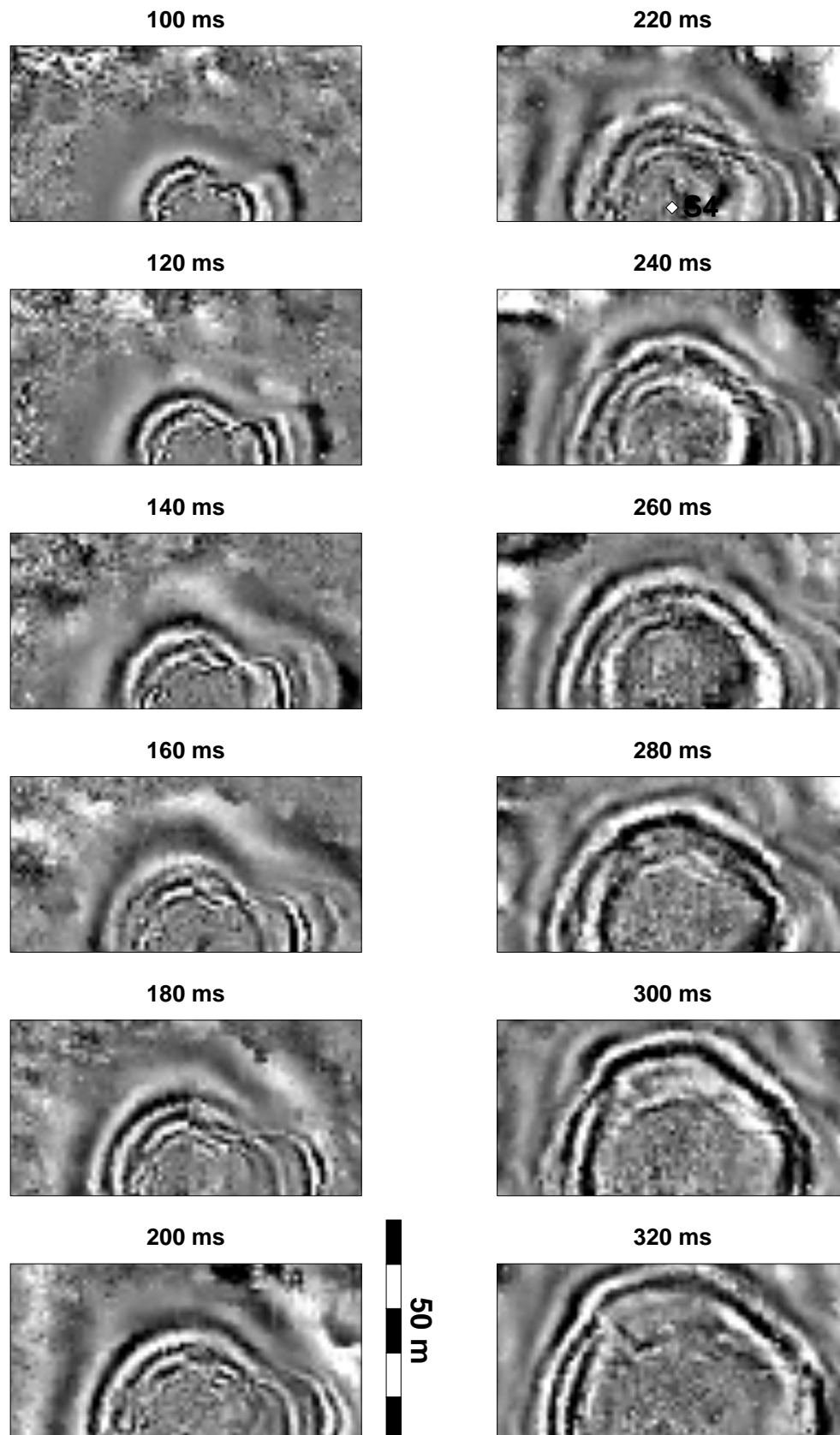


**Figure B.11:** Sequence of time slices with 20ms time increment, starting at 100ms for the radial configuration after slowness projection for shotpoint S4 with shot direction Y.

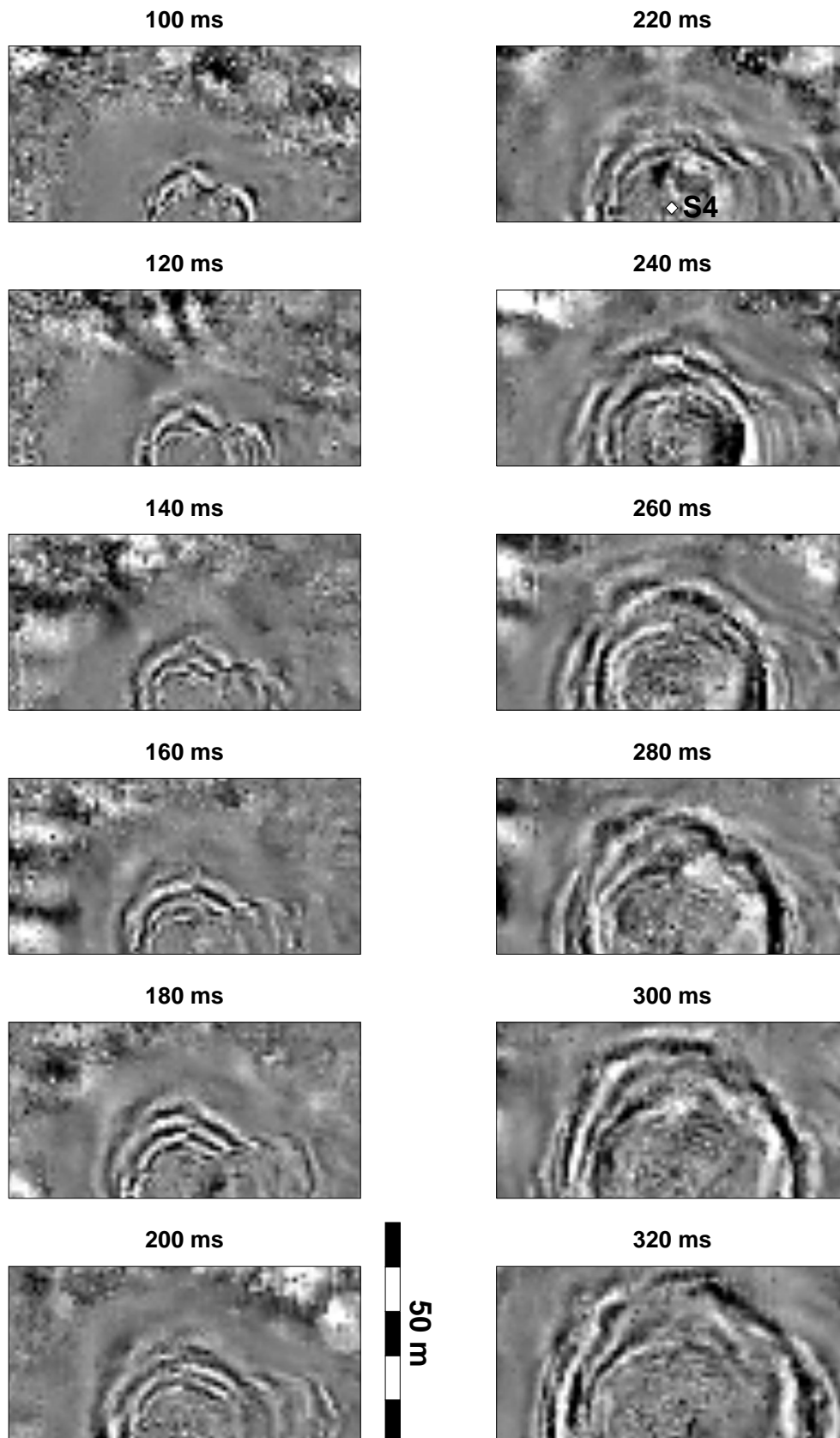


**Figure B.12:** Sequence of time slices with 20ms time increment, starting at 60ms for the transverse configuration after slowness projection for shotpoint S4 with shot direction X.

# Appendix C

## Tomographical Inversion

For tomographic traveltimes inversion a software package provided by John Hole of Virginia Polytechnic Institute and State University was used. It contains the tomography algorithm described in Hole (1995).

The finite difference traveltimes code used in the forward modeling is improved from that described in Hole (1992). John Vidale's original algorithm (Vidale, 1990) has been extended to allow the proper calculation of travel times in the presence of large, sharp velocity contrasts, without significantly sacrificing the superior speed and accuracy of the original algorithm. The new algorithm is described in Hole & Zelt (1995).

In principle the algorithm first calculates first arrival traveltimes and compares them to picked traveltimes obtained from field data. The traveltimes residual attributed and converted to a velocity perturbation is then distributed along corresponding ray paths traced through the initial velocity model. This initial model is then updated by adding these perturbations. In the algorithm smoothing plays the role that regularization or damping does in other algorithms. For a smoothest-model approach early iterations should be smoothed by about half the size of the entire model. Smoothing then is gradually reduced as the iterations converge. This drastically reduces dependence on the starting model by modeling large-scale features first. Two different smoothing concepts are used in the algorithm, one is weighted by number of rays penetrating the corresponding cell, the other one is unweighted (J. Hole, 2003, personal communication).

As starting model a smoothed version of the inverted refractor model derived in section 5.3 was used. The results shown in this thesis were obtained by implementing the smoothing concept shown in table C.1.

Figure C.1 shows intermediate inversion results of the velocity field sliced along the refractor surface: panel (a) after one iteration, panel (b) after 11 iterations, panel (c) after 21 iterations and panel (d) after 31 iterations. Please compare with the velocity field after 39 iterations shown in fig. 5.23, panel (c). Due to the good starting model the iteration converged rather quickly.

Figures C.2 to C.4 show 3-D views of the sliced final velocity model including renderings of the ray coverage data provided by the inversion software for shot points S1, S2, and S3, respectively. Ray coverage is illustrated by isosurfaces with a threshold wrapping

---

<b>Iteration Nr.</b>	<b>Weighted smoothing (nx/ny/nz Points)</b>	<b>Unweighted smoothing (nx/ny/nz Points)</b>
1 – 4	20/20/10	21/21/11
4 – 8	10/10/6	11/11/5
8 – 16	6/6/2	7/7/3
> 16	4/4/2	5/5/1

**Table C.1:** *Smoothing concept for traveltime tomographic inversion.*

model crossed by at least ten rays. Please note, how the rays travel through zones of high velocity, following Fermat's Principle and how they illustrate the difficulties of imaging a refractor with traditional 2-D refraction seismic surveys.

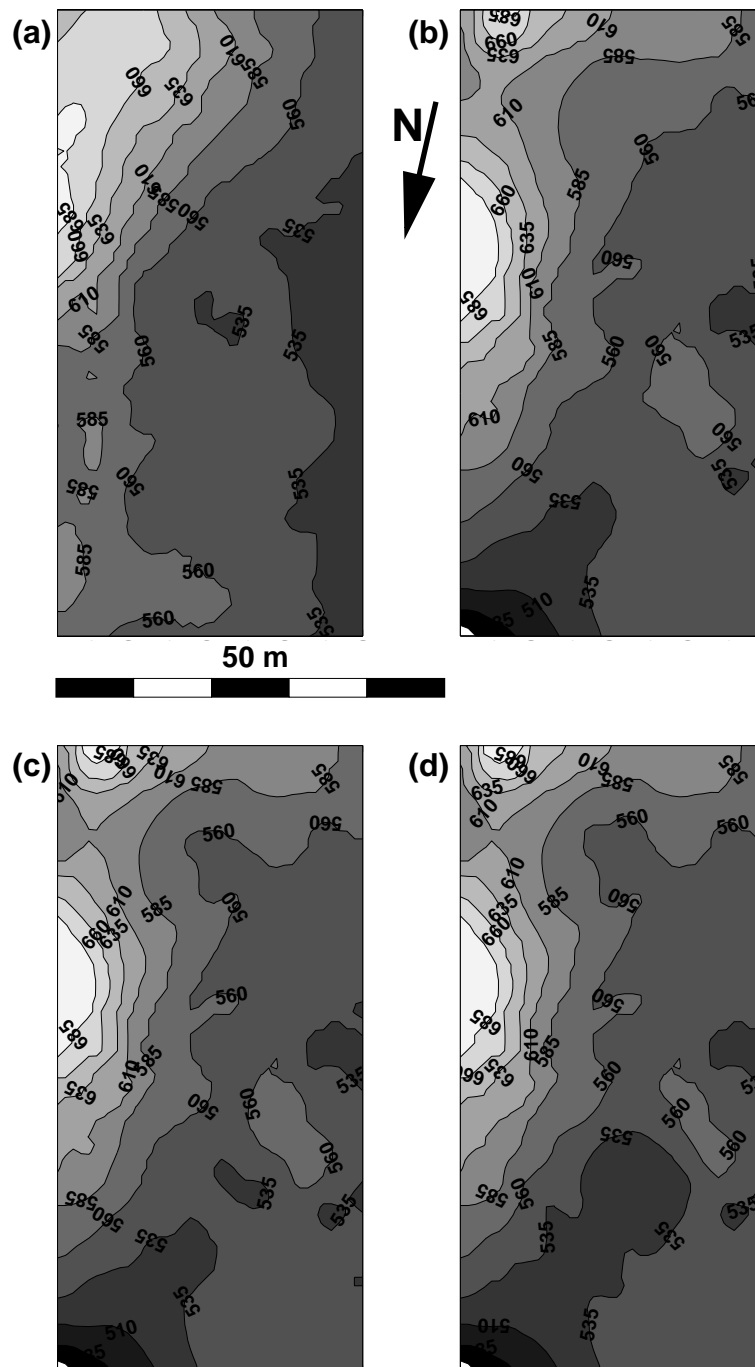


**Figure C.1:** Intermediate results of the velocity field at the refractor surface: (a) after one iteration, (b) after 11 iterations, (c) after 21 iterations and (d) after 31 iterations. Please compare the velocity field after 39 iterations in fig. 5.23, panel (c).

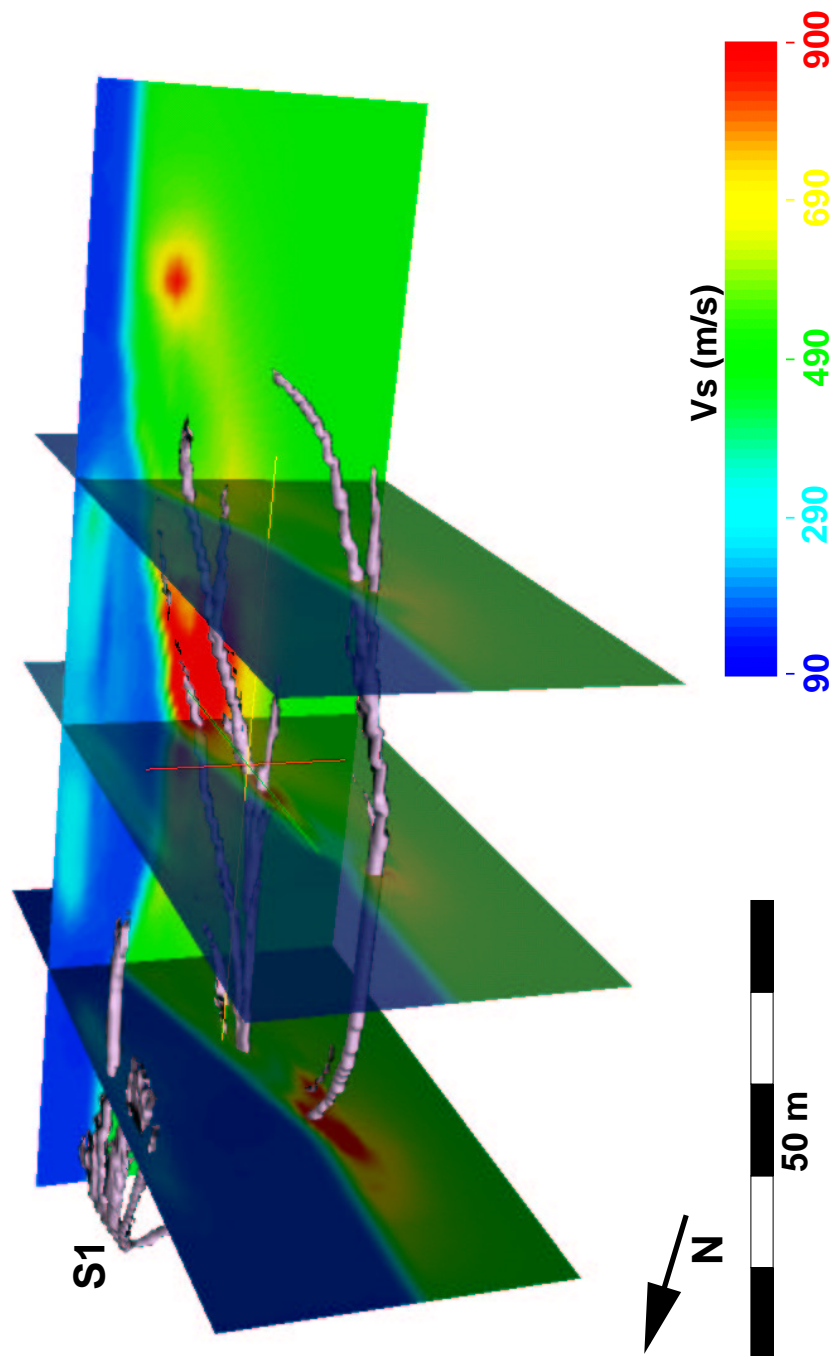


**Figure C.2:** Ray coverage of shotpoint S1. Displayed is the sliced velocity model of the subsurface with isosurfaces that enclose volumes traversed by more than 10 rays.

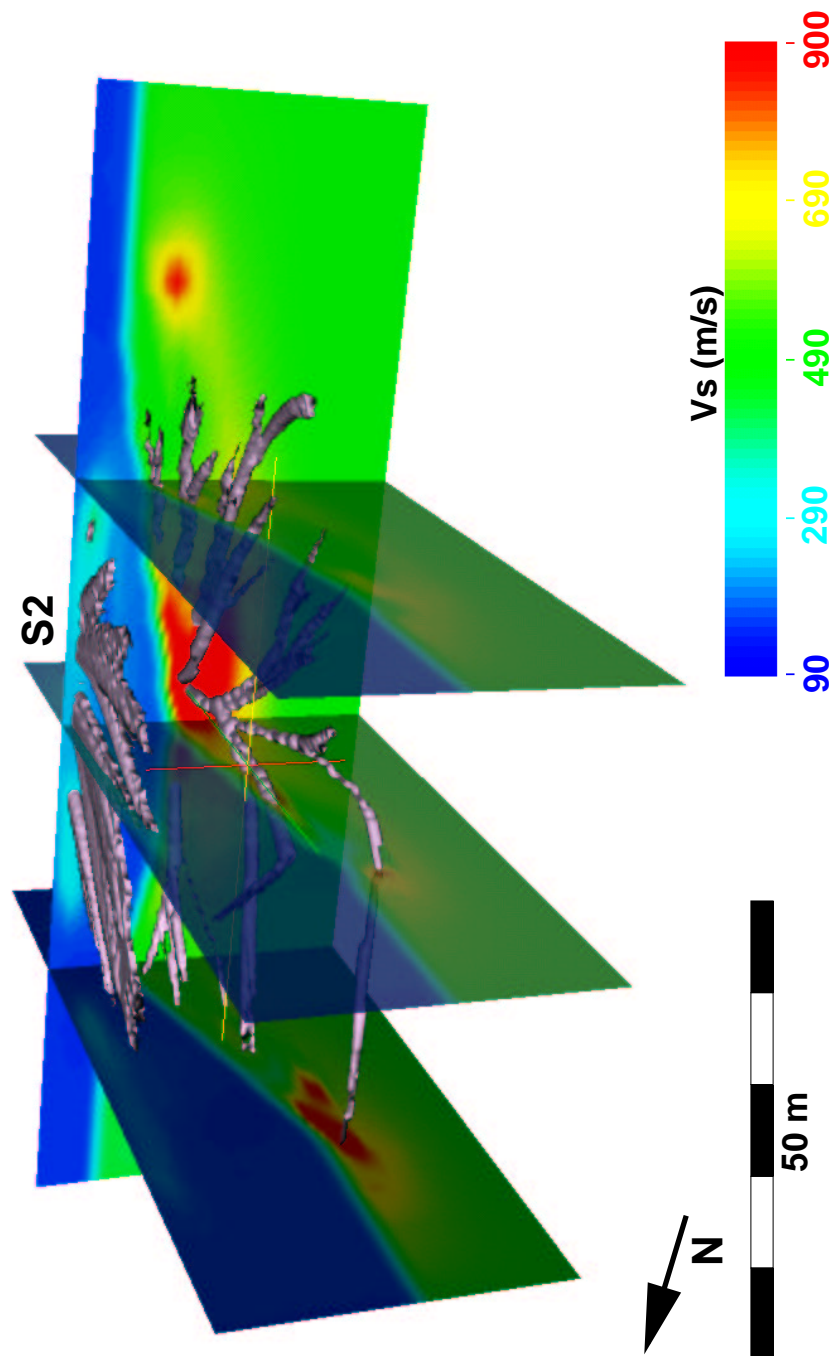


**Figure C.3:** Ray coverage of shotpoint S2. Displayed is the sliced velocity model of the subsurface with isosurfaces that enclose volumes traversed by more than 10 rays.

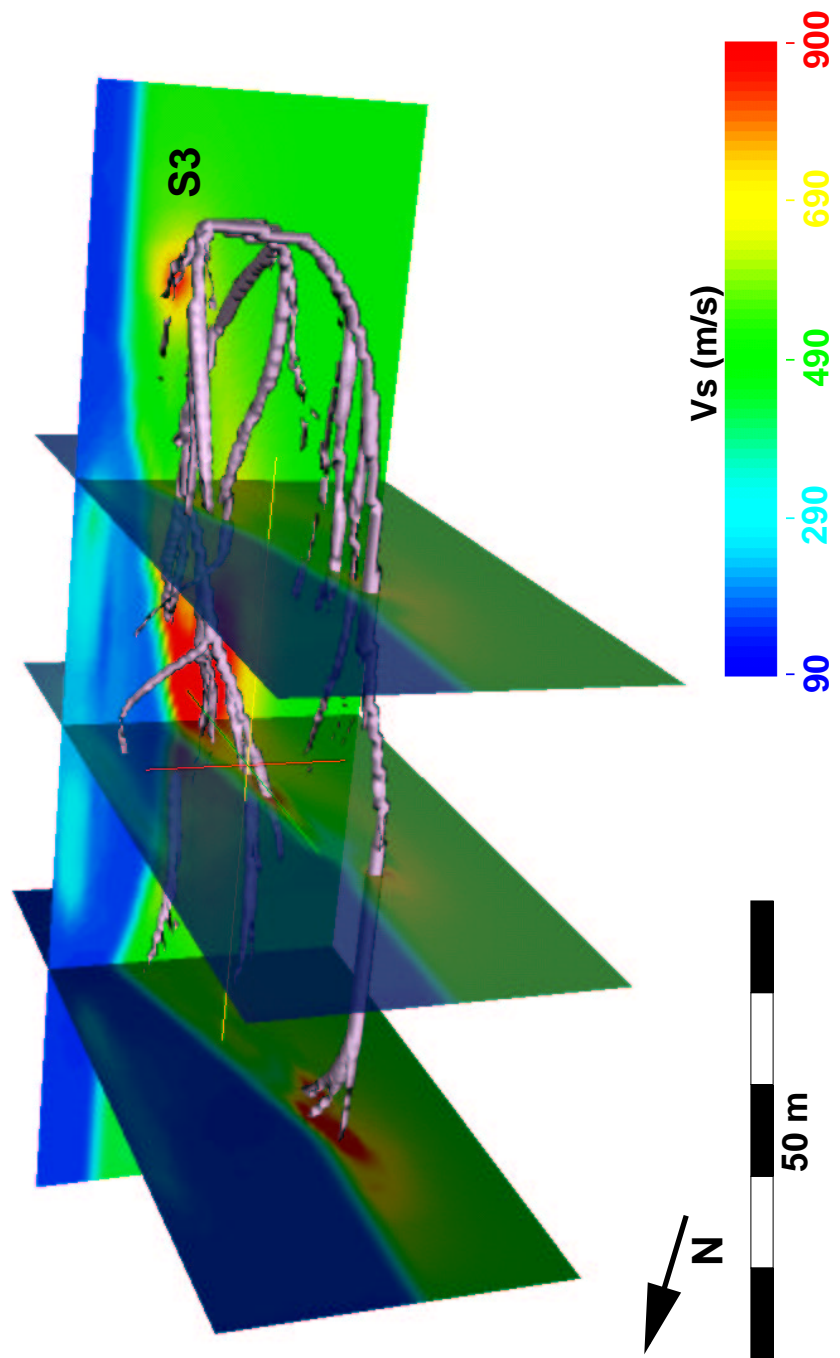


**Figure C.4:** Ray coverage of shotpoint S3. Displayed is the sliced velocity model of the subsurface with isosurfaces that enclose volumes traversed by more than 10 rays.



# Danksagung

An der Entstehung dieser Arbeit waren direkt oder indirekt eine Reihe von Personen beteiligt. Allen gilt mein herzlichster Dank.

Im besonderen danke ich meinem Doktorvater Herrn Prof. Dr. Wolfgang Rabbel für das interessante und innovative Thema, für seine Betreuung, die vielen konstruktiven Vorschläge und für seine Geduld.

Ich danke meinem Korreferenten Prof. Dr. R. Meißner für zahlreiche wichtige Anregungen und die Korrektur der Arbeit.

Dr. Harald Stümpel ermöglichte mir die zahlreichen Meßfahrten nach Sizilien und in die Türkei. Dafür möchte ich mich bedanken. Ebenso bei allen 'Mitfahrerinnen' und 'Mitarbeiterinnen' für die Hilfe und auch den Spaß an den Fahrten.

Dem Land Schleswig-Holstein sei für die Unterstützung durch ein Stipendium, sowie der DFG für die Förderung des Projektes gedankt.

Als Leiter der milesischen Ausgrabungen gab mir Prof. Dr. V. von Graeve von der Ruhruniversität Bochum die Möglichkeit, die Messungen in Milet durchzuführen. Vielen Dank.

Ich danke Prof. Dr. Helmut Brückner, Universität Marburg, für zahlreiche Bohrungen im Löwenhafen (vor allem ganz kurzfristig in diesem Jahr) und für die schnelle und unkomplizierte Bereitstellung der Ergebnisse.

Thanks to John Hole for providing the tomographic inversion program and his advice.

Vielen Dank an alle „3.-Flur'ler“, für die angenehme Arbeitsatmosphäre, die aufmunternden Worte, die zahlreichen Kaffees und Tees, Süßigkeiten und sonstigen Nettigkeiten. Insbesondere meinen alten und neuen Zimmerkolleginnen, Filiz D.-S., Patrick, Birte und Tina danke ich. Herzlichen Dank an Thomas Bohlen für seine immer wieder gern in Anspruch genommene Hilfe bei den Modellierungen.

Danke Thies, für Deine positive Art und guten Ratschläge.

Danke Filiz B., dass Du mir immer wieder geduldig zugehört hast und mein Jammern vor allem in der letzten Zeit ertragen hast. Du hast es auch bald geschafft!

Ich danke der Firma GLS & Co. für die stets sofortige Hilfe bei Problemen kleinerer und größerer Art.

Danke an die weltweit besten MiBeWo's und Freunde: Martina, Christof, Wolfgang & Inken, Merret und Markus & Anne, O'4 & Carine, Susanne & Sven, Claudia, Juliane & Frank und vielen anderen.

Die Polarsternfahrt ANT XVII/2 wurde für mich zu einem unvergeßlichen Erlebnis. Dafür danke ich allen 'Mitfahrern', insbesondere Wilfried, Johannes, Micky und Uli.

During my time at the GSC in Ottawa I met many interesting people and learned a lot. Thank you for this opportunity. Gilles & Nathalie, Erick & Line, Juanjo & Bea, Xavi, Ron & Louise, Danita thanks for the good time in Ottawa. I really miss you all and also the Canadian winter.

Bedanken möchte ich mich auch bei meinen Eltern, die mich während meines gesamten Studiums in jeder Hinsicht vertrauensvoll unterstützt haben und bei meinen Geschwistern, die mich immer ernst genommen haben.

Ich möchte meinem lieben Freund Christof für alles danken. Er ist immernoch das Beste, was mir je widerfahren ist!

## Lebenslauf

Name: Susanne Wölz  
Geburtsdatum: 16. August 1966  
Geburtsort: Kleinmachnow  
Staatsangehörigkeit: deutsch  
Familienstand: geschieden

### Schulbildung

1972-1982 Maxim-Gorki-Schule Kleinmachnow, Realschulabschluß  
1984-1986 Abendschule der VSH, Abitur

### Ausbildung & Berufstätigkeit

1982-1984 Ausbildung zur Film- und Videolaborantin  
1984-1986 Filmlaborantin im DEFA-Studio für Spielfilme  
1986-1989 Fotolaborantin beim Berliner Verlag  
1989-1992 Fotolaborantin beim City-Labor-Service, Berlin

### Studium, Praktika & Berufstätigkeit

1993-1996 Geophysik an der TU Berlin, Vordiplom  
1996-1999 Geophysik an der Christian-Albrechts-Universität zu Kiel  
Abschluß: Dipl. Geophysikerin

seit 1999 Promotionsstudentin  
1999-2001 Stipendiatin des Landes Schleswig-Holstein  
seit 2001 wissenschaftliche Mitarbeiterin am Institut für  
Geowissenschaften, Abteilung Geophysik

1999 Praktikum am Geological Survey of Canada in Ottawa  
2000 Polarstern-Expedition ANT XVII/2 in die Antarktis  
2000-2001 Praktikum am Geological Survey of Canada in Ottawa

Kiel, den 03.November 2003

Susanne Wölz

## **Eidesstattliche Erklärung**

Ich erkläre hiermit an Eides Statt, daß ich die vorliegende Arbeit selbständig und ohne Benutzung anderer, als der angegebenen Hilfsmittel angefertigt habe -abgesehen von der Beratung durch den Betreuer. Die aus fremden Quellen direkt übernommenen Gedanken sind kenntlich gemacht.

Diese Arbeit wurde weder in gleicher Form einer anderen Prüfungsbehörde vorgelegt, noch veröffentlicht oder zur Veröffentlichung eingereicht.

Kiel, den 03. November 2003

Susanne Wölz